SAND77-1517
Unlimited Release
UC-21

# Laser Development for Laser Fusion Applications Research Progress Report January-September 1977



Directorate of Physical Research


SF 2900 Q(7-73)

SAND77-1517
Unlimited Release
Printed February 1978

Distribution
Category
UC-21

# LASER DEVELOPMENT FOR LASER FUSION APPLICATIONS
# RESEARCH PROGRESS REPORT
January - September 1977

Directorate of Physical Research 5200
Sandia Laboratories
Albuquerque, New Mexico 87115

CONTENTS

CONTENTS (cont)

# LASER DEVELOPMENT FOR LASER FUSION APPLICATIONS
## RESEARCH PROGRESS REPORT
## January - September 1977

# LASER DEVELOPMENT FOR LASER FUSION APPLICATIONS

## INTRODUCTION

Advances in knowledge about laser-driven thermonuclear implosions have been and are being paced by the development of advanced laser drivers. The physical principles of this promising new source of energy are now quite clear, and commercialization of laser-fusion energy will be paced by the development of advanced high-average-power laser drivers.

The laser research and development described herein was conducted for the USERDA, Division of Laser Fusion. The goal of this research is to develop the laser technology that is required for commercialization of laser-fusion energy.

Our program addresses three promising high-power laser systems: iodine, hydrogen fluoride and Group VI atoms. Both the iodine laser and the HF laser have a demonstrated high-power capability, and experimental results indicate that there are probably no serious problems in the way toward development of either of these lasers for laser-fusion applications. In both these technology-development programs, we are making steady technical progress: we know where we are going, we understand the problems and know how to go about solving them, and we have a sufficient number of alternatives to give confidence for success. The Group VI atom lasers continue to show great promise as high-power lasers, but the progress toward development of these lasers has been disappointing. In this report we describe in detail the progress that we have made in the development of these three lasers, and we document the areas that need further study.

## HF-LASER PROGRAM

### Overview

Sandia's HF-laser program for FY 77 and FY 78 was revised in June 1977 in order to meet several new program milestones that were established by the Division of Laser Fusion of ERDA. The present HF-laser program objectives are to: (1) improve the kinetics code so that reliable projections of large systems can be made, (2) demonstrate efficient energy extraction from HF high-gain amplifiers, (3) demonstrate focusability of the HF laser, and (4) demonstrate short-pulse generation and amplification. The new milestone schedule will lead to the demonstration of high-optical-quality short-pulses (5 ns) from large-volume amplifiers before the end of FY 78. Optical quality will be demonstrated by performing small-diameter pinhole transmission studies. In order to concentrate our effort on meeting our immediate objectives, portions of our previous program have been postponed or terminated. The canceled or terminated programs are: theoretical and experimental kinetic studies, a prototype angular multiplexing experiment, high-pressure flowing $H_2$-$F_2$ stability studies, and the development of a backup near-diffraction-limited oscillator-preamplifier chain.

There were two major experimental accomplishments in this reporting period. The first was the demonstration of efficient energy extraction from a 200-J amplifier using an oscillator whose spectra matched that of the amplifier. The second was the development of a near-diffraction-limited multiline oscillator-preamplifier system to be used for the upcoming demonstrations of high-optical-quality beams from large-volume high-energy HF amplifiers. In addition, the HF kinetics code has been upgraded with more recent kinetic data, and comparisons of predictions by our code with others are now satisfactory.

### Objective of HF Oscillator-Amplifier Studies Using $H_2$-$F_2$ Gas Mixtures

One of the purposes of these studies was to determine the energy extraction characteristics of a large-volume high-energy

electron-beam-initiated amplifier using an oscillator whose spectra matched those of the amplifier. Of particular importance is the input energy density required to extract a significant amount of energy from the amplifier. The input energy density required to suppress both backward and forward amplified spontaneous emission (ASE) and parasitic oscillations must be known in order to project performance of advanced systems and to estimate the expected level of prepulse on target.

The second purpose of this series of studies was to compare the beam divergence of the amplified beam with that of the beam incident on the amplifier in order to document that severe degradation of beam optical quality is not experienced. Because of the power and energy requirements of the oscillator, a large-volume (2.9 liter) oscillator was used. Consequently, its output was many times diffraction limited, and focusability studies would not be indicative of limitations imposed by the amplifier medium. The next generation experiments will use a near-diffraction-limited oscillator-preamplifier chain to demonstrate good focusability of amplified beams from large-volume HF amplifiers.

## Characteristics of Large-Volume Oscillator Using $H_2$-$F_2$ Mixtures

The operating characteristics of the L-geometry electron-beam-excited oscillator that was used for the oscillator-amplifier studies were carefully documented. The details of this system and some of the experimental results were discussed in the last semiannual report. The optical cavity of the oscillator was a stable configuration and consisted of a calcium fluoride flat and a 20-metre-radius-of-curvature copper mirror. The cavity mirror separation was 208 cm and the active medium length was 92 cm, giving an active volume of 2.9 ℓ. The laser was normally operated with $Al_2O_3$ brewster-angle windows.

The total output energy from the laser was measured as a function of $F_2$ pressure at a constant $F_2/O_2/H_2$ ration of 1.0/0.3/0.25. The results are shown in Fig. 1. Also shown in Fig. 1 is the dependence of the laser pulse width (FWHM) as a function of $F_2$ pressure and the previously reported e-beam energy deposition results. Above a pressure of about 400 torr $F_2$, the laser energy output begins to deviate from the linear energy deposition. This behavior is believed to be due to parasitics. The evidence for this assumption will be discussed later.

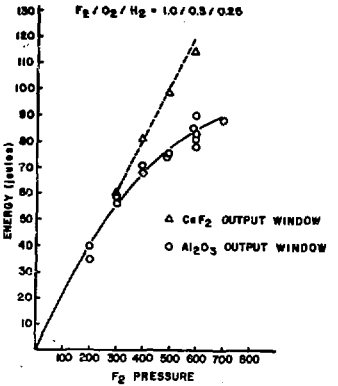


Fig. 1. Oscillator energy output as a function of $F_2$ pressure for a fixed $F_2$:$O_2$:$H_2$ ratio of 1:0.3:0.25. Also shown is the pulsewidth (FWHM) and the estimated electron-beam energy deposition.

The time-integrated spectra of the laser output were obtained using a Sandia-built grating spectrograph. The spectral data were recorded as a burn pattern on unexposed developed Polaroid film. An estimate of intensity was made by visual inspection of these burn patterns. These data are listed in Table I.

TABLE I

Identification and Relative Intensity of the Oscillator Spectra

| Identification | Intensity | Identification | Intensity | Identification | Intensity |
|---|---|---|---|---|---|
| $P_1(6)$ | M | $P_2(9)$ | VS | $P_5(7)$ | S |
| $P_1(7)$ | S | $P_2(10)$ | VS | $P_2(8)$ | M |
| $P_1(8)$ | S | $P_2(14)$ | W | $P_5(9)$ | M |
| $P_1(9)$ | VS | | | $P_5(10)$ | VW |
| $P_1(14)$ | M | $P_3(4)$ | M | | |
| $P_1(15)$ | W | $P_3(5)$ | VS | $P_6(4)$ | M |
| $P_1(16)$ | W | $P_3(6)$ | VS | $P_6(5)$ | M |
| $P_1(17)$ | W | $P_3(7)$ | VS | $P_6(6)$ | M |
| $P_1(18)$ | VW | $P_3(8)$ | VS | $P_6(7)$ | VW |
| $P_1(19)$ | VW | $P_3(9)$ | S | $P_6(8)$ | VS |
| $P_1(20)$ | VW | | | $P_6(9)$ | VW |
| $P_1(21)$ | VW | $P_4(5)$ | M | | |
| | | $P_4(6)$ | M | | |
| $P_2(4)$ | VW | $P_4(7)$ | S | | |
| $P_2(5)$ | S | $P_4(8)$ | S | | |
| $P_2(6)$ | VS | $P_4(9)$ | M | | |
| $P_2(7)$ | VS | | | | |
| $P_2(8)$ | VS | $P_5(4)$ | W | | |
| | | $P_5(5)$ | M | | |
| | | $P_5(6)$ | S | | |

The relative energy spectral distribution was obtained by placing a small-aperture calorimeter behind the film plane in the spectrograph. The spectral range was defined by the aperture site. This spectral distribution of the energy output of the laser is shown in Fig. 2. The grating used to obtain these data was blazed at 2.8 microns. No correction for the variation of grating efficiency with wavelength has been made. As a rule of thumb, the efficiency curve for a grating blazed at $\lambda_B$ drops to about 70 percent of blaze efficiency for $\lambda = \lambda_B \pm \lambda_B/2k$ (in order k). Because of this rule of thumb, the wavelength dependent correction for grating efficiency would not be expected to be large from 2.6 to 3.5 μm. Also shown in Fig. 2 are the wavelength locations of the various vibration-rotation lines which have been identified in the time-integrated spectrum. About 70 percent of the total output energy is in the wavelength region between 2.6 and 3.0 microns. The spectral lines in this region originate primarily from the first, second, and third vibrational levels.

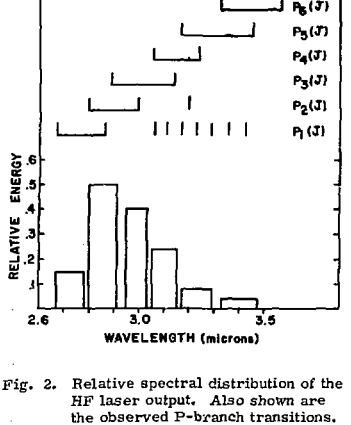


Fig. 2. Relative spectral distribution of the HF laser output. Also shown are the observed P-branch transitions.

The temporal behavior of selected vibration-rotation lines have also been obtained. These data, which have been time correlated with the electron-beam current and the spectrally unresolved laser pulse, are shown in Fig. 3. The time marked $T_1$ is the start of the electron-beam current and the time $T_2$ indicates the start of the laser pulse. As these data show, lasing occurs initially on the 2 → 1 vibrational transition. The sequences $P_3(5)$, $P_2(6)$, and $P_1(7)$ are in cascade, and the data indicate that lasing on the $P_3(5)$ and $P_1(7)$ lines starts after lasing starts on $P_2(6)$. These data suggest that, in this cascade system, the population of vibration-rotation level v = 2, J = 5 is initially inverted with respect to the population of the v = 1, J = 6 level, while there is no initial population inversion of the v = 3, J = 4 level with respect to the v = 2, J = 5 level, and there is also no initial inversion of the v = 1, J = 6 level with respect to the v = 0, J = 7 level. As lasing starts on the $P_2(6)$ transition, the population of the v = 2, J = 5 level starts to decrease and the v = 3, J = 4 level becomes inverted with respect to the v = 2, J = 5 level. Lasing then occurs on the $P_3(5)$ transition. Also, lasing on $P_2(6)$ increases the population of the v = 1, J = 6 level with the result that it is inverted with respect to the v = 0, J = 7 level. Lasing then occurs on the $P_1(7)$ transition. As further evidence that this cascade behavior is correct, the periodic oscillations that occur on each of the lasing transitions has the proper temporal correlation. That is, when $P_2(6)$ is at a maximum, $P_3(5)$ and $P_1(7)$ are at a minimum, and when $P_2(6)$ is at a minimum, $P_3(5)$ and $P_1(7)$ are at a maximum. The frequency of the periodic oscillations corresponds to the round trip transit time of our low Q cavity.

The thin-film ablation technique for obtaining focal-spot intensity distribution, which was described in the last progress report, has been used to measure the focal-spot intensity distribution obtained with a 1-metre-focal-length mirror. These results are shown in Fig. 4. Integration of the focal-spot intensity distribution indicates that 90 percent of the output energy is contained within a cone of angular half-width equal to 3.5 milliradians. This number assumes that the

focal-spot intensity distribution does not have a large-diameter low-intensity tail.

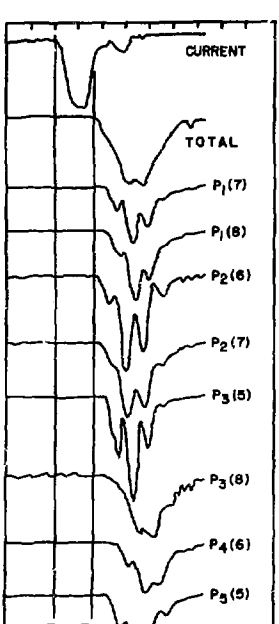


Fig. 3. Time correlation between the electron-beam current, total laser output and various P-branch transitions. The time $T_1$ represents the beginning of the current pulse, while $T_2$ represent the onset of the laser pulse.

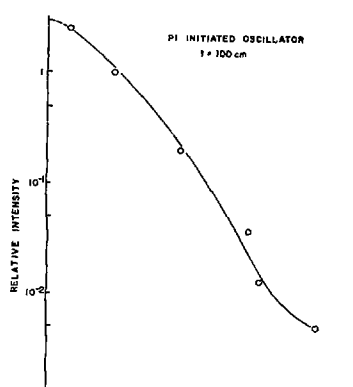


Fig. 4. Focal-spot intensity distribution for the electron-beam initiated oscillator.

The effect of parasitic oscillations on the laser output is now discussed. In the section on HF code development, a simple one-line computer code is discussed which allows lasing to occur transverse to the optical axis of the laser cavity. It is found that, under certain conditions, oscillator performance can be degraded even when the threshold gain for parasitics exceeds the cavity threshold gain. This effect occurs because of gain overshoot. This simple model predicts that parasitics will become important for specific conditions, namely, when the ratio $\ell_T/L_T$ is greater than $\ell_L/L_L$, where $\ell_T$ and $\ell_L$ are the transverse and longitudinal dimensions of the laser medium, respectively, and $L_T$ and $L_L$ are the mirror separation of the transverse and longitudinal cavities. These conditions are probably fulfilled in this oscillator because the ratio $\ell_L/L_L$ is about equal to 0.5, while $\ell_T/L_T \approx 1$. As an

experimental check of this model, the output energy of the oscillator could be determined as a function of the length of the longitudinal optical cavity. However, in the present configuration of the oscillator, it is not possible to make an appreciable change in this length. It is possible to reduce the longitudinal cavity loss by replacing the sapphire windows with calcium fluoride windows. This has the effect of lowering the longitudinal cavity threshold with respect to the transverse cavity threshold. The results with $CaF_2$ windows are compared with $Al_2O_3$ windows in Fig. 5. With the lower loss longitudinal cavity, the oscillator energy output does not deviate from a linear pressure dependence as it does when the $Al_2O_3$ windows are used. While this single experiment does not prove the importance of parasitic oscillations in this oscillator, it does give reason to believe that they may be important in systems for which the active medium is much shorter than the cavity length.

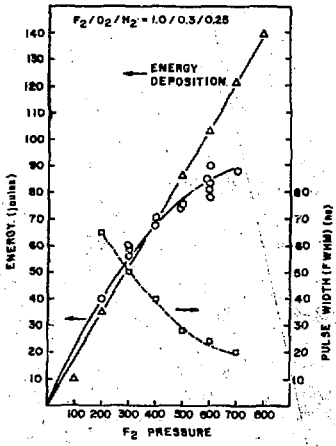


Fig. 5. Laser output energy as a function of $F_2$ pressure for two different types of output windows.

The oscillator output energy should also be influenced by changing the laser tube wall reflectance. This will have the effect of lowering the threshold for transverse lasing. To increase the wall reflectance, a thin stainless-steel liner was inserted into the laser tube. For a mixture of $F_2/O_2/H_2$ equal to 400/120/100 torr, no output energy from the oscillator was detected. With these same conditions, without a liner, an output energy of about 70 joules was measured. The gain overshoot in the HF laser is related to the $H_2$-$F_2$ burn time (i.e., the magnitude of gain overshoot increases with decreasing burn time), and it is possible to change the burn rate by changing the concentration of molecular hydrogen in the laser gas mixture. The laser energy output as a function of $H_2$ pressure was measured for the case of the normal laser tube and the case of a stainless-steel liner. The results are shown in Fig. 6. Also shown is the laser pulse duration (FWHM) for both cases as a function of $H_2$ pressure. For the case of the stainless liner, one observes an increase in output energy as the $H_2$ pressure is increased and then an extremely rapid decrease in output energy.

These experiments indicate that either a poor optical cavity design or a high reflectivity laser tube wall may severely degrade the performance of a large-volume HF laser oscillator.

## Characteristics of Large-Volume Amplifier Using $H_2$-$F_2$ Mixtures

The amplifier used in the extraction experiment was electron-beam initiated and used mixtures of $H_2$, $F_2$, and $O_2$. The electron-beam used for this amplifier was our Maxwell Labs POCO machine (MIMI). Some electron-beam deposition studies for the amplifier were given in the last semiannual report.

Scattering structures were inserted in the standard MIMI diode to increase the electron-beam temperature in an effort to reduce the strong pinching reported in the last semiannual report. Only slightly improved electron-energy spatial distributions were obtained by this method. Therefore,

the drift region and pressure relief tank between the electron-beam machine and the laser cell were removed and the diode was modified to extend the anode 15 cm from the normal location. Figure 7 is a schematic view of the modified arrangement. The standard 50-cm-long cathode was used on a 0.64-cm x 50-cm x 15-cm-long cathode extension shank. A 25 $\mu$m-thick titanium anode was separated from a 127-$\mu$m-thick stainless-steel high-pressure window by a 1-cm-thick support structure. Rectangular openings 1.27 x 5 cm in the support structure allowed passage of the electron beam. No failures in the high-pressure window due to reaction overpressure have occurred in over 300 shots. This modified geometry has been operated at a diode voltage of 1.5 MeV and diode current of approximately 85 kA.

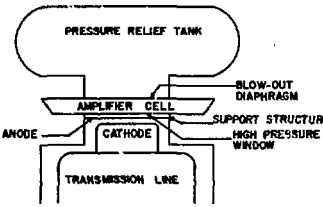


Fig. 7. Schematic view of modified diode arrangement used for the electron-beam initiated amplifier.

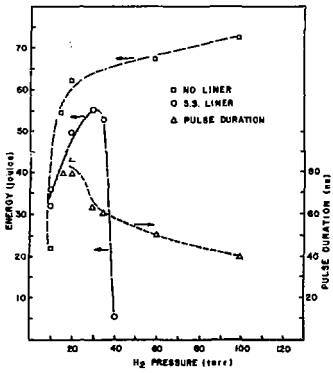


Fig. 6. Laser output energy as a function of $H_2$ pressure with and without a thin stainless steel liner. Laser pulse duration (FWHM) are also shown for both configurations.

The electron-beam energy distribution measured along the optical axis of the amplifier cell is shown in Fig. 8. For these measurements the cell was filled with 1352 torr of $N_2$ which has a density equal to an $F_2/O_2/H_2$ mixture of 800 torr/240 torr/200 torr. The measurements were made using a single linear array of 23 calorimeter elements. Each element was 2.54 cm x 2.54 cm. The FWHM of this distribution is 44 cm compared with an FWHM of 30 cm with the normal diode. Of equal significance is the more uniform distribution with the modified geometry. CYLTRAN calculations[1] indicate that 0.1 joule of electron-beam energy is deposited in the laser volume for each torr of the $F_2$-$O_2$-$H_2$ mixture.

Figure 9 is a schematic cross section of the amplifier cell. In addition to the main amplifier axis, additional ports were provided to observe radiation perpendicular to and at a 15-degree angle to the amplifier axis. All surfaces around these axes were machined with a phono-finish to reduce specular reflections. The cell was constructed to minimize the volumes near the high-pressure window and near the blow-out diaphragm, since these volumes were not contained within the cylindrical optical cavity (unprobed volume).

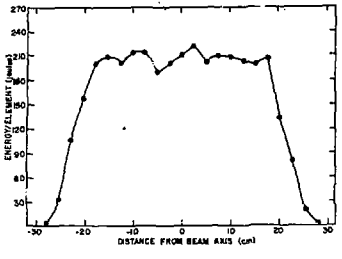


Fig. 8. Electron-beam energy distribution along the optical axis of the laser cell.

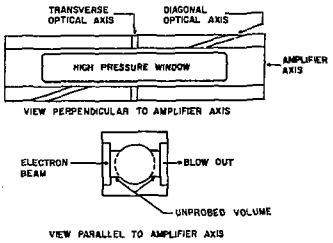


Fig. 9. Schematic cross sections of the amplifier cell.

The amplifier was operated an as oscillator to investigate the laser energy output as a function of pressure to determine laser output timing with respect to electron-beam current, and to devise means for reducing parasitic oscillations. The mole ratio of $F_2/O_2/H_2$ was held constant at 1/0.3/0.25. Initial energy measurements were obtained with sapphire brewster-angle windows and with resonator reflectors separated by 3 metres. These reflectors consisted of a 12-metre-radius-of-curvature gold mirror and an Infrasil-quartz flat. With a brass blow-out diaphragm and with a mixture containing 400 torr of $F_2$, only 8 joules was extracted from the volume as shown in Fig. 10. This energy was increased to ~ 25 joules by replacing the brass diaphragm with a mylar diaphragm, which allows most of the transverse radiation to escape into the pressure relief tank. Curve (a) in Fig. 10 shows the laser energy as a function of $F_2$ pressure for $F_2$ pressures between 400 and 800 torr. The improvement with the mylar diaphragm is attributed to a decrease in parasitic oscillations set up between the high-pressure window and the blow-out diaphragm. When the brewster-angle windows were removed and the reflectors were placed directly on the ends of the amplifier cell, the laser energy increased to the values shown in curve (b) of Fig. 10. The factor of four increase in energy is attributed to the further suppression of parasitic oscillations by the larger laser flux in the excited volume that is realized with the shorter cavity and with elimination of losses by the brewster windows. The factor of four increase with the shorter cavity is consistent with estimates made by the one-point single-transition rate equation treatment. A slight further increase in energy was obtained by lining the cylindrical volume of the amplifier with stainless-steel screen; this prevents low-angle radiation originating in the unprobed volumes from extracting energy from the probed volume. This effect is shown by curve (c) of Fig. 10. The blow-out diaphragm for these measurements was an ebanol-c brass foil which gives the same performance as the mylar sheet but which does not have the disadvantage of leaving molten mylar in the amplifier cell. In addition to the data shown in Fig. 10 the effect of adding 200 torr of $SF_6$ to the $F_2$-$O_2$-$H_2$ mix was investigated. The laser energy increased about linearly from 244 joules at 400 torr $F_2$ to 288 joules at 800 torr. The axes normal to the amplifier and at 15 degrees to the amplifier were monitored with AuGe detectors. No radiation

was detected along either the transverse or the diagonal axis under any conditions.

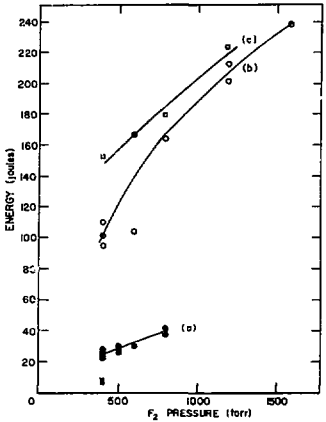


Fig. 10. Energy extracted from the amplifier operated as an oscillator as a function of $F_2$ pressure. The mole ratio of $F_2$:$O_2$:$H_2$ was 1.0: 0.3:0.25. Data points refer to: x - brass blow-out diaphragm, with 3 metre cavity, curve (a) - mylar blow-out diaphragm with 3 metre cavity, curve (b) - mylar blow-out diaphragm with 1 metre cavity, curve (c) - ebanol-c blow-out diaphragm and stainless steel screen liner with 1 metre cavity.

Figure 11 shows the relative timing between the electron-beam current pulse and the laser output signal for a mixture containing 800 torr of $F_2$. The laser pulse width (FWHM) over the $F_2$ pressure range from 400 torr to 1600 torr averaged 49 nanoseconds. No consistent trend to shorter pulse widths at higher pressures was observed.

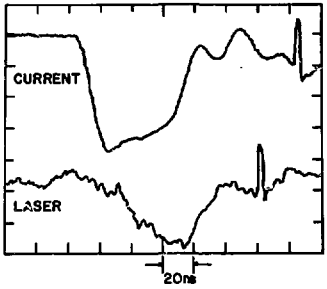


Fig. 11. Relative timing between electron-beam current and laser output intensity.

Spectra from the amplifier, when operated as an oscillator, consisted of the following lines: $P_1(7\text{-}10)$, $P_2(5\text{-}11)$, $P_3(5\text{-}7, 9)$, $P_4(6, 8)$, $P_5(5\text{-}7)$, and $P_6(5)$. These time-integrated spectra were obtained from burn patterns taken at the focal plane of a 1-metre radius of curvature mirror. This technique did not allow us to observe some weak lines that were not capable of producing burns.

## Experimental Results of the Oscillator-Amplifier Study

The objective this experiment was to determine the extractable energy from an HF amplifier as a function of input power, to determine the effect of varying the input power on the amplitude of the forward and backward amplified spontaneous emission

(ASE), and to compare the spatial intensity distribution of the input and output optical beams.

A schematic diagram of the experiment is shown in Fig. 12. The oscillator and amplifier shown in this diagram are the electron-beam-initiated systems whose characteristics were described in the previous two sections. The energy output and pulse shape of the oscillator were monitored using a total absorbing calorimeter and an Au-Ge detector, respectively. The forward and backward ASE were monitored using quartz beam splitters and calorimeters as illustrated in Fig. 12. The temporal behavior of the $ASE_+$ and $ASE_-$ signals were monitored with Au-Ge detectors. To separate the extracted energy in the collimated beam from the radiation emitted at large angles by ASE, the calorimeter that was used to measure the collimated energy was apertured and located 5.4 m from the center of the amplifier. This aperture, which was a 10-cm-diameter copper flat mirror, was located 2.8 m from the center of the amplifier. The collimated beam size at the aperture (10 cm flat mirror) was determined from footprints, and it was determined that all of the energy was collected. The amount of ASE reaching the calorimeter, determined by exciting only the amplifier, was found to be insignificant.

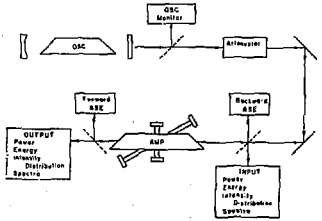


Fig. 12. Block diagram of oscillator-amplifier experiment.

The input power to the amplifier was varied using attenuators. These attenuators consisted of single surface reflections from various combinations of small angle wedges. The peak input intensity to the amplifier was varied from $10^4$ W/cm$^2$ to $10^7$ W/cm$^2$.

The pulse width from the oscillator and the duration of positive gain in the amplifier were both approximately 50 nanoseconds. The energy extraction from the amplifier as a function of delay time between the start of the electron beam current and the start of the oscillator pulse is shown in Fig. 13. Maximum energy is extracted for a time delay of 30 to 40 nanoseconds.

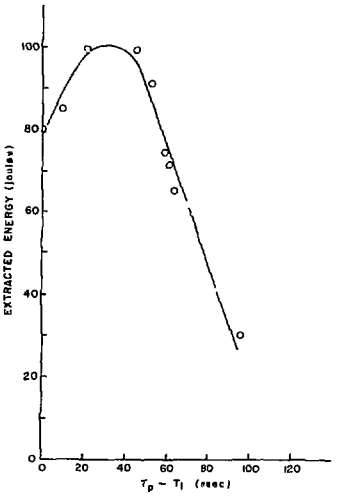


Fig. 13. Extracted energy of the amplifier as a function of delay time between the oscillator pulse and the gain pulse of the amplifier.

The time correlation of the electron-beam current, the oscillator-input into the amplified signal, and the amplified spontaneous emission in the backward direction are shown in Fig. 14. These data have all been time correlated to the same spatial point, namely, the center of the amplifier cell. The amplified signal starts at the same time that the input does, although it reaches a peak approximately 20 ns after the peak of the input signal. The amplified spontaneous emission starts at about the start of the electron-beam current and reaches its peak at about the same time as the amplified signal.

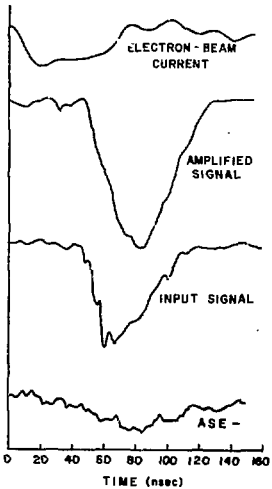


Fig. 14. Time correlated data showing the relationship between the electron-beam current, input intensity, amplified intensity and the amplified spontaneous emission in the backward direction (ASE).

The results of the energy extraction experiment are shown in Fig. 15. All the data were taken with the amplifier operating at an $F_2/O_2/H_2$ pressure of 800/240/200 torr. The $F_2/O_2/H_2$ pressure ratio of the oscillator was 400/120/100 torr. All the data displayed in Fig. 15 were obtained with the delay between oscillator pulse and electron-beam current that gave maximum energy extraction. The input intensity was taken to be the peak intensity of the oscillator pulse measured at the input to the amplifier. The extracted energy was obtained by subtracting from the collimated energy the corrected input energy. A correction for the losses in the two windows on the amplifier was made. The horizontal dashed line in the figure is the energy out of the amplifier that was obtained when it was configured as an oscillator and represents the total extractable energy from the amplifier. The data in Fig 15 show that an input intensity of $10^7$ W/cm$^2$ is sufficient to extract 90 percent of the extractable energy.

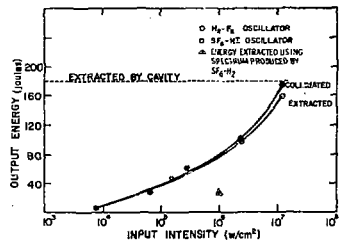


Fig. 15. Output energy of the amplifier as a function of input intensity. A data point obtained using $SF_6$-$H_2$ rather than $H_2$-$F_2$ in the oscillator is also shown.

The amplified spontaneous emission for an input intensity of $10^4$ W/cm$^2$ decreased about a factor of three from the value measured when there was no probe beam into

the amplifier. Increasing the input power above this level did not further reduce the amplified spontaneous emission. These results are not understood at this time but may be due to parasitic modes.

To determine the effect of a different input spectrum on the energy extracted, the oscillator was operated using a mixture of $SF_6$-$H_2$. This gave a spectrum that contained vibration-rotation lines from only the first three vibrational levels rather than the first six obtained when mixtures of $H_2$ and $F_2$ were used. The peak input intensity was $10^6$ W/cm$^2$, and the energy extracted was 25 joules. While there are no experimental data using $H_2$-$F_2$ mixtures in the oscillator at this same power level, the curve of Fig.15 indicates that we would expect to extract about 80 joules. This measurement indicates that, for efficient energy extraction from an amplifier using $F_2$ and $H_2$, it is necessary to use an oscillator spectrum that contains vibration-rotation lines from the first six vibrational levels.

The time-integrated spectrum from the output of the amplifier was measured and compared with the oscillator input. This comparison is shown in Table II. As the table indicates, a few weak lines that are observable in the oscillator spectrum are not observable in the amplified spectrum.

The amplified beam quality was compared with the oscillator beam quality using the thin-film ablation technique that was described in the last semiannual report. Figure 16 shows this comparison. Within the limits of this technique, which are pointed out in the section on oscillator characteristics, the input and output energy distributions are identical. The next series of experiments will use a near diffraction limited beam from an $SF_6$-HI discharge oscillator which will permit a more critical evaluation of beam quality limitations imposed by the amplifier.

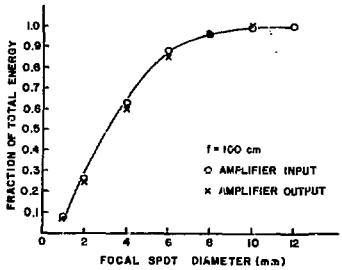


Fig. 16. A comparison of input and output energy distribution as a function of focal spot diameter.

Objective of High-Quality Discharge-Initiated SF6-HI Oscillator-Preamplifier System

The HF-laser research program at Sandia is currently directed toward evaluating energy extraction techniques from electron-beam-driven amplifiers containing mixtures of $H_2$, $F_2$, and $O_2$. One facet of this program requires a high-quality (2X diffraction limited divergence) oscillator-preamplifier chain with sufficient power density (> $10^5$ W/cm$^2$) at the $H_2$-$F_2$ amplifier to extract a significant fraction of the available energy. This system needs to include a large percentage of HF vibrational-rotational lines extending from $v = 1$ to $v = 6$ in order to efficiently probe the final amplifier. Initial experiments are to include determination of net energy extraction, comparison of beam quality before and after the final amplifier, and documentation of focusability of the final beam. All of these experiments can be accomplished with a long pulse oscillator-preamplifier (~ 100 ns). However, for future experiments, the system must be converted to a system with a relatively short pulse width (~ 5 ns).

TABLE II

Spectral Comparison Between the Amplifier Input and Output

| | Input | Output | | Input | Output | | Input | Output | | Input | Output |
|---|---|---|---|---|---|---|---|---|---|---|---|
| $P_1(4)$ | - | VW | $P_2(4)$ | VW | W | $P_4(4)$ | - | VW | $P_6(4)$ | M | M |
| $P_1(6)$ | M | M | $P_2(5)$ | S | S | $P_4(5)$ | M | S | $P_6(5)$ | M | M |
| $P_1(7)$ | S | S | $P_2(6)$ | VS | VS | $P_4(6)$ | M | S | $P_6(6)$ | M | M |
| $P_1(8)$ | S | S | $P_2(7)$ | VS | VS | $P_4(7)$ | S | S | $P_6(7)$ | VW | VW |
| $P_1(9)$ | VS | VS | $P_2(8)$ | VS | VS | $P_4(8)$ | S | S | $P_6(8)$ | VW | - |
| $P_1(10)$ | VS | VS | $P_2(9)$ | VS | VS | $P_4(9)$ | M | S | $P_6(9)$ | VW | - |
| $P_1(14)$ | M | W | $P_2(10)$ | VS | VS | | | | | | |
| $P_1(15)$ | W | W | $P_2(14)$ | W | - | $P_5(4)$ | W | M | | | |
| $P_1(16)$ | W | M | | | | $P_5(5)$ | M | S | | | |
| $P_1(17)$ | W | VW | $P_3(4)$ | M | S | $P_5(6)$ | S | S | | | |
| $P_1(18)$ | VW | VW | $P_3(5)$ | VS | VS | $P_5(7)$ | S | S | | | |
| $P_1(19)$ | VW | - | $P_3(6)$ | VS | VS | $P_5(8)$ | M | M | | | |
| $P_1(20)$ | VW | - | $P_3(7)$ | VS | VS | $P_5(9)$ | M | M | | | |
| $P_1(21)$ | VW | VS | $P_3(8)$ | VS | VS | $P_5(10)$ | VW | VW | | | |
| | | | $P_3(9)$ | S | M | | | | | | |

---

The first choice for an oscillator-preamplifier system meeting the above requirements would be based on $H_2$-$F_2$ mixtures, but this would require much development and the program milestones time scale did not permit this luxury. After studying alternate systems,[2] a system was designed using electric discharges in $SF_6$-HI mixtures for two reasons. First, the design could utilize the proven technology of a pin-discharge-initiated oscillator and Marx-driven amplifiers[3,4] (these systems have been successfully demonstrated at LASL using $SF_6/C_2H_6$ mixtures). Secondly, electric discharges in $SF_6$-HI mixtures have been shown to yield laser action on HF vibrational-rotational lines from v = 1 through v = 6.[5]

The characteristics of the oscillator-preamplifier system that was developed are discussed in this section. A schematic drawing of the system is shown in Fig. 17.

Briefly, the system consists of a pin-discharge oscillator operating in the $TEM_{00}$ mode, a 4X beam expander with a spatial filter, a 2.5-cm-diameter preamplifier, a 2.6X beam expander, and a 3.75-cm-diameter final preamplifier. The output of the final preamplifier is expanded to match the diameter of our electron-beam-initiated 200-joule amplifier. Table III gives the beam diameter, energy and divergence of the system at various locations along the chain. A more detailed discussion of the individual components as well as experimental data will be given in the following sections. In addition, the short-pulse option is discussed as well as a possible upgraded oscillator-preamplifier system using $H_2$-$F_2$-$O_2$ mixtures and electron beam excitation.

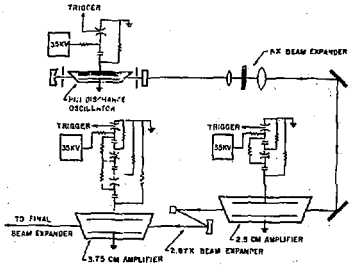


Fig. 17. Schematic of the high quality, long-pulse discharge initiated $SF_6$-HI laser system.

## Pin-Discharge-Initiated Oscillator and First Beam Expander

The physical characteristics of this system are similar to those presented in Refs. 3 and 4. The discharge takes place between a double row of pins and a cylindrical rod across a 15-mm gap. The pins in each row are spaced 6.4 mm apart and the rows are separated by 6.4 mm. The discharge region extends 80 cm and is driven by a 0.02-$\mu$F capacitor charged to 35 kV.

The oscillator cavity is 110 cm long and consists of a 5-metre-radius-of-curvature copper mirror and a ZnSe flat with one side AR coated. In order to obtain $TEM_{00}$ operation, apertures were placed at each end of the cavity. The starting point for the determination of the size of these apertures was a calculation of the $TEM_{00}$ mode spot size at each mirror. The apertures should be typically 1.5 times the $1/e^2$ points of the Gaussian beam. From this point, one must experimentally adjust the aperture until stable operation of the laser is obtained. The apertures used here are 3.5-mm diameter and 5.4-mm diameter, with the latter being at the output coupler.

The first beam expander consists of two $BaF_2$ lenses (chosen to minimize dispersion with a 200-$\mu$-diameter spatial filter at the mutual focus. Expansion ratios of 4.1 and 5 have been used in these experiments.

Beam divergence before and after the first beam expander was obtained by measuring the focused spot size. These results are presented in Table III. Figure 18 shows the focused spot profile, taken after the beam expander. The profile was determined by scanning a detector with a 200-$\mu$-diameter aperture across the focused beam using a 5-metre-focal-length mirror. The dashed curve in the figure is a least-squares fit to a Gaussian profile. The beam profile directly out of the oscillator was also determined during these experiments and was found to be consistent with a Gaussian profile. The measured waist size (Table III) was about 50-percent larger than expected from calculations.

The single-mode output of the oscillator was 10 mJ (150 ns) using a 20:1 mixture of $SF_6$:HI. The output varied somewhat with overall pressure and, more importantly, the spectral content varied with overall pressure. The HF ($v = 5, 6$) lines were particularly sensitive to pressure, vanishing

for pressures greater than 95 torr. Time histories of each line of the 30 or more lines were obtained for total pressures of 70 torr and 90 torr in order to determine the optimum conditions for matching the $H_2$-$F_2$ electron-beam-initiated amplifier spectrum. Table IV shows the lines present in the oscillator spectrum at 70 torr, as well as those present in the $H_2$-$F_2$ system (when configured as an oscillator) and those present in the $SF_6$-HI preamplifier (when configured as an oscillator). The matchup is reasonably good, provided that temporal matching also occurs. Examination of the individual time histories (Fig. 19) shows that there are time intervals where a majority of the lines are coincident in time.

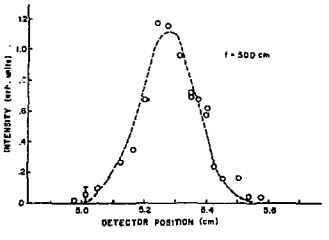


Fig. 18. Focal spot intensity distribution of the oscillator output. The dashed line is a least squares fit to a Gaussian profile.

TABLE III

Beam Characteristics of $SF_6$-HI Oscillator Preamplifier System

| Location | Beam Diameter | Energy | Full Angle Divergence | Ratio of Measured to Calc. Diff. Limited Divergence |
|---|---|---|---|---|
| Oscillator | 0.35 cm | 10 mJ | 2.0 mrad | 1.5 |
| Output of First Beam Expander | 1.5 ± 0.2 cm | 10 mJ | 680 μrad | 1.5 |
| Output of 2.5 cm Preamp | 1.5 ± 0.2 cm | 190 ± 40 mJ | 760 μrad | 1.7 |
| Output of Second Beam Expander | 3.6 ± 0.2 cm | 190 ± 40 mJ | 330 μrad | 1.7 |
| Output of 3.75 cm Preamp | Apertured to 3.3 cm | 1.1 ± 0.1 J (1.5 J, Unapertured) | 420 μrad | 2.0 |
| Output of Final Beam Expander | 6.6 cm | 1.1 ± 0.1 J (1.5 J, Unapertured) | 200 ± 50 μrad | 2.0 |

TABLE IV

Spectral Comparison of $SF_6$-HI Discharge System With Electron-Beam Initiated $H_2$-$F_2$ Oscillator

| | $H_2$-F2 | $SF_6$-HI | | $H_2$-$F_2$ | $SF_6$-HI | | $H_2$-$F_2$ | $SF_6$-H |
|---|---|---|---|---|---|---|---|---|
| $P_1(4)$ | - | O | $P_2(7)$ | VS | A O | $P_4(7)$ | S | A O |
| $P_1(5)$ | - | O | $P_2(8)$ | VS | A O | $P_4(8)$ | S | A O |
| $P_1(6)$ | M | A O | $P_2(9)$ | VS | A | $P_4(9)$ | M | A O |
| $P_1(7)$ | S | A O | $P_2(10)$ | VS | | | | |
| $P_1(8)$ | S | A O | $P_2(14)$ | W | | $P_5(4)$ | W | A O |
| $P_1(9)$ | VS | A | | | | $P_5(5)$ | M | A O |
| $P_1(10)$ | VS | A | $P_3(4)$ | M | A O | $P_5(6)$ | S | A O |
| $P_1(14)$ | M | | $P_3(5)$ | VS | A O | $P_5(7)$ | S | A O |
| $P_1(15)$ | W | | $P_3(6)$ | VS | A O | $P_5(8)$ | M | A O |
| $P_1(16)$ | W | | $P_3(7)$ | VS | A O | $P_5(9)$ | M | A O |
| $P_1(17)$ | W | | $P_3(8)$ | VS | A O | $P_5(10)$ | VW | A O |
| $P_1(18)$ | VW | | $P_3(9)$ | S | A O | | | |
| $P_1(19)$ | VW | | | | | $P_6(4)$ | M | |
| $P_1(20)$ | VW | | $P_4(4)$ | - | A O | $P_6(5)$ | M | O |
| | | | $P_4(5)$ | M | A O | $P_6(6)$ | M | O |
| $P_2(4)$ | VW | A O | $P_4(6)$ | M | A O | $P_6(7)$ | VW | |
| $P_2(5)$ | S | A O | | | | $P_6(8)$ | VW | |
| $P_2(6)$ | VS | A O | | | | $P_6(9)$ | VW | |

O - Oscillator transition

A - Amplifier transition

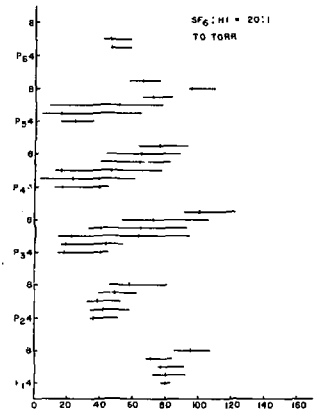


Fig. 19. Time history of the laser transitions from the oscillator using gas mixtures of $SF_6$-HI.

Most of the diagnostics described here were also performed with mixtures of $SF_6$-$C_2H_6$. The beam quality was essentially identical with that when $SF_6$-HI was used and typically about twice the energy was extracted from the system [although only HF (v = 1 to v = 3) lines were present]. Since the HI mixtures tended to be unstable (HI photodissociates), the ethane mixtures provided a source for system setup and checkout prior to introducing the HI. The $SF_6$-HI mixtures were stored at a temperature of 7°C and, after passivating the container, were usable for a period of several months.

## Fast-Discharge-Initiated Preamplifiers

The two preamplifiers in the system are each excited by a discharge between two Rogowski shaped electrodes. The first preamplifier (2.5-cm aperture) has an excitation volume of 2.5 cm x 2.5 cm x 50 cm. The second preamplifier (3.75-cm aperture) has an excitation volume of 3.75 cm x 3.75 cm x 50 cm. The discharge for both of the amplifiers is driven by fast Marx banks. The two-stage Marx for the 2.5-cm-aperture amplifier contains two 0.04-$\mu$F capacitors. Each capacitor is normally charged to 35 kV. This produced an initial voltage of 70 kV across the discharge region. The Marx for the 3.75-cm-aperture amplifier is a three-stage Marx with three 0.04-$\mu$F capacitors, which are each charged to 35 kV. This produces an initial voltage of 105 kV across the discharge region.

The preamplifiers were initially tested by putting the amplifiers in a cavity consisting of a sapphire flat for an output coupler and a totally reflecting 5-metre mirror. Studies of energy output for different mixtures and pressures of $SF_6$-$C_2H_6$ and $SF_6$-HI, and different discharge voltages were made. The relative output in the 2.5-cm-diameter amplifier as a function of the initial charge voltage on the capacitors is shown in Fig. 20 for an $SF_6$-HI mixture of 20:1. The total output energy was not sensitive to the gas mixture using $SF_6$:HI ratios between 15:1 to 20:1. Although the total stored energy can be increased by increasing the voltage across the discharge, 35-kV charge per capacitor was chosen for both preamplifiers in order to minimize voltage breakdown problems. At this charge voltage, a maximum of 0.6 J from the 2.5-cm-amplifier and 1.5 J from the 3.75-cm amplifier was obtained using $SF_6$-HI (20:1) mixtures. With $SF_6$-$C_2H_6$ (15:1) mixtures, a maximum of 1 J was obtained from the 2.5-cm amplifier and 4.0 J was obtained from the 3.75-cm amplifier. It is interesting to note that, although the excitation volume for the 3.75-cm amplifier is two times that of the 2.5-cm amplifier, the energy obtained is nearly four times that of the 2.5-cm amplifier. As each preamplifier was inserted into the system, the relative oscillator-preamplifier timing required for maximum energy extraction was determined

by locating the time for onset of amplified spontaneous emission (ASE) in the preamplifier. This is the time at which laser action occurs with no external feedback and proves to be the optimum time for energy extraction by the oscillator pulse. Finally, the energy extraction as a function of amplifier pressure was determined. A typical result is shown in Fig. 21 for a 2.5-cm-aperture preamplifier. The overall system jitter (trigger input to laser pulse output) was less than 10 ns.

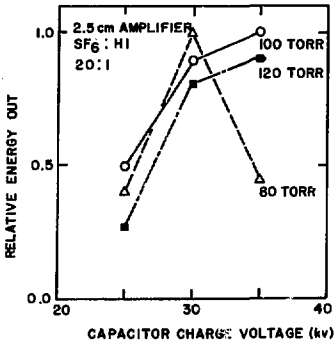


Fig. 20. Output energy from the 2.5 cm diameter preamplifier run as an oscillator as a function of gas pressure and charge voltage.

Reflecting Beam Expanders for Oscillator-Preamplifier System

The beam expander between the 2.5-cm-aperture amplifier and the 3.75-cm-aperture amplifier as well as the final beam expander are constructed using reflecting optics. Although the first beam expander is constructed from refracting optics, calculations indicate

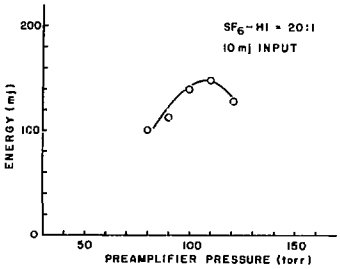


Fig. 21. Relative gain of the preamplifier as a function of pressure for a fixed $SF_6$:HI ratio of 20:1.

that it is not possible to continue to use refracting optics throughout the chain due to the dispersion that would be introduced into the chain. However, the use of reflecting optics is not without problems. In order to keep the cost of the reflecting elements reasonable, off-axis-spherical mirrors are used instead of off-axis parabolas. Care must be taken so that the divergence due to off-axis aberrations is not excessive. The criteria used for these optical elements were

$$\text{Sagittal Comma } \beta = (0.0625\,\theta/F/D)^2 \ll \beta_{DL}$$

$$\text{Astigmatism } \beta = 0.5\,\theta^2/F/D) \ll \beta_{DL}$$

where

$$\beta_{DL}(\text{diffraction limited}) = 2.44\,\lambda/D\,.$$

The angular width of the beam is $\beta$, the diameter of the beam on the mirror is D, and F is the focal length of the mirror. The angle $\theta$ is the angle between the incident and reflected beams.

The second beam expander is constructed from a 1.5-metre-radius-of-curvature convex mirror and a 4.0-metre-radius-of-curvature concave mirror, giving a beam expansion of 2.67. The final beam expander, chosen to match the aperture of the $H_2$-$F_2$ amplifier (not shown in Fig. 19), was constructed from 5-metre-radius-of-curvature convex mirror and a 10-metre-radius-of-curvature concave mirror giving a final beam expansion of two.

## Beam Quality of Discharge-Initiated Oscillator-Preamplifier System

The beam diameters and the measured divergence angles for the electric-discharge-initiated oscillator-preamplifier system are summarized in Table III. The oscillator divergence was determined as previously mentioned by measuring the focused spot profile (Fig. 18). The laser beam divergence was also measured subsequent to the first preamplifier and after the final preamplifier. The technique used to measure the divergence utilized multiple reflections from one surface of a ZnSe wedge. The resultant beams, each increasingly attenuated, were then focused onto a thin bismuth film and the diameter of the ablated spot was determined. The small thickness of the film (400 → 800 μm) provides a reasonably sharp ablation threshold. The relative attenuation factor for each reflection has been calibrated using an HeNe laser and a photodiode. Intensity as a function of focal spot diameter is shown in Fig. 22 for the oscillator and both preamplifiers but without the final (2X) beam expander. Also shown are the data for extraction from the 2.5-cm-aperture preamplifier only, and the 3.75-cm-aperture preamplifier only. These data were taken by not charging one amplifier. For each case, the initial beam diameter was 3.3 cm. Clearly the beam is somewhat degraded by the large amplifier, and relatively more energy is present at large divergence when this amplifier is saturated. This technique was not used in conjunction with the final beam expander due to the off-axis astigmatism introduced when allowing for the greater beam diameter.

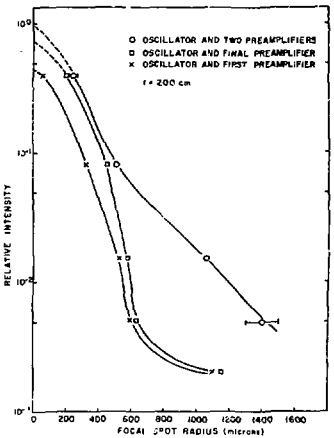


Fig. 22. Focal spot intensity distribution for various configurations of the oscillator-preamplifier system.

In addition to this technique for divergence measurements, shear-plate interferometry was applied to the beam at various locations. In order to obtain a usable pattern, the pattern from the shear plate was focused onto Polaroid film. These results were in agreement with the focused-beam results before the final expander and gave a value of 200 ± 50 μm radian full-angle divergence at the final output. Moreover, some phase distortions were present in the beam, but the distortions were no worse than $\lambda/2$ over the entire wavefront. This technique will be applied to the beam at various points along the optical path both before and after the electron-beam-initiated final amplifier in order to check the various mirror surfaces and to determine the beam degradation due to the amplifier.

## Short Pulse Option for Discharge Initiated $SF_6$-HI System

The beam from the final electron-beam-initiated $H_2$-$F_2$ amplifier should be near-diffraction limited with a high contrast ratio. The pulse length requirements for laser fusion are of the order of a few nanoseconds. The previous sections have discussed the development of a long-pulse oscillator-preamplifier chain that will be used to study the extraction of energy from large-volume $H_2$-$F_2$ amplifiers. In this section we will discuss the development of a technique for generating a short pulse from an oscillator-preamplifier chain. In addition to generating a short pulse, it is necessary that the technique be capable of controlling ASE in the preamplifier. The technique of polarization rotation, where the polarization of the beam is rotated 90 degrees for a few nanoseconds, has been discussed previously[2] and has been demonstrated using mixture of $SF_6$-$C_2H_6$.[6] With this technique the ASE will be suppressed because a photon flux will be in the preamplifiers at all times.

The next generation of experiments will require that this technique be demonstrated for our $SF_6$-HI oscillator-preamplifier chain. Currently, a high-optical-quality oscillator and preamplifier with the short pulse generation capability is under development. The final system that will be used is shown in Fig. 23. The oscillator, operating in the $TEM_{00}$ mode, is polarized as indicated in the figure. At the desired time in the 100-ns-long pulse, the output polarization of the oscillator output is rotated for a fixed time period. The entire pulse, including both polarizations, is then amplified by the two succeeding preamplifiers. The short pulse is split off after the final preamplifier by a brewster-angle beam splitter. All of the components with the exception of the EO crystal and polarizer are currently being used for the long-pulse laser system described in the previous section. The components that will be added to the existing chain are a polarizer and the EO crystal. A final brewster-angle polarizer will be added at the end of the amplifier chain in order to separate the short pulse from the total pulse. Currently, a ZnSe wedge (7.6 cm x 25.4 cm) and a quartz wedge are available. About 49 percent of the energy in the short pulse will be reflected with the ZnSe, while 14 percent will be reflected using the quartz wedge.

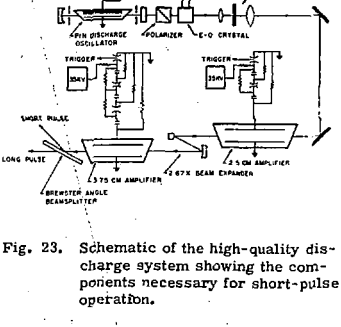


Fig. 23. Schematic of the high-quality discharge system showing the components necessary for short-pulse operation.

Currently, a $TEM_{00}$-mode pin-discharge oscillator and a 2.5-cm-diameter preamplifier are being constructed. Experiments on the system should begin in the near future with a target date of February for a working system.

## $H_2$-$F_2$ Electron-Beam-Initiated Oscillator-Preamplifier System

An attractive possibility for a high-quality oscillator-preamplifier system whose spectrum would match those of an $H_2$-$F_2$ amplifier is one using the same chain reaction. Some initial experiments along this line have been performed at Sandia.

A 20-cm-long high-pressure laser cell has been constructed and is designed to operate with $H_2$-$F_2$-$O_2$ mixtures of up to 4 atmospheres. The mixture is ignited with a 300-keV or 600-keV electron beam (3 ns, 10 joules) from a Febetron 706 fitted with an extended diode. The electron beam is guided into the λ-geometry cell with a 4-kG magnetic field. This laser can be operated at various pressures and concentrations so that it will produce pulse widths similar to that of our pin-discharge oscillator. Therefore, by the correct choice of cavity components and apertures, the oscillator can be made to operate in the $TEM_{00}$ mode. The preamplifiers would be initiated by similar electron-beam machines, but they could have shorter pulse widths since the laser is expected to produce pulses as short as 10 ns at the maximum pressure. The final oscillator-preamplifier chain would be similar to that shown in Fig. 7. However, taking advantage of the inherently high efficiency of an electron-beam initiated laser using $H_2$-$F_2$-$O_2$ mixtures, one might expect an output of approximately 2 joules for an oscillator-single-preamplifier chain. The electron-beam-initiated oscillator-preamplifier system would be configured much like that shown in Fig. 23.

In order to demonstrate the feasibility of an oscillator-preamplifier chain based on the $H_2$-$F_2$ reactions, one must first demonstrate that a high-optical-quality laser beam is obtainable from such an oscillator. Moreover, the efficiency and spectral content must be determined for initiation levels of a few joules and compared with earlier high-energy experiments. In order to meet program milestones on time, work on this backup oscillator-preamplifier system has been postponed so that more effort could be placed on construction and testing the discharge system. If the spectra obtained from lasers using mixtures of $SF_6$-HI do not contain enough lines to extract a significant amount of energy from electron-beam initiated $H_2$-$F_2$ lasers, this work will resume.

## Chamber for HF-Laser Focusing Experiments

One of the HF-laser program milestones scheduled for completion in early FY 78 is to focus energy from an electron-beam initiated HF laser system through small diameter pinholes (≤ 400 μm) in order to demonstrate focusability. Because of the power densities involved, air breakdown problems would be encountered unless the experiments were carried out in an evacuated chamber. In order to perform such focusing experiments, a vacuum chamber and optical system have been designed and constructed so that a 7.6-cm-diameter collimated laser beam can be reflected from an off-axis copper parabolic mirror to the focal spot. The vacuum chamber incorporates a calorimeter to measure the energy transmitted through the pinhole, as well as the off-axis mirror and pinhole assemblies. The chamber has been constructed so that initial mirror and pinhole alignment can be performed while opened to the atmosphere without moving the position of the optically flat laser beam transmission window on the vacuum chamber. The system has also been designed so that the six degrees of rotational and translation motion of the mirror mounting assembly and three degrees of translation for the pinhole mount can be remotely adjusted from outside the chamber after evacuation. A number of observation ports are included so that the mirror mounting and pinhole mounting assemblies can be viewed from the outside of the chamber. The chamber is also designed to accommodate a probe laser beam to investigate pinhole closure times.

A diagram of the laser beam chamber is shown in Fig. 24. The chamber is 1.8 m long and has a diameter of 76 cm. The chamber is mounted on a stand that permits alignment of the chamber with the incoming laser beam. The laser-beam window has a 14-cm clear diameter while the main observation port at the opposite end of the

chamber accommodates a 24-cm-diameter window. Three pinhole-viewing windows (two of which are on one side of the chamber with the third on the opposite side) have a diameter of 11.4 cm. The chamber incorporates a solid steel optical bench with a three-position leveling arrangement in order to align the plane of the bench parallel with the incoming HF laser beam. A diagram of the optical bench, mirror, pinhole, and calorimeter is shown in Fig. 25. The 43- by 97-cm optical bench is large enough to accommodate 10-cm-diameter parabolic mirrors with an offset of 10 cm from the inside edge of the mirror to the axis of the parabola. Gold-coated glass mirrors with a focal length of 46 cm have been obtained for initial focusing studies. Solid copper mirrors having a 25-cm focal length were obtained also and are currently undergoing final polishing with an outside contractor.

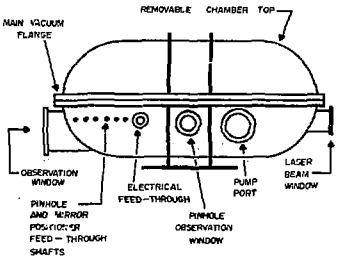


Fig. 24. Diagram of the laser beam chamber for focusing HF laser energy through small diameter pinholes.

Commercially available mirror mounts and a translational mount for the pinhole were modified so that they could be actuated with rotary feed-through drive units mounted in the vacuum chamber. Additional modifications of the mirror mounts were made in order to more accurately control the position of the focal spot within the aperture of the pinhole.

Initial focusing procedures are to be initiated shortly using a 10-cm-diameter collimated He-Ne laser beam to align the off-axis parabolic mirror such that its focus corresponds to the geometric position of the pinhole. Also, the expanded He-Ne beam is to be used in facilitating initial alignment of the mirror and pinhole assembly with the HF laser beam.

## Computer Study of Parasitic Oscillations in HF Amplifiers and Oscillators

In the previous semiannual report, an approximate treatment for parasitic oscillations in directions transverse to the optical axis was described and incorporated into the HF laser code. Parametric studies have since been carried out. A number of unexpected results were obtained and will be presented here. The results for oscillators have also been obtained using a simple one-point, single-transition cavity rate equation treatment. This simple treatment will be used to conveniently illustrate the underlying mechanisms for the oscillator results.

Some representative results of the parametric study are shown in Figs. 26 through 28. These are calculations of electron-beam-initiated HF oscillator and amplifier performance for the approximate geometry, gas mixture, and input-signal conditions of Sandia's REBA experiments.[7] Figure 26 illustrates the predicted variation of oscillator output energy with wall reflectivity. When the gain threshold, for parasitics falls below the oscillator gain threshold, quasi-steady-state theory predicts a discontinuous decrease in oscillator output. The more inclusive theory embodied in our code predicts a smooth transition, as shown, with important parasitic degradation even when the parasitics threshold is greater than the oscillator threshold. Figure 27 illustrates the variation of amplifier output energy with wall reflectivity. Additional results not shown

demonstrate that parasitics become increasingly important with increasing pressure. Figure 28 shows the parasitics-limited oscillator output energy as a function of $H_2$ partial pressure. The predicted decrease in output energy with increasing $H_2$ partial pressure beyond about 50 torr is caused by parasitics. The general trend illustrated here has been confirmed experimentally and is shown in Fig. 6. In addition to the above results, the HF code has also shown that increasing the cavity length for a fixed active-medium length will enhance parasitic oscillation. Recent experimental results shown in Fig. 10 are consistent with this prediction.

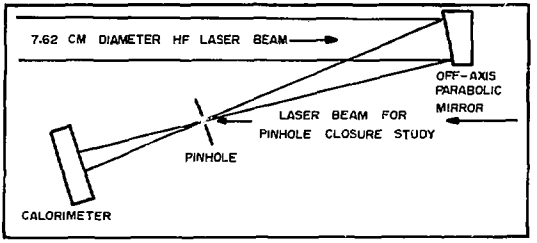


Fig. 25. Diagram of the optical bench for mounting the mirror, pinhole and calorimeter within the laser beam chamber.

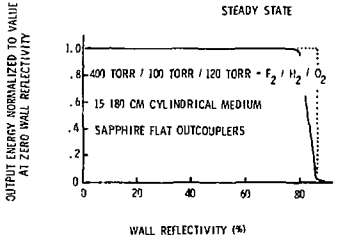


Fig. 26. Performance of HF oscillator as a function of parasitic wall reflectivities.

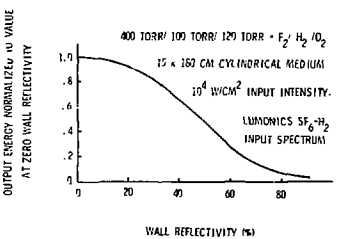


Fig. 27. Performance of HF amplifier as a function of parasitic wall reflectivities.

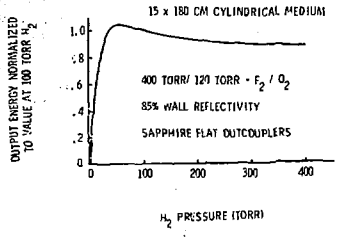


Fig. 28. Performance of parasitics-limited HF oscillator as a function of $H_2$ pressure.

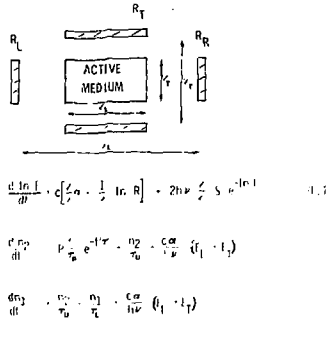


Fig. 29. Schematic and equations for simple model of parasitics-limited oscillator.

All of the predicted trends for parasitics-degradation of oscillator performance obtained with the HF code have been duplicated using the simple one-point treatment mentioned earlier. Figure 29 shows a schematic of the one-point model and the associated equations for a single-transition four-level model. The subscripts L and T denote longitudinal and transverse directions. The active-medium and cavity dimensions $\ell$ and $\mathscr{L}$ and the reflectivities R are illustrated. The cavity radiation densities are given by E, and the gain coefficient $\alpha$ and spontaneous emission term S are calculated in terms of the upper- and lower-level number densities $n_2$ and $n_1$. Pumping strength is denoted by P, and the various characteristic times are given by $\tau$. Binary scaling of collisional processes and Lorentz broadening of the line profile are assumed. Figure 30 shows results for oscillator output as a function of wall reflectivity at various gas pressures. Numerical values for the various governing parameters are shown on the figure and were chosen to approximate conditions of Sandia's electron-beam-initiated HF-laser experiments. As also predicted by the HF code, parasitics degradation is seen to become increasingly severe with increasing pressure. This is shown again in Fig. 31, which also illustrates the enhancement of parasitics by increased cavity length.

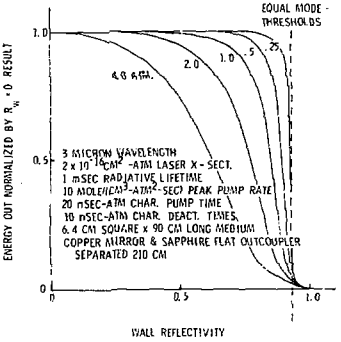


Fig. 30. Effect of wall reflectivity and pressure on parasitic-oscillation degradation of oscillator performance.

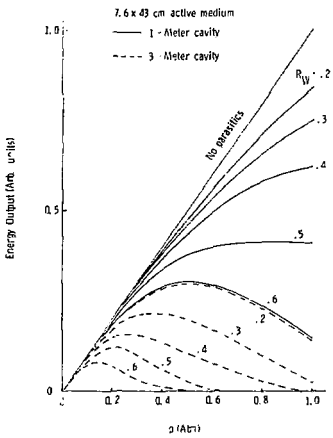


Fig. 31. Effect of wall reflectivity, cavity length, and pressure on oscillator output.

An important characteristic of all of the foregoing results is that parasitic oscillations occur despite the fact that the gain threshold for parasitics exceeds the cavity threshold. This is shown to be attributable to transients as follows. The gain thresholds are shown in Fig. 32, along with representative energy-density and gain time-histories. Severe gain overshoot is evident. During the period of overshoot for a mode, the associated radiative energy density increases. The reason that transverse (parasitic) radiation increases faster than the longitudinal radiation, initially, is shown in Fig. 33. The rate of increase of radiation (essentially $(\ell/\mathcal{L})\alpha + (1/\mathcal{L})\ell n_e R$) is plotted versus $\alpha$ for each mode. While the values of R and $\ell$ dictate a greater abscissa intercept (gain threshold) for the transverse-radiation result, the values of $\ell/\mathcal{L}$ dictate a greater slope as well. Thus, in this case, for sufficiently large gain overshoot, the parasitic oscillation builds up faster than the desired cavity oscillation. It is now clear that increasing either pressure or $\mathcal{L}_L$ will enhance the parasitics.

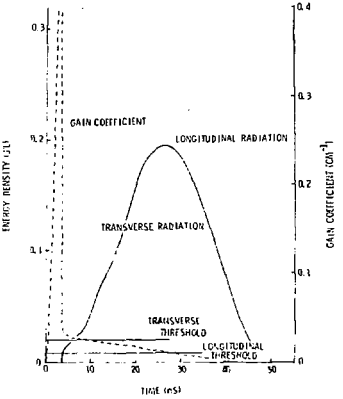


Fig. 32. Representative energy-density and gain-coefficient time histories at one atmosphere with 85 percent wall reflectivity.

The work described above permits some insight into the existing experimental results and suggests conditions that must be avoided if parasitic oscillations are to be minimized. A less restrictive treatment of the directional-dependence of parasitics radiation has subsequently been formulated. It is anticipated that formulation would bring the HF code into better agreement with experimental data. This more refined formulation will be implemented as time and necessity dictate.

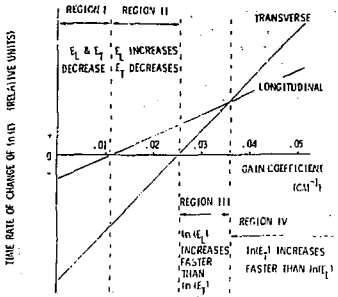


Fig. 33. Relative magnitudes of time rate of change of oscillator and parasitic radiative-energy density as a function of gain coefficient.

## Kinetics Upgrade of HF-Laser Code

Following a review of our HF-laser predictive capabilities, ERDA/DLF suggested specific measures be taken in order to upgrade the kinetics packages of the HF computer code. Of prime concern was the large overprediction of light-output pulse width when electron-beam dissociation of $F_2$ was assumed to cost 10 eV of deposited energy per F-atom produced, the widely accepted value. The specific measures that were taken were:

1. Add the chain-terminating reactions involving oxygen, as privately transmitted by Dr. Ray Taylor of Physical Sciences, Inc. (PSI).

2. Add the multiquantum HF-HF vibration-translation exchange, scaling with vibrational level v as $v^{2.3}$, as recently implemented by Dr. J. J. T. Hough.[8]

3. Add the updated Lorentz-broadening treatment as recently described in the literature.[8]

4. Bring all other data in the HF code reaction package up-to-date with the codes at PSI and Aerospace Corp.

5. Compare computed results with experimental data reported by Dr. J. Mangano[9] of Avco Everett Research Lab.

6. Recompute the results corresponding to Sandia's experiments, with an F-atom cost of 10 eV.

Figure 34 shows computed results for a standard test case first calculated by the code RESALE.[10] For this case, the active medium length is 100 cm, with mirror reflectivities 0.8 and 1.0. The initial pressure is 1.207 atm, and the initial mixture is $F_2/H_2/F/Ar$ = 1/1/0.1/50. RESALE predicted 0.101 joule/cm$^3$ output energy, Hough's code SPIKE predicted 0.089 joule/cm$^3$, and Sandia's modified code HFOX predicts 0.058 joule/cm$^3$. The differences in output energy and pulse shape are expected in view of the many differences between the three codes. The most important differences were as follows: RESALE did not allow gain overshoot, and RESALE and SPIKE did not allow rotational nonequilibrium or multiquantum HF-HF V-T exchange.

Figure 35 shows computed results for Mangano's 30 percent $F_2$ case,[9] assuming 12 eV per F atom. An updated version of SPIKE predicted 0.0225 joule/cm$^3$ output, the PSI code predicted 0.0320 joule/cm$^3$, and HFOX predicts 0.0160 joule/cm$^3$, while experiment indicates 0.051 joule/cm$^3$. No record of the experimental output time history is available, although the pulsewidth (FWHM) is reported as 2.0 μs. A number of differences exist between the three codes in this case also: SPIKE did not include the oxygen kinetics, the PSI code used $v^{2.0}$ rather than $v^{2.3}$ scaling for the HF-HF multiquantum V-T rate, both the PSI code and SPIKE assumed that all the F atoms

were made instantaneously at t = 0, while HFOX simulated production over 200 ns, corresponding to the electron-beam duration, and only HFOX included spatial nonuniformity and rotational nonequilibrium. It should be mentioned that the three time histories shown in Fig. 25 each have slightly different definitions. The SPIKE result is output power, directly. The HFOX result is power incident on the output coupler, and, therefore, should be multiplied by the transmissivity, 0.9, to get output power. The PSI result is "intracavity flux" and should be multiplied by $-(\ell n_e R)/(2L) = 1.15$ to get output power.

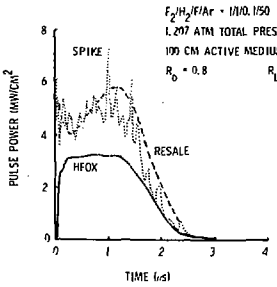


Fig. 34. Various code predictions of pulse power for standard test case.

Finally, for one of Sandia's REBA experiments,[7] with 10 eV per F atom cost, HFOX predicts a relatively long low-power output pulse (hundreds of ns, 30 MW/cm$^2$) compared with experiment (50 ns, 200 MW/cm$^2$). Thus it appears at this time that the code upgrading has not resolved the problem of pulsewidth overprediction for intense-excitation cases. The reason of the disagreement between prediction and experiment remains a matter of current investigation.

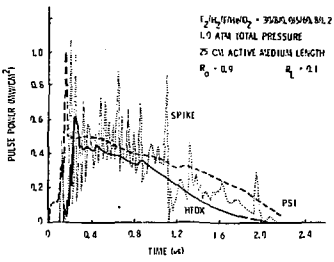


Fig. 35. Various code predictions of pulse power for Mangano's $F_2$-rich code.

## Repetitively Ignited Flowing H2-F2-O2 Mixtures

The purpose of this study was to establish techniques and requirements for achieving stability against spontaneous detonations and to achieve an acceptable degree of uniformity in laser-type mixture slugs of gas flowing in a repetitively ignited $H_2$-$F_2$-$O_2$ system. Initial studies concerning slug separation had established that hydrogen injected repetitively into a flowing $F_2$-$O_2$ system could be isolated to the extent that a continuous combustion would not occur for slug injection rates up to 10 per second.[11] Although the initial data were obtained using Ar as a substitute for the $F_2$-$O_2$ mixture and He as a substitute for $H_2$, subsequent measurements with $F_2$-$O_2$ mixtures and $H_2$ have shown that an acceptable level of slug separation could be achieved with these gases.

The presently described study has been concerned with the determination of mixture uniformity occurring over the active mixture volume that, in the present case, would be equivalent to a laser cavity volume of 2 cm in diameter and 8 cm long. This corresponds to the ignition region[11] of the flowing system.

In order to examine the slug uniformity after injection and passage of the slugs through a 40-cm-long mixing region to the 8-cm-long ignition region, additional mass spectrometric data were obtained. For this study, the mass spectrometer probe was constructed to measure time-dependent concentrations at different points throughout the ignition region so that a three-dimensional number density profile of the slugs could be obtained. The mass spectrometer experimental arrangement used for this study is shown in Fig. 36. The time-dependent gas number densities within the ignition region of the flowing system were recorded using a digitized data recording system which converted the time-dependent gas concentration at the sampling probe into a digitized signal level recorded in a multichannel scaler. The signal levels for gas number densities at the sampling probe were calibrated using a series of gas mixtures obtained from Matheson, in order that absolute rather than relative concentrations could be obtained.

A concentration profile for a slug after passing into the ignition region is shown in Fig. 37. Although these data were obtained for the case where He was substituted for $H_2$, the concentration contours shown in the figure would be equivalent to the hydrogen concentration in an $H_2$-$F_2$-$O_2$ slug as it passes through the ignition region of the flowing system. The data shown were obtained using an He injection time of 30 ms and give an equivalent maximum hydrogen content of about 16 percent (as is used in most of our HF laser studies). Other gas composition ratios can be obtained by changing the diameters of the gas flow orifices at the injection head.

In examining the slug concentration contours (as shown in Fig. 37), a position of the slug with respect to the ignition region can be determined which will yield a minimum radial gradient in the preiginition index of refraction for a light path parallel to the mixture flow and extending through the 8-cm ignition region (Fig. 38). The preignition index of refraction at any point in the slug is:

$$n = \left[\alpha\left(n_{(F_2)} - 1\right) + \beta\left(n_{(O_2)} - 1\right) + \gamma\left(n_{(H_2)} - 1\right)\right]\frac{P}{P_o} + 1 \ , \qquad (1)$$

where $n_{(F_2)}$, $n_{(O_2)}$, and $n_{(H_2)}$ represent the index of refraction at 1 atm of $F_2$, $O_2$, and $H_2$, respectively, and $\alpha$, $\beta$, and $\gamma$ are the mole fractions of each gas such that $\alpha + \beta + \gamma = 1$. Under the conditions for obtaining the data shown in Fig. 37, $P = 1$ atm and $P/P_o = 1$. The average index of refraction, $n_{av}$, along any ray parallel to the flow and extending for an 8-cm path length through the slug (corresponding to the 8-cm-long ignition region) is

$$n_{av} = \frac{1}{Z - Z_o}\int_{Z_o}^{Z} n_Z dZ \ , \qquad (2)$$

where $Z_o$ is an arbitrary starting point for the ray at some point on the leading edge of the slug. The value of $n_{av}$ can be determined for an 8-cm-long ray along the center of the cylindrical ignition region and for other rays parallel to the flow farther out towards the wall of the ignition portion for the flow system such that $n_{av}(r)$ can be determined by any $Z_o$ to $(Z_o + 8)$ cm path through the slug which is at some fixed position in the ignition region (i.e., at a given instant of time). If $n_{av}(r)$ is determined over the 8-cm ignition region for a series of slug positions with respect to the ignition region, a region in the slug coinciding with the ignition region can be found where there is a minimum change in the value of $n_{av}(r)$ from the center of the flowing system ($r = 0$) out to the outer wall ($r = 1$ cm). In the case of the data shown in Fig. 37, a minimum change in $n_{av}(r)$ in the ignition region occurs when the maximum $H_2$ concentration has reached the down stream end of the ignition region (the

right-hand side of the ignition region as shown in Fig. 38). When the slug is located in such a position, the average $H_2$ concentration through the 8-cm ignition region changes by about 1 percent from the center of the flow to the outer wall. This yields a value of $\Delta n/n$ of about $\pm 3 \times 10^{-7}$ using indexes of refraction for $H_2$, $F_2$, and $O_2$ determined at the sodium D line under the conditions where $[F_2]:[O_2]:[H_2] \approx 1:0.3:0.25$ and P = 1 atm. This relatively small shift in the index of refraction would cause a wavefront distortion (over an active volume of 30 cm) of $\lambda/15$ for sodium D radiation. The slug uniformity was considered good enough at this time to conclude the mass spectrometric studies and proceed with stability studies at the remote test site using $H_2$ slugs in the flowing $F_2$-$O_2$ system.

The stability tests were carried out with the flow system as shown in Fig. 38 in conjunction with a charcoal reactor to dispose of the exhausted $F_2$ and traps to remove HF so that flow rates of $10^3$ cm/s could be studied. The $F_2$-$O_2$ mixtures were introduced into pressure containers at 400 psi and mixed by convective heating. For the initial flow studies, the $F_2$-$O_2$ and $H_2$ pressures delivered at the flow-limiting orifices of the injection head were about 170 psi, giving a flow velocity in the range of $10^3$ cm/s and a composition at the center of the slugs of $F_2$:$O_2$:$H_2$ = 1:0.4:0.25. Some of the pressure transducers (Fig. 38) were triggered simultaneously with $H_2$ slug injection in order to determine if slug stability could be maintained during slug injection, during flow through the mixing region, and during entrance into the ignition region such that no ignition would occur spontaneously through the system prior to arrival of the slug at the charcoal disposal trap.

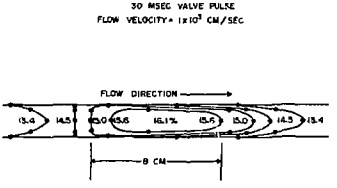


Fig. 37. The equivalent $H_2$ concentration occurring within a slug as it flows through the ignition region of the flowing system.

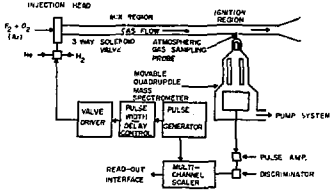


Fig. 36. Diagram of the mass spectrometer gas sampling system for quantitative measurement of gas concentrations within the mixture slugs.

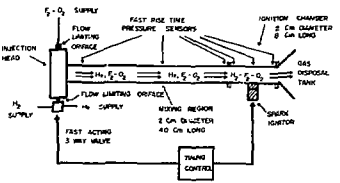


Fig. 38. A block diagram of the flowing system as was used at the remote test site to study stability in laser type mixtures of $H_2$, $F_2$, and $O_2$.

Initial tests of the flowing system indicated that ignition of the $H_2$ slugs occurred at the injection head during $H_2$ injection. The apparent reason for this initial lack of stability was that prepassivation of the system was incomplete because of the rapid removal of $F_2$ by the charcoal reactor. However, after continuous operation of the system, preignition ceased to occur and successful $H_2$ slug injection into the $F_2$-$O_2$ mixture and flow through the mixing and ignition regions took place.

Initial studies of the flowing system were carried out using 30-ms $H_2$ slug injection times. As indicated in Fig. 38, when the $H_2$ flow was off, He flow system was maintained through the $H_2$ injection ports of the $H_2$ flow system to maintain a time-independent gas flow rate in the system. A time-dependent oscilloscope trace of the output from a pressure transducer located in the ignition region of the flowing system is shown in Fig. 39, which was obtained using a repetition rate of two slugs/second. This trace shows a small pickup signal corresponding to the 30-ms $H_2$-valve opening pulse and is followed by a large pressure excursion occurring 100 ms after $H_2$ injection. From the known flow velocities it was determined that slug detonation occurred within the charcoal trap downstream from the ignition region rather than in the mixing or ignition regions of the flowing system. Thus, from repeated runs as shown in Fig. 39, it was determined that short-term stability (seconds of firing) could be achieved for injection, mixing, and flow through the ignition region for atmospheric pressure laser-type $H_2$-$F_2$-$O_2$ mixtures.

In order to meet ERDA/DLF established milestones on schedule, it was necessary that these studies be postponed. However, a number of significant accomplishments have thus far been achieved as follows:

1. Active mixture slug separation was achieved for slug injection rates up to 10 slugs/second.

2. Slug mixture uniformity over the ignition region was quantitatively determined and found to be essentially acceptable for laser cavity operation. Thus, the design of the valving system, injection head, and mixing region seems adequate for a repetitively ignited $H_2$-$F_2$-$O_2$ laser system.

3. Slug stability during gas injection at high pressure was achieved for the nondiluted $H_2$-$F_2$-$O_2$ mixtures.

4. Stability of slugs was maintained during passage through the mixing and combustion regions of the flowing systems.

5. Short-term stability for repetitive slug injection and flow through the complete system was achieved for slug injection rates of 2 per second.

6. A tentative proof was obtained that the system does not flash back during operating conditions.

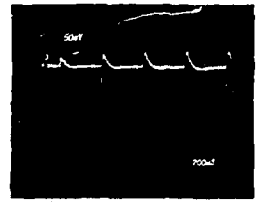


Fig. 39. An oscilloscope trace from a pressure transducer at the ignition region. The trace shows large spikes occurring when laser type mixture slugs were detonated within the charcoal $F_2$ trap. Small excursions occurring 100 ms before each detonation spike corresponds to $H_2$ slug injection at the injection head. The trace timing is 200 ms/division.

## Spontaneous Detonations in Multiatmosphere $H_2$-$F_2$-$O_2$ Mixtures

It is sometimes observed that spontaneous detonations occur in $H_2$-$F_2$-$O_2$ mixtures during loading of these gases into the laser cell or prior to ignition of the laser gas with an electron beam. Work concerning stability of multiatmosphere $H_2$-$F_2$-$O_2$ mixtures has shown that it is possible to achieve stability provided that the mole fraction of oxygen is maintained above a minimum value depending upon the total pressure and the $[F_2]/[H_2]$ ratio involved.[12] Although the mechanisms by which stability takes place in such mixtures have been the subject of a number of studies,[13,14] little effort has been expended in the development of a kinetic model for the existence of third-limit detonations in $H_2$-$F_2$-$O_2$ mixtures.

Effort has been given, during the period covered by this report, to examine possible spontaneous detonation mechanisms which are consistent with experimentally observed phenomena regarding detonations in multiatmosphere $H_2$-$F_2$-$O_2$ mixtures. One of the most salient features concerning spontaneous detonations in such mixtures is that they are initiated at the surface of the containing vessel rather than from the free gas volume.[11,12] The effect of shifting the explosion limits by use or nonuse of the hydrogen surface treatment previously discussed[11] is shown in Fig. 40.

Thus, any kinetic model for the occurrence of detonations in multiatmosphere $H_2$-$F_2$-$O_2$ mixtures must account for surface-initiated processes rather than those only occurring in the gas phase. The only mechanism thus far proposed[15] for the occurrence of third-limit detonations in $H_2$-$F_2$-$O_2$ mixtures has involved volume rather than surface processes and can be explained by the following sequence of reactions in $H_2$-$F_2$-$O_2$ mixtures:

Linear Chain

$$F + H_2 \rightarrow HF^* + H \qquad (3)$$

$$H + F_2 \rightarrow HF^* + F \qquad (4)$$

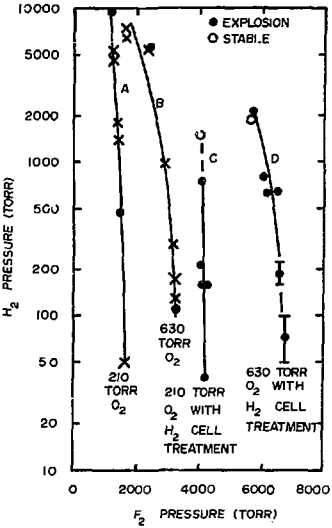


Fig. 40. Observed pressures at which spontaneous detonations occur in $H_2$-$F_2$-$O_2$ mixtures. Explosions occurred at the solid points (or crosses from Ref. 12) as the $H_2$ is added to $F_2$-$O_2$ mixtures placed in the cell prior to $H_2$ introduction. Curves A and B were obtained using $F_2$ passivation prior to each gas filling. Curves C and D were obtained utilizing the explosion cell hydrogen treatment and subsequent $F_2$ passivation prior to each gas filling. The partial pressures of $O_2$ used to obtain each curve are shown in the figure.

Branching

$$HF^* + F_2 \rightarrow HF + 2F \qquad (5)$$

$$HF^{*} + H_2 \rightarrow HF + H_2^{*} \quad (6)$$

$$H_2^{*} + F_2 \rightarrow HF + H + F \quad (7)$$

Termination

$$H + O_2 + M \rightarrow HO_2 + M \quad (8)$$

Regeneration

$$HO_2 + F_2 \rightarrow HF + O_2 + F \quad (9)$$

It has been shown[13, 14] that reactions (3) through (7) are responsible for detonation. Reaction (8), however, acts as a chain terminator to prevent detonation above the second explosion limit. The process $F + O_2 + M \rightarrow FO_2 + M$ has also been considered as a chain terminator. However, it has been pointed out[14, 15] that the reaction $FO_2 + H_2 \rightarrow HF + O_2 + H$ may proceed at such a high rate that $FO_2$ formation may not play an effective role as a chain terminator in $H_2$-$F_2$-$O_2$ mixtures. Under conditions of high fluorine pressure, as in multiatmosphere laser-type $H_2$-$F_2$-$O_2$ mixtures, reaction (9) has been proposed[16] to initiate third-limit detonations through regeneration of F atoms. This type of detonation could occur if the $HO_2$ concentration formed through reaction (8) becomes great enough so that F atom regeneration through reaction (9) equals the H atom loss through reaction (8). Under such conditions, reaction (8) could no longer act as a sink for atoms and the mixture would tend to become explosive. In the present case, however, loss of $HO_2$ by the process[17]

$$HO_2 + HO_2 \rightarrow H_2O_2 + O_2 \quad (10)$$

with a rate coefficient of $k_9 = 1.8 \times 10^{12}$ cm$^3$/mole-second would account for an $HO_2$ loss greater than that through reaction (9) for the case where 6000 torr of $F_2$ is present in the mixture if the $HO_2$ concentration reaches $1.6 \times 10^{-12}$ moles/cm$^3$. The $HO_2$ loss rate through reaction (10) increases as the square of the $HO_2$ concentration, while the loss of $HO_2$ through reaction (9) changes linearly with $HO_2$ concentration. Thus, as the $HO_2$ concentration increases in a pre-explosion reaction sequence, reaction (10) could eventually account for much of the $HO_2$ loss

It is of interest, nevertheless, to examine what the quasi-steady-state H atom concentration would be in a mixture containing say 6000 torr of $F_2$ and 630 torr of $O_2$ under the conditions where F atom regeneration through reaction (9) is equal to the H atoms loss through reaction (8). In such a case:

$$[H][O_2][F_2]k_6 \cong [HO_2][F_2]k_7 \quad (11)$$

and

$$[H] = \frac{[HO_2]k_7}{[O_2]k_6} \leq 0.8 \times 10^{8}[HO_2]. \quad (12)$$

Equation (12) was obtained with an upper limit value for $k_7$ and an accepted value for $k_6$ at 287 K.[14] If the $HO_2$ concentration reaches a value of $1.6 \times 10^{-12}$ moles/cm$^3$, the [H] atom concentration would approach $1.3 \times 10^{-20}$ moles/cm$^3$. At the $HO_2$ concentration where loss of $HO_2$ through reaction (10) exceeds the loss of this radical through reaction (9), there are so few H atoms to enter into chain reactions (3) and (4 that a near linear chain-initiated third-limit detonation involving reaction (9) could not take place. Thus, a conclusion is reached that the proposed volume initiated third-limit detonation mechanism could not occur in mixtures containing up to 6000 torr of $F_2$ and 630 torr of $O_2$ at room temperature.

As $H_2O_2$ forms in the mixture through reaction (10), there will be a tendency for water vapor to eventually form in the explosion cell through decomposition of $H_2O_2$. Decomposition of $H_2O_2$ can occur at the wall of the explosion chamber such that

Wall

$$H_2O_2 \rightleftharpoons 2\,OH \quad (13)$$

takes place readily at room temperature.[18,19] With at least 100 torr of $H_2$ in the $H_2$-$F_2$-$O_2$ mixture, the process[20]

$$H_2 + OH \rightarrow H_2O + H \qquad (14)$$

is the dominant loss process for removal of OH from the system until the OH concentration becomes unreasonably large (i.e., $> 10^{-8}$ moles/cm$^3$). The formation of water, essentially at the surface of the explosion cell supplies the igniting mechanism in $H_2$-$F_2$-$O_2$ mixture since it has been shown that water vapor will ignite in a fluorine atmosphere at a metal surface such as nickel wire.[21] Thus, the proposed model for detonations in $H_2$-$F_2$-$O_2$ mixtures is consistent with the experimental observation that spontaneous detonation in $H_2$-$F_2$-$O_2$ mixtures initiates at the surface of the explosion cell rather than primarily from the gas volume. This model is supported by the experimentally observed fact that pre-exposure of the explosion cell to small amounts of water vapor prior to filling the cell with $H_2$-$F_2$-$O_2$ mixtures drastically reduces the stability of such mixtures.[22]

## High-Pressure $H_2$-$F_2$ Laser Studies

The HF laser, operating on the $H_2$-$F_2$ chain reaction, is an attractive system due to its relatively high overall efficiency. The available output energy is, however, distributed over a large number of vibrational-rotational lines of the HF molecule. For an efficient oscillator-amplifier chain, one therefore requires a similar spectrum throughout all early stages. This situation has been discussed in a previous section, with current development emphasizing electric discharges in $SF_6$-HI gas mixtures to obtain a high-quality beam with reasonable spectral match. A second possibility for the oscillator is, clearly, an electron-beam initiated mixture of $H_2$ and $F_2$. With sufficiently short initiation times (few ns) one could then expect to achieve laser pulses of comparable duration by increasing the gas pressure. Provided the fractional initial dissociation ($F/F_2$) does not decrease with overall pressure, the burn rate and subsequent laser pulse would then decrease with increasing pressure. Moreover, with initiation levels similar to those anticipated for the final amplifier, one may expect to achieve a reasonably similar spectral match.

The experiments described here were originated to examine the pressure-dependent HF laser pulsewidths for pressures up to 10 atmospheres of $F_2/H_2/O_2$ at approximate relative concentrations of 1:0.25:0.3. Oxygen is present in these mixtures in order to prevent premature detonation of the mixture. The electron-beam pulse, originating from a Febetron 706, was 2.5 ns (FWHM) in duration, with electron energies of either 440 keV or 625 keV. The test cell was designed to withstand pressure excursions up to 3000 psia. From energy deposition measurements, the initial $F/F_2$ ratio was expected to be about 0.1 percent or more. Subsequent experiments must then examine the feasibility of obtaining a high-quality laser beam from this oscillator. The results described here are preliminary in nature; further work has been postponed in order to accelerate progress on the electric discharge system.

The high-pressure cell used here was equipped with sapphire windows mounted transverse to the electron beam axis. After each shot, the overpressure was allowed to expand into a pressure-relief tank through a thin Mylar rupture disc. The gain length, determined from electron-beam profile determinations, was approximately 1 cm. A cavity was formed with a 98-percent reflectance 2-metre-radius-of-curvature mirror and various output couplers. Most of the measurements were performed with a 60-percent-reflecting ZnSe flat. Others used were an uncoated ZnSe flat (~17-percent reflectance) and a coated Germanium flat (80-percent reflectance). Laser pulses were monitored with an Au:Ge (77 K) detector (response time 2 ns). Energy measurements were made with a 2.5-cm-diameter Scientech calorimeter.

Briefly, the portion of this work which has appeared in earlier reports showed that laser action did not occur for these conditions without feedback,[11] i.e., the single pass gain (1-cm gain length) was not enough to overcome the window losses. This is a unique situation for electron-beam-initiated $H_2$-$F_2$ mixtures and resulted in increased sensitivity to otherwise small kinetic losses. It was shown that the laser pulse consisted of two distinct peaks, with the second peak probably originating from higher HF vibrational levels ($v \geq 3$). The amplitude of this peak (which contained most of the total energy) decreased strongly with increasing fractional pressure of oxygen. The earlier studies showed that the laser pulsewidth decreased with increasing total pressure (with standard $F_2$-$H_2$-$O_2$ mixtures) up to 1200 torr $F_2$. The present work has extended the range of pressures studied up to 2400 torr $F_2$ and 600 torr $H_2$ with a wide range of $O_2$ concentration. The output energy dependence on $O_2$ concentration has been studied in greater detail, and the possible effects of parasitic oscillations has been investigated. For one case, the output pulse shape has been compared with Sandia's HF laser code.

The $O_2$ dependence of the laser output is summarized in Fig. 41 for 1200 torr $F_2$, 800 torr $F_2$, and 400 torr $F_2$ at a fixed $H_2$ fraction of 0.25. The results are shown as a function of total $O_2$ pressure. The results indicate that, for these conditions, the standard 30 percent $O_2/F_2$ ratio would result in practically no output at 1200 torr $F_2$. The portion of the laser pulse which had earlier been attributed to the higher vibrational levels of HF [and, therefore, due to the "hot" reaction: $H + F_2 \rightarrow HF(v \leq 6) + F$] was the only part of the pulse which was degraded with increasing $O_2$, over the range indicated in Fig. 41. Less than 10 percent of the output was contained in the remainder of the laser pulse.

With this in mind, Fig. 41 suggests that $O_2$, or one of its products formed in the mixture, contributes strongly towards quenching the

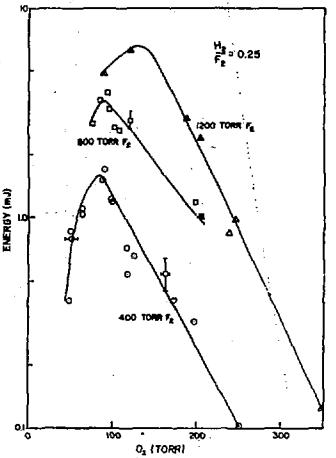


Fig. 41. The variation of laser output energy with $O_2$ pressure for three $F_2$ pressures. The $H_2/F_2$ ratio was fixed at 0.25. The gain length was 1 cm, with an initial $F/F_2$ ratio of approximately 0.1 percent.

"hot" reaction. Typical rate constants for the competing reaction $H + O_2 + M \rightarrow HO_2 + M$ are of the order of $10^{-32}$ $cm^6$ $s^{-1}$ $molec^{-2}$ or less, which predicts reaction times of several hundred ns—somewhat longer than the observed laser pulse. Nevertheless, this mechanism generally accounts for the observed behavior, and more extensive measurements are required to clarify this point. The decrease in output seen in Fig. 41 at low $O_2$ pressures is possibly due to increased preignition buildup of HF—a process which is inhibited in the

presence of $O_2$. For regions of the curves where decreased output was observed, increasing the cavity feedback (from 60 percent to 80 percent) resulted in a considerable increase in output energy and pulsewidth. This result is consistent with predicted effects of the H-atom scavenging reaction mentioned earlier. At the highest pressures studied here (2400 torr $F_2$, 600 torr $H_2$, 400 torr $O_2$), the laser pulsewidth varied from about 10 ns with 60 percent feedback to 50 ns with 80 percent feedback. In order for the results to be meaningful to the overall program of oscillator development, similar experiments must necessarily include a determination of laser spectral content as a function of pressure and mixture composition.

The Sandia HF laser code results were compared with the data at 800 torr $F_2(F_2/H_2/O_2 = 1/0.25/0.30)$, and the overall pulse shape was in reasonable agreement, although the energy was overpredicted by nearly a factor of 10[2]. In order to determine if part of the discrepancy was due to parasitic oscillations within the cell, several computer runs were made based upon a simplified parasitics model developed by J. B. Moreno. This model predicted that the presence of parasitics would be indicated by sensitivity of the results on cavity length and wall reflectivity. Several experiments were run, varying the cavity length and the internal cell reflectivity.

The latter was achieved by placing various liners, including Teflon and wire mesh within the cell. The results were generally independent of any of these variations. The HF laser code has recently been modified by J. B. Moreno to include the various effects of $O_2$ chemistry and will be useful in future experiments of the type described here.

In summary, the development of a small-volume high-pressure $H_2$-$F_2$, electron-beam-initiated oscillator which requires a short pulse at high pressures with a spectral match to larger scale amplifiers will require a more detailed understanding of the $O_2$ chemistry on the mixture. The results shown here, although preliminary, indicate that the HF inversion density for $v \geq 3$ is seriously affected by the presence of $O_2$ for systems of comparable scale to that described here.

## Time Sequenced Energy Extraction on the High-Gain Xenon Laser

It has been proposed that the technique of angular multiplexing could provide an efficient scheme for extracting short pulses from a high-gain laser with spatial and temporal control of the extracted laser beam. The angular multiplexing[23] scheme produces a short laser pulse ($\sim$ 1 ns) by sequentially passing several short pulses through the amplifier at slightly different angles, and each of the amplified laser pulses are then combined into a single short laser pulse by appropriate optical delay lines. The intensity of each pulse must be sufficient to control the forward and backward amplified spontaneous emission (ASE). The purpose of this study was to experimentally examine the technique of angular multiplexing. The prototype system chosen for study was the high-gain infrared xenon laser. The xenon laser was chosen because: (1) it is a high-gain system (measured small-signal gain coefficient[24] is $g_o = 2.5\ cm^{-1}$), (2) it operates at wavelengths[11] in the same range as other more complex high-gain lasers such as HF (this is important if comparisons and scaling to other high-gain systems are to be made), and (3) of the available high-gain lasers, the xenon laser system is probably the least complex with regard to construction and operation.

The initial phase of this program was to characterize well the xenon-laser system that was fabricated for this study: namely, determine the small-signal gain, saturation intensity, and spontaneous emission parameters for this laser. The performance of a master-oscillator power-amplifier (MOPA) combination was also measured in order to

determine what fraction of the available energy could be extracted and what effect, if any, transverse reflectivity had on transverse ASE and the extracted energy. These results were reported in Ref. 11.

The second part of the study was concerned with sequentially passing two xenon-laser pulses through a power-amplifier at slightly different angles. The questions addressed in the second part were: (1) what fraction of the available energy in the amplifier could be extracted by both pulses, (2) how does pulse distortion and energy extraction vary with pulse separation and pulse delay, and (3) how does the forward ASE flux vary with pulse separation and initial pulse delay. Input pulsewidths and pulse intensities were kept constant for the second part of the study.

The experimental arrangement is shown in Fig. 42. It consisted of two oscillators each pulsed sequentially in time with variable pulse separation of 0.1, 0.5, 1.0, 1.5, and 2.0 $\mu$s. The oscillators, described in Ref. 24, were identical and each consisted of an 8 mm-I.D. quartz tube with two hollow aluminum electrodes separated by 25 cm. Each oscillator produced approximately 0.1 mJ in a 1.5-$\mu$s (FWHM) pulse. Each pulse was passed through the power-amplifier at an angle of approximately 10 mrad with respect to the amplifier axis and was expanded to fill a 4-cm$^2$ area of the amplifier cross section. Each pulse filled about 82 percent of the active discharge volume of the amplifier. The first oscillator pulse was initiated at various predetermined delay times with respect to the electrical initiation of the amplifier.

The laser amplifier consisted of a 30-cm-long quartz tube with Infrasil Brewster-angle windows at each end. As described in Ref. 11, an absorbing material lined the walls of the amplifier to minimize the formation of parasitic oscillations. For the same reason, the aluminum electrodes of the amplifier were sandblasted. The gain period of the amplifier, obtained from the time dependence of the ASE, was approximately 4.5 $\mu$s long with an FWHM of 1.3 $\mu$s. The results of previous experiments[24] have shown that the small-signal-gain coefficient and saturation intensity of the xenon gain medium was $g_o$ = 2.5 cm$^{-1}$ and $I_s$ = 0.2 W/cm$^2$. The output spectrum of the MOPA system contained lines at 2.027, 2.65, 3.508, and 3.65 $\mu$m.

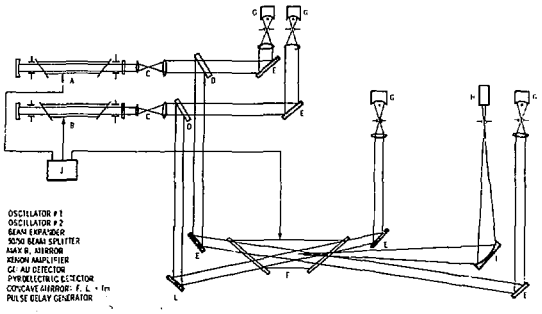


Fig. 42. Diagram of experimental arrangement used for studying time sequenced energy extration on the high-gain xenon laser.

The intensity of input and output pulses to the amplifier were monitored using Au:Ge infrared detectors cooled to 77 K. In addition, the intensity of the forward ASE was also measured.

In Fig. 43 the forward ASE of the amplifier as a function of time delay is shown. The amplifier pump is turned on at $t = 0$. The time delay was measured from the leading edge of the leading oscillator pulse to $t = 0$. At a time delay of $\geq 0.05\ \mu s$ for the leading input pulse, the ASE intensity is at a maximum value of 5.5 W/cm$^2$. By reducing the time delay to approximately $-0.3\ \mu s$, the peak of the leading pulse is coincident with the peak of the amplifier gain pulse. At $-0.3\ \mu s$, the ASE intensity has decreased to less than 1 W/cm$^2$. Decreasing the time delay less than $-0.3\ \mu s$ resulted in a gradual increase in the ASE intensity (at $-0.5\ \mu s$, the forward ASE intensity was 1.8 W/cm$^2$).

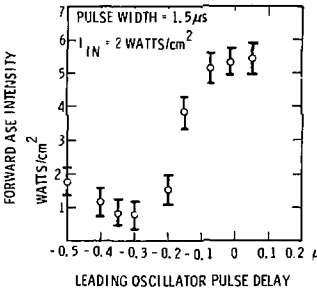


Fig. 43. Forward ASE intensity for various time delays of initial pulse.

Figure 44 shows the extracted intensity (i.e., $I_{out} - I_{in}$) as a function of time delay for the leading input pulse. A fixed pulse separation of 1.0 $\mu s$, a fixed oscillator pulsewidth of 1.5 $\mu s$ (FWHM), and a fixed input pulse intensity of 2 W/cm$^2$ were used in this case. Figure 44 indicated an optimum leading pulse delay of approximately $-0.3\ \mu s$ for these experiments. The leading pulse extracts about 60 percent of the measured maximum extractable power because it overlaps the maximum inversion time of the amplifier. The maximum extractable power was measured to be 12 W/cm$^2$ in Ref. 24. These measurements were taken for input intensity levels, $I_i$, approximately 10 times the saturation intensity level ($I_i/I_s = 10$).

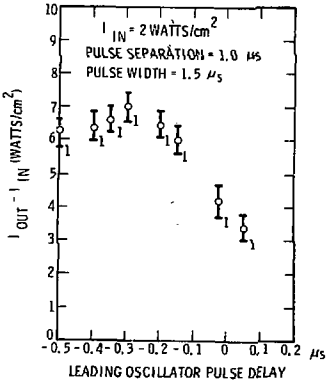


Fig. 44. Extracted intensity as a function of time delay for leading input pulse.

Figure 45 shows extracted intensity ($I_{out} - I_{in}$) for the leading and trailing pulses as a function of pulse separation. A fixed leading-pulse delay of $-0.3\ \mu s$ and

an input intensity of 2 W/cm$^2$ for each input pulse was used in this measurement. Figure 45 shows that, with small pulse separations (nearly overlapping input pulses), both pulses extracted the same amount of energy. As the separation is increased, the trailing pulse extracts less energy because at later times there is less available energy in the amplifier. From Fig. 45, the optimum pulse separation for maximum extraction is seen to be between 1.0 and 1.5 $\mu$s. At pulse separations larger than 2.0 $\mu$s, the total extracted intensity by both pulses (sum of both output pulse intensities) falls to less than 42 percent of the maximum extractable power. This is compared with 93 percent for the total extracted intensity at 1.0-$\mu$s pulse separation.

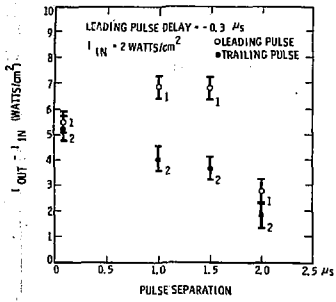


Fig. 45. Extracted intensity for initial and secondary pulses for various pulse separation times.

At pulse separation less than or greater than the range 1.0 to 1.5 $\mu$s, ASE becomes the predominate competitor for available power. This is verified by Fig. 46 which shows the forward ASE as a function of pulse separation for a fixed time delay of -0.3 $\mu$s and a fixed input pulse intensity of 2/W cm$^2$. Forward ASE was reduced to less than 0.5 W/cm$^2$ for pulse separations of 1.0 to 1.5 $\mu$s. The uncertainty in measured ASE intensity and extracted intensity in these experiments was ±10 percent. The increase in the forward ASE increases both for separations less than 1.0 $\mu$s and separations greater than 1.5 $\mu$s because, under these conditions, the input pulses do not cover in time the entire gain-period of the amplifier. Intensity in these experiments was interpreted to mean average intensity, calculated from the measured energy, laser pulsewidth, and the active cross-sectional area.

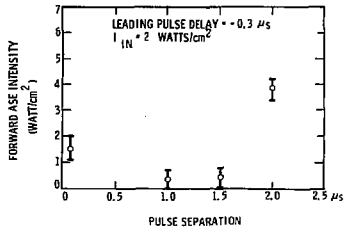


Fig. 46. Forward ASE intensity as a function of pulse separation for a fixed time delay of -0.3 $\mu$s.

In Fig. 47 we show the temporal shape of both output pulses for various input pulse separations. The input flux for each pulse was 2.0 W/cm$^2$. The time delay was fixed at -0.3 $\mu$s. The input pulsewidth shown by the dashed lines in Fig. 47 (b, c, d, e) were each 1.5 $\mu$s (FWHM). Curve (a) of Fig. 47 shows the time dependence of the amplified spontaneous emission from the amplifier with no input. This represents the gain-period of the amplifier. Curve (b) shows the leading and trailing pulse outputs when the separation of the two oscillators was 0.1 $\mu$s. As expected, the outputs are nearly identical.

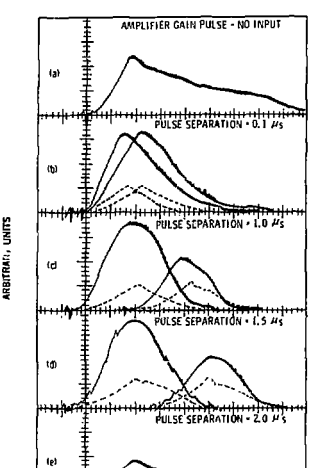


Fig. 47. Temporal shape of amplified pulses for various input pulse separations. Curve (a) shows the time dependence of the amplifier gain pulse. The dashed curves in (b), (c), (d), and (e) are the time histories of the input oscillator pulses.

For the cases of optimum pulse separation (c and d in Fig. 47), the technique of amplifier-multiplexing has been demonstrated. These data show that individual pulses shorter than the amplifier gain pulse can be produced from a high-gain amplifier. The time at which the leading and trailing intensities are equal corresponds to the time at which the intensities of the two input oscillator pulses are equal. Under these conditions, more than 90 percent of the available energy was extracted from the amplifier and the ASE was reduced by a factor of 10 over that measured when no input flux was present in the amplifier. As shown in Fig. 47 (c, d) there is very little temporal distortion in either pulse; the trailing pulse showed no distortion while the leading pulse was broadened from 1.5 to 1.7 μs (FWHM). This distortion is caused by the temporal variation of the gain in the amplifier. As the number of input pulses are increased (shorter input pulsewidths) the distortion in the pulses should be reduced.

Figure 47 (e) shows the effect of separating the pulses such that the amplifier gain period is not entirely covered by the input oscillator pulses. Both pulses are temporally distorted, and no gain was measured for the trailing pulse. The leasing pulse is much longer than (c) and (d) because of the increased ASE at this separation.

Measurements indicate that optimum pulse separation as well as pulse delay time exist for the xenon laser. For this optimum pulse separation and pulse time, the temporal shape of the amplified pulses was relatively undistorted. Also, at this optimum pulse separation and pulse delay time, the power extraction efficiency was maximum and measured forward ASE was minimum. Power extraction efficiency and forward ASE were found to be a sensitive function of pulse separation and pulse delay times. The measured optimum pulse delay and pulse separation times were ~0.3 μs and 1.25 ± 0.25 μs, respectively, for the xenon laser. These measurements were made for fixed input beam intensities and fixed pumping level of the gain medium.

The next phase of this experiment was to produce shorter oscillator pulses such that a clearer demonstration of pulse shortening by angular multiplexing could be demonstrated. Unfortunately, it was necessary to terminate this program in order to meet our HF program milestones. However, the results demonstrate the concept, and they

permit us to proceed with confidence that the technique can be used on large HF laser systems to shorten the pulse width and to suppress laser prepulse on target.

## IODINE LASER PROGRAM

### Overview

Experimental studies during this report period emphasized evaluation of beam quality in saturated and unsaturated amplifiers, pulse distortion, efficiency and code development. The codes are now in good shape, and little further development is needed in order to confidently design more complex systems. Chemical kinetic modeling has been used to predict starting material consumption in an iodine laser, and a study of chemical regeneration has been initiated.

### SAIL-1 Output Beam Quality

The transmission of the oscillator output beam through apertures of various radii was measured at three different distances z from the oscillator mode-selecting aperture. The results are shown in Fig. 48. The solid curves correspond to the expected transmission for a Gaussian beam with a full-width divergence (1/e intensity points) of 455 $\mu$rad. The agreement with the data is extremely good. Agreement is also very good with previously taken lateral shearing interferograms of the oscillator output beam.[25] In the latter case the beam diameter at z = 26.4 m was originally estimated to be 9 mm from photographs of the beam profile. However, from Fig. 48, the intensity diameter at z = 26.4 m is 12 nm. The divergence inferred from the lateral shearing interferograms then agrees exactly with the divergence obtained from Fig. 48.

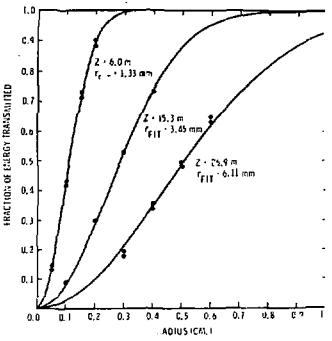


Fig. 48. The transmission of the SAIL-1 atomic iodine oscillator beam through various diameter apertures at three distances z.

Photographs of the preamplifier output beam were taken using the EPL streak camera as an image converter. Similar photographs were previously taken of the oscillator output beam.[26] Figure 49 (a) is a photograph of the preamplifier output beam taken at a distance of 26.4 m from the oscillator mode-selecting aperture. The preamplifier was unsaturated and the gain was ~ 100. Figure 49 (b) and 49 (c) are a "shade-of-gray" plot, and a contour map was constructed from a densitometer scan of Fig. 49 (a). It can be noted that the preamplifier output beam diameter is slightly smaller than the oscillator output beam diameter at the same distance z.[26] This is consistent with previously taken lateral shearing interferograms of the preamplifier output beam,[25] and is caused by gas

dynamic motion of the preamplifier gain medium resulting from nonuniform pumping.

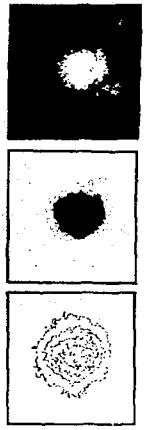


(a) Photograph of beam profile taken with EPL streak camera used as an image converter.

(b) "Shade-of-gray plot" made from densitometer scan of (a) above.

(c) Contour map made from densitometer scan of (a) above.

Fig. 49. The beam profile of the iodine preamplifier output at a distance of 26.4 m.

Lateral shearing interferograms were also taken for the 75-mm-diameter amplifier output beam, both in the unsaturated and saturated case. The system was modified slightly prior to taking the interferograms. Longer flashlamps were installed in the 75-mm-diameter amplifier, and the active gain medium length was increased from 312 to 353 cm. Also, an optical gate consisting of crossed polarizers and a Pockels cell was installed between the preamplifier and the 75-mm amplifier. The optical gate introduced a small amount of phase distortion to the beam wavefront, but it was considered small enough to neglect. In order to avoid phase distortion introduced by the preamplifier,[25] the oscillator pulse was injected into the preamplifier 2 $\mu$s earlier than was normally the case. This advance was determined by taking lateral shearing interferograms of the preamplifier output as a function of delay from initiation of the preamplifier flashlamps to insertion of the oscillator pulse. This eliminated the phase distortion from the preamplifier, and the preamplifier gain was still $\sim$ 40. Figure 50 (a) shows a lateral shearing interferogram for the 75-mm amplifier with a gas mixture of 10 torr $C_3F_7I$ plus 750 torr argon. The gain is $\sim$ 700, and the amplifier is unsaturated. The resultant fringe pattern is consistent with an interferogram of the oscillator itself.[25] The radius of curvature is the same as for the oscillator, and little phase distortion is present. Figure 50 (b) shows an interferogram for the 75-mm amplifier when the amplifier has been saturated. The gain has been reduced to 80. The input energy is 6 mJ, and the beam has not been expanded before insertion into the 75-mm amplifier.

A number of observations are worth noting from Fig. 50 (b). First, the beam diameter has grown, because the net gain in the wings is higher than it is on-axis. Second, the fringes have the same tilt angle as in Fig. 50 (a) on the outer edges of the beam, but the tilt angle is smaller in the center of the beam, where most of the saturation occurs. The radius of curvature is 23 percent larger on-axis than at the edges, i.e., that part of the beam has experienced a slight positive lensing (whole-beam self-focusing). Preliminary calculations using a one-dimensional propagation code[27] predict for the same conditions a similar phase retardation on-axis as that inferred from Fig. 50 (b). The effects of phase

retardation due to gain saturation on the ultimate focusability of the output beam are being investigated.

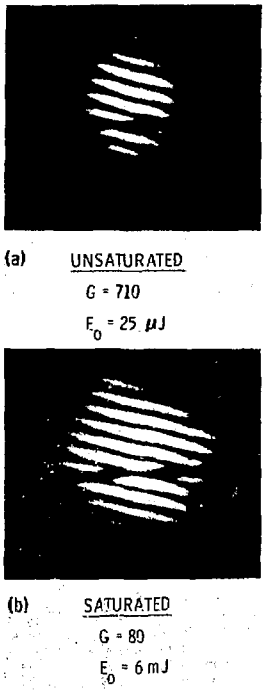


Fig. 50. Lateral shearing interferograms of SAIL-1 75-mm amplifier output beams for a nonsaturating and a saturating input pulse.

Temporal Broadening of an Unsaturated Amplified Pulse Due to Insufficient Amplifier Bandwidth

It is important that the amplification of a laser pulse does not modify the temporal pulseshape, because in general the pulseshape influences the target interactions. The bandwidth of the iodine laser is typically 10 to 20 GHz for buffer gas pressures of a few thousand torr, and the question arises as to the effect of this bandwidth or smaller bandwidths on the temporal pulseshape of amplified subnanosecond pulses. To this end, we have measured the broadening of pulses in the unsaturated preamplifier under various conditions using the EPL streak camera. Figure 51 is an example of the broadening that can occur. The preamplifier buffer gas pressure was 500 torr, which corresponds to a bandwidth of ~3 GHz. Appreciable broadening of the output pulse is evident. There is a split filter across the camera slit for calibration purposes, so that the top half of the exposure is brighter than the bottom half.

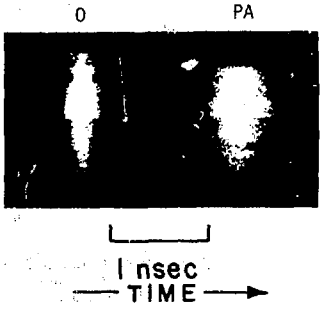


Fig. 51. Temporal pulse broadening of SAIL-1 oscillator output (O) by low pressure (low bandwidth) preamplifier (PA)

The parameter used to characterize the broadening was $\tau_o^2 - \tau_i^2$, where $\tau_o$ and $\tau_i$ are the pulsewidth (FWHM) of the output and input pulse, respectively. This parameter was chosen because two simple analytic theories suggested that this parameter should be independent of the pulsewidth itself.[28,29] This occurs because shorter pulsewidths produce more broadening, and the two effects tend to cancel each other. The quantity $\tau_o^2 - \tau_i^2$ was calculated as a function of $\ln g^{SS}$ using a 1-dimensional beam propagation code.[27] The results are shown in Fig. 52 for three different bandwidths (argon buffer gas pressures of 350, 500, and 1000 torr). Two temporal pulseshapes were used in the calculations: $\exp(-4 \ln 2\, t^2/\tau^2)$ and $\exp(-16 \ln 2\, t^4/\tau^4)$; the calculated temporal broadening for these two pulseshapes is given in Fig. 52 by the solid curve and the dashed curve, respectively. Agreement with the data, which are also plotted in Fig. 52, is poor.

The poor agreement may be explained by the following argument. Because the two simple analytic theories[28,29] indicated that the broadening should be independent of the pulse width, the oscillator cavity length was not carefully tuned to the active mode-locker frequency. This resulted in a range of pulse widths as expected, but it also resulted in a range of pulse shapes as well. Examples of the different pulse shapes are shown in Fig. 53. The "good" pulse is characteristic of a well-aligned oscillator; the small perturbations are noise from the streak camera. The "fair" pulse has a distinct shoulder, and the "poor" pulse has the top clipped off. These two latter pulses would result in an incorrect inference of the

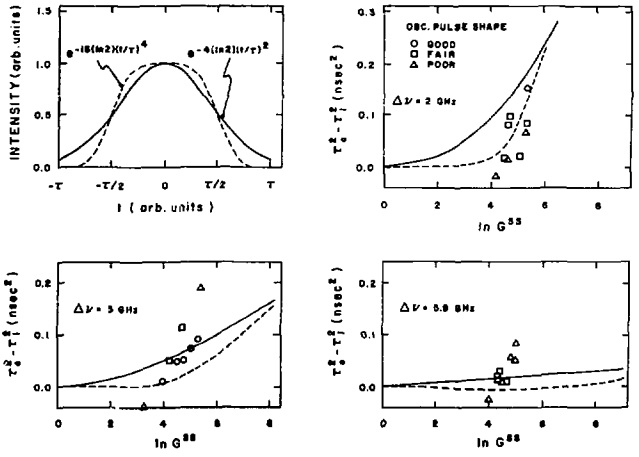


Fig. 52. Effect of pulseshape on temporal broadening and comparison to experiment for an unsaturated atomic iodine amplifier at various bandwidths.

pulse width (FWHM), because the data are being compared to a smooth temporal pulse shape.

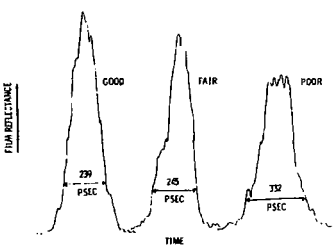


Fig. 53. Examples of three classes of streak camera photographs of atomic iodine oscillator pulses.

It can be seen in Fig. 52 that the "good" pulses agree best with the theoretical broadening for the Gaussian pulses (solid line), which is the expected pulse shape for an actively mode-locked oscillator.[30] The "poor" pulses have the worst agreement. In retrospect, this experiment should be repeated using only "good" pulses, with the oscillator cavity length well tuned to the active mode-locker frequency. However, it is encouraging that the initial broadening data agree qualitatively with the 1-dimensional code calculations. Also, it is important to point out that when the pre-amplifier is operated with a sufficient bandwidth, no pulse distortion is observed.

## Overall Efficiency of the SAIL-1 75-mm Amplifier

An attempt was made to optimize the overall efficiency of the SAIL-1 75-mm amplifier by varying both the capacitor bank energy and the $C_3F_7I$ fill pressure. Both of these parameters had a small effect on the overall efficiency.

The total energy stored on the amplifier capacitor bank ($E_{cap}$) can be varied from 30 to 50 kJ. The logarithm of the small signal gain ($\ell n\, G^{SS}$) is proportional to the energy stored in the gain medium. A plot of $\ell n\, G^{SS}/E_{cap}$ vs. $E_{cap}$ is shown in Fig. 54. As $E_{cap}$ was varied from 30 to 50 kJ, the overall efficiency was virtually unchanged (note the expanded vertical scale). This suggests either that the effective blackbody temperature of the flashlamps did not change appreciably with a 30% increase in peak current,[31] or that the contribution to the total light emission in the laser pumpband by blackbody radiation from the lamp plasma is small. The results of Ref. 31 would yield an 11% higher temperature for a 30% increase in current. It is to be noted that there is a significant contribution to the near ultraviolet radiation by line radiation from silicon ablated from the flashlamp inner wall, and its role in the lamp behavior has yet to be ascertained.

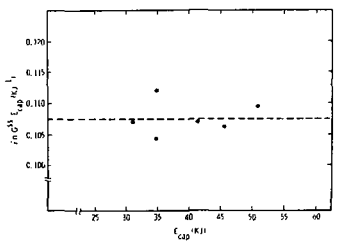


Fig. 54. Logarithm of small signal gain $\ell n\, G^{SS}$ divided by capacitor bank energy $E_{cap}$ vs. $E_{cap}$.

If not all of the flashlamp emission in the laser pumpband is absorbed by the gain medium, the overall efficiency will be reduced. To investigate this effect, the SAIL-1 75-mm amplifier was run as an oscillator. A cavity was formed by placing a 100% reflector at one end and a 30% reflector at the

other end. The total laser energy was measured as a function of $C_3F_7I$ pressure. The laser energy for a free-running iodine oscillator is equal to 2/3 of the stored energy above threshold. The ratio of argon buffer gas pressure to $C_3F_7I$ pressure was held fixed at 50:1. The threshold inversion varied as the $C_3F_7I$ pressure was varied, but since the amplifier was pumped strongly, the threshold inversion was negligible compared to the laser energy. Thus, the laser energy was proportional to the stored energy.

The laser energy vs. $C_3F_7I$ pressure is shown in Fig. 55. For low $C_3F_7I$ pressures, the laser energy increases rapidly. As the medium becomes optically dense at higher pressures, the laser energy levels off, since all of the available flashlamp pump light is absorbed. The tailoff at still higher $C_3F_7I$ pressures is due to losses at the tube circumference, where the lasing is now occurring. At $C_3F_7I$ pressures > 15 torr, the radial gain profile is nonuniform.[32] At 10 torr, the radial gain profile is quite uniform and the stored energy is only 16% down from the peak stored energy. The latter does not seem to be an unacceptable loss in order to achieve a uniform radial gain profile. However, if a nonuniform radial gain profile does not result in excessive degradation of focusability (which is yet to be determined), a 15 torr $C_3F_7I$ fill pressure is optimal for this amplifier.

The peak overall efficiency from Fig. 49 is 0.22%. Similar experiments performed at Max-Planck-Institut für Plasmaphysik and at the University of Manchester have yielded peak overall efficiencies of ~1%. One significant difference between the present experiment and these two other experiments is that our flashlamps have a peak current of ~25 kA, whereas the peak flashlamp current in the other two experiments is ~50 kA. The most efficient[35] blackbody temperature is approximately 19,500 K for radiation in the iodine pumpband. For a flashlamp bore of 1.5 cm (all three facilities have similar bore flashlamps), the current which produces this temperature is ~29 kA. The fact that significantly higher currents yield much higher efficiencies may suggest that the plasma opacity is not high enough in the iodine pumpband to permit blackbody-like radiation. Reference 36 addresses this question, and experimental evidence gathered in this laboratory is consistent with the increase in plasma opacity with increasing discharge current.

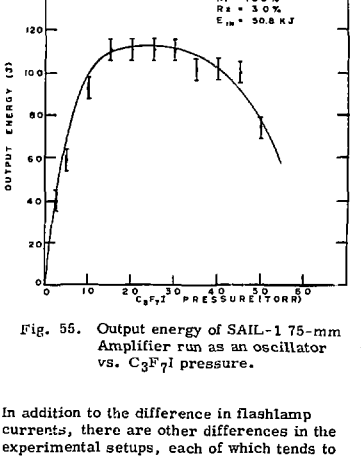


Fig. 55. Output energy of SAIL-1 75-mm Amplifier run as an oscillator vs. $C_3F_7I$ pressure.

In addition to the difference in flashlamp currents, there are other differences in the experimental setups, each of which tends to lower the overall efficiency of the SAIL-1 75-mm amplifier. These factors include: germasil filters surrounding the flashlamps, use of sealed rather than recharged lamps (with new gas), nonoptimal flashlamp reflector geometry, and frosting of the laser tube. The design of a practical laser system must include the consideration of each of these factors as it affects total system performance.

## Comparison of 1- and 2-Dimensional Beam Propagation Code Results With Experimentally Determined Line Broadening and Gain Saturation Parameters

One of our primary goals has been to develop reliable 1- and 2-dimensional beam propagation codes to model the iodine laser system. Reliable codes are necessary to scale the iodine laser to systems with the energies and powers appropriate to laser fusion. Two important parameters used in the codes are line broadening coefficient B and the saturation flux $F_s$. The latter parameter is related to the stimulated emission cross section $\sigma$.

The atomic iodine transition is split into six hyperfine transitions.[37] The strongest is the F = 3 → F = 4 transition, which is the transition on which the SAIL-1 oscillator lases. As the argon buffer gas pressure is increased, these six transitions begin to overlap, and the gain at the F = 3 → F = 4 wavelength reflects this overlap. A measurement of the gain at the F = 3 → F = 4 wavelength as a function of argon pressure can then in principal determine the broadening coefficient B.

Figure 56 shows the product $P_{Ar}$ *ln* $G^{SS}$ as a function of argon pressure for the SAIL-1 preamplifier. The rise in this product with increasing pressure is due to both the overlap of the hyperfine lines and the increase in preamplifier bandwidth. At low argon pressures, there is insufficient bandwidth to amplify efficiently the 225-ps (FWHM) pulses from the oscillator. The solid curves are fit to the data (obtained by varying the inversion density) using a 1-dimensional beam propagation code,[27] assuming B = 3, 6, and 9 MHz/torr for the broadening coefficient for argon. The shape of the curve is relatively insensitive to B; however, B = 5 to 6 MHz/torr results in the best fit. Numerous previous determinations of B by several laboratories,[37-40] including Sandia, also range between 5 and 6 MHz/torr. Thus, the 1-dimensional code quite accurately reproduces the change in $G^{SS}$ due to bandwidth effects and line overlap.

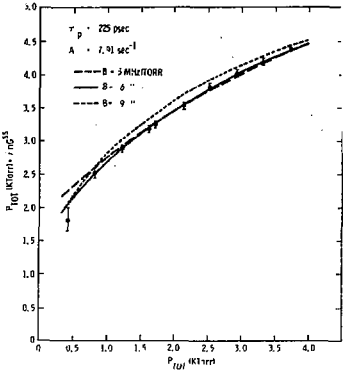


Fig. 56. Variation of *ln* $G^{SS}$ times total pressure vs total pressure in an atomic iodine laser amplifier.

*One other point can be inferred from Fig. 33.* In order to extract an appreciable amount of energy from the F = 2 upper state, the argon buffer gas pressure should be at least 3 to 4 ktorr. If it is necessary to operate at pressures lower than this, in order to reduce the saturation flux, a two-line oscillator may be desirable if optimum extraction efficiency is required.[41]

Another test of the ability of the codes to reproduce experimental data is the prediction of gain saturation. Figure 34 shows the saturation of the gain of the SAIL-1 75-mm amplifier. The experimental conditions for the data shown are $P_{Ar}$ = 750 torr, $P_{C_2F_7I}$ = 10 torr, and $E_{cap}$ = 50.8 kJ. In order to obtain maximum saturation, the input beam has not been beam-expanded. Since the input beam must traverse several metres through the amplifier, an increase of the beam diameter will occur due to the natural divergence of the beam. For this reason, the

2-dimensional beam propagation code was used. Three different predictions of the code are shown in Fig. 57: B = 5 MHz/torr with lower level relaxation, B = 5 MHz/torr with no lower level relaxation, and B = 3 MHz/torr with lower level relaxation. For all three cases, the total A-coefficient was assumed to be 7.91 second$^{-1}$.

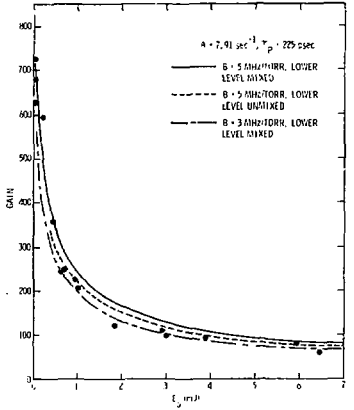


Fig. 57. Gain vs. input energy $E_0$ for SAIL-1 75-mm atomic iodine laser amplifier.

All three calculations fit the data well; however, the calculation with B = 5 MHz/torr and lower level relaxation (which we believe to be realistic) does not saturate quite as rapidly as the data indicate. The lower level relaxation rate has not been well determined, and there is great discrepancy between different literature values.[42, 43] However, if the broadening is controlled by lower level relaxation, as is currently believed,[42] then the relaxation rate should be rapid enough to relax the lower levels under the experimental conditions of the data shown in Fig. 57. One other possibility is that the code in its present form does not include all the sources of the self-focusing that we have observed for gain saturated pulses. The contributions to self-focusing from the nonlinear refractive indices $n_2$ of argon and $C_3F_7I$ are not included in the code and are now being investigated more fully. The fact that focusing is observed in the shear plate interferometry measurements indicates that the nonresonant part of the refractive index due to the different polarizabilities of the J = 1/2 and J = 3/2 manifolds is not dominant. This effect would cause defocusing. More experiments may be necessary, however, in order to resolve the slight discrepancy between the gain saturation data and the predictions of the 2-dimensional code using what we consider to be the proper input parameters.

## Two-Dimensional, Time-Dependent, Multilevel Maxwell-Bloch Code for Iodine Amplifiers

In a previous report,[27] a one-dimensional, time-dependent Maxwell-Bloch code (ISIX) was described for calculating the evolution of the electric field as it is amplified in the six-level iodine system. The necessity of using small-radius beams rather than expanded beams forced the development of an accurate two-dimensional version of the amplifier code because of significant diffractive beam spread inside the amplifiers.

The Maxwell-Bloch equations to be solved are

$$\left(\frac{\partial}{\partial z} + \frac{1}{C}\frac{\partial}{\partial t}\right)\mathcal{E} - \frac{1}{2ik}\nabla_t^2\mathcal{E} = \mathcal{P}, \qquad (a)$$

$$\mathcal{P} = \sum_{\text{transitions}} \mathcal{P}_{IJ}, \qquad (b)$$

$$\frac{\partial \mathscr{P}}{\partial t}_{IJ} = (-\gamma + i\,\Delta\omega_{IJ})\mathscr{P}_{IJ}$$

$$J > I$$

$$+ \frac{k}{2\epsilon_0 \hbar} S_{IJ} \mathscr{E}(\rho_L/g_I - \rho_J/g_J) , \qquad (c)$$

and

$$\frac{\partial \rho_I}{\partial t} = \lambda_I - \gamma_I \rho_I + \frac{1}{\hbar\omega} \left\{ \sum_{K<I} (\mathscr{E}\mathscr{P}^*_{KI} + \text{c. c.}) - \sum_{K>I} (\mathscr{E}\mathscr{P}^*_{IK} + \text{c. c.}) \right\} , \qquad (d)$$

where $S_{IJ}$ is a line strength and the other symbols have their usual meanings. In these equations $\rho_I$, $\mathscr{P}_{IJ}$, and $\mathscr{E}$ are functions of the cylindrical coordinates r and z and of time t. There are six level densities, six complex *medium polarization densities* corresponding to the six transitions between levels, and the one complex electric field amplitude.

In order to integrate the parabolic partial differential equation for $\mathscr{E}$ with numerical stability, one should use an implicit technique.[44, 45] We use the Crank-Nicolson method with the Thomas alorithm[44] for the solution of the banded matrix system. In order to use this method efficiently, the *two-step predictor-corrector integration method* of Icsevgi and Lamb[46] was abandoned in favor of the simpler Heun method,[44] which is used as a single step predictor-corrector. In terms of retarded time, the Maxwell-Bloch equations can be symbolically written as

$$\left(\frac{\partial}{\partial z} - \frac{1}{2ik}\nabla_t^2\right) \mathscr{E} = \mathscr{P} , \qquad (15a)$$

$$\frac{\partial}{\partial t} \mathscr{M}_n = f_n . \qquad (15b)$$

$\mathscr{M}_n$ has been used to denote any of the 12 dependent variables relating to the medium. The presence of off-resonant transitions in these Maxwell-Bloch equations necessitates a small integration step size in time. One must allow for a time grid of the order of 500 points. The number of radial points depends on the divergence of the paraxial beam; the number may vary from 100 to several thousand for divergent beams. The number of points in axial distance z varies widely, depending upon the amplifier length and gain. In order to make the problem tractable in storage and speed on our larger computers, the following design has been chosen for the computation. Let $\underline{\mathscr{E}}(z, t)$ and $\underline{\mathscr{M}}_n(z, t)$ be vectors representing the dependent variables at a particular z and t. Each element is the value at a given radius. In this vector notation, the transverse Laplacian becomes a banded matrix operator:

$$\frac{1}{2ik}\nabla_t^2 \rightarrow \underline{D} .$$

The Maxwell-Bloch equations may now be written as

$$\left(\frac{\partial}{\partial z} - \underline{D}\right) \underline{\mathscr{E}} = \underline{\mathscr{P}} , \qquad (16a)$$

$$\frac{\partial}{\partial t} \underline{\mathscr{M}}_n = \underline{f}_n . \qquad (16b)$$

The implicit predictor-corrector algorithm for integrating the equations can now be described easily; let superscript P denote a predicted value, superscript C a corrected value. First, predict $\underline{\mathscr{E}}$ by advance in z *using the Crank-Nicolson-Thomas procedure.*

$$\underline{\mathcal{E}}^{P}(z, t) = (\underline{1} - 1/2\ \underline{D})^{-1} \left\{\Delta z\ \underline{\mathcal{P}}(z - \Delta z, t) + (\underline{1} + 1/2\ \underline{D})\ \underline{\mathcal{E}}(z - \Delta z, t)\right\}. \quad (17a)$$

Second, predict all medium quantities by advance in t:

$$\underline{\mathcal{M}}_n^{P}(z, t) = \underline{\mathcal{M}}_n(z, t - \Delta t) + \Delta t\ \underline{f}_n(z, t - \Delta t). \quad (17b)$$

Third, evaluate predicted time derivatives using all the predicted dependent variables:

$$\left(\frac{\partial \underline{\mathcal{M}}_n}{\partial t}\right)^{P} = \underline{f}_n^{P}(z, t). \quad (17c)$$

Fourth, compute the corrected electric field by Crank-Nicolson-Thomas advance in z:

$$\underline{\mathcal{E}}^{C}(z, t) = (\underline{1} - 1/2\ \underline{D})^{-1} \left\{1/2\Delta z \left(\underline{\mathcal{P}}(z - \Delta z, t) + \underline{\mathcal{P}}^{P}(z, t)\right) + (\underline{1} + 1/2\ \underline{D})\ \underline{\mathcal{E}}(z - \Delta z, t)\right\}. \quad (17d)$$

Finally, obtain corrected medium quantities by time advance:

$$\underline{\mathcal{M}}_n^{C}(z, t) = \underline{\mathcal{M}}_n(z, t - \Delta t) + 1/2\Delta t \left\{\underline{f}_n^{P}(z, t) + \underline{f}_n(z, t - \Delta t)\right\}. \quad (17e)$$

Rapidly accessible disc file storage is used for the electric field and medium polarization. At a particular z, the vectors (radial variation) are stored end-to-end in order of increasing time on the disc file:

$$\underline{\mathcal{E}}(z, o), \underline{\mathcal{P}}(z, o), \underline{\mathcal{E}}(z, \Delta t), \underline{\mathcal{P}}(z, \Delta t), \ldots \underline{\mathcal{E}}(z, t_N), \underline{\mathcal{P}}(z, t_N),$$

where $t_N$ is the final time point used in the time grid. This procedure requires storage of only about 90 radial vectors in the computer memory at any instant. Typical calculations have required from 1 to 5 minutes CDC-7600 execution time for a single pulse's evolution through the SAIL-1 main amplifier.

This code (called TZYR for t, z, and r) has been utilized for the gain saturation calculations described elsewhere in this report. The code is in a state of modification since it is still to be amalgamated with more powerful wave propagation codes being developed.

## Approximations to Maxwell-Bloch Equations Suitable for Longer Pulses

Since the SAIL-1 oscillator is capable of producing pulses of the order of 200 ps and shorter, the basic theoretical description of amplification in the iodine system began with the Maxwell-Bloch equations which properly account for coherent transient effects through the medium polarization decay rate. In the event that longer pulses become of interest, as appears likely in the laser fusion program, we can approximate the Maxwell-Bloch equations in the standard manner that leads to the photon rate equations. Thus, instead of integrating the differential equations for

the six complex, oscillatory medium polarization densities, one approximates them as functions of the local field, i.e.:

$$\mathcal{P}_{IJ} \sim (\gamma - i\Delta\omega_{IJ})^{-1} \frac{k}{2\epsilon_0 \hbar} S_{IJ}$$

$$\mathcal{E}(\rho_I/g_I - \rho_J/g_J) \quad . \tag{18}$$

This approximation saves considerable computer time for it effects a reduction in the number of points in the time grid. The electric field envelope and the medium level densities are still integrated as before.

A few computational tests were run to evaluate the accuracy of this approximation as to the effect on pulse phase distortion. For pulses of the order of 200 ps, the results were not encouraging and it was decided not to make use of the approximation. However, the pulse phase distortion predicted by the Maxwell-Bloch theory settled down to the phase predicted by this approximation in the trailing edge of the pulse. Thus one would find the approximation useful for pulses of the order of 1 ns or perhaps even shorter.

A further, more drastic, but nevertheless useful, approximation is to reduce the photon rate equations for a six-level system to a two-level model. In this case the amplification process is described by

$$\left(\frac{\partial}{\partial z} + \frac{1}{c}\frac{\partial}{\partial t}\right) I = \sigma_{se}\, In \tag{19}$$

$$\frac{\partial}{\partial t} n = -b \frac{I}{h\nu} \sigma_{se}\, n \quad , \tag{20}$$

where $I$ is intensity, $n$ is inversion density, $\sigma_{se}$ is the stimulated emission cross section, and $b$ is $1 + g_U/g_L$. The solution to these equations may be written out algebraically.[47, 48] A small computer code (TWOL) was written to evaluate chained amplification based on this two-level model. It has been used to predict long pulse extraction efficiencies in the current SAIL-1 system.

## Development of More Advanced Wave Propagation Codes

Our two-dimensional, time-dependent Maxwell-Bloch code ("TZYR") described elsewhere in this report solves in cylindrical coordinates for the propagation of a pulse through an amplifier. This is appropriate in most cases since the length of a given amplifier is normally much shorter than the Rayleigh range ($1/2\ kw^2$) characteristic of the beam size ($w$) inside the amplifier. Thus, if the beam is injected at near-collimation, it will not undergo significant diffraction spreading before exiting the amplifier. However, two serious problems arise with the use of cylindrical coordinates. First, propagation between amplifiers must allow for large increases in beam size (e.g., the Asterix design[49]), and, secondly, beams may not always be collimated before injection into the amplifiers. In either case the use of a cylindrical coordinate system requires a large number of radial grid points and a prohibitive amount of computer time. What is needed is a coordinate system that follows the expansion of the beam and also allows for the factorization of divergent phase fronts from the electric field envelope, $\mathcal{E}$. In the case of laser beams propagated long distances through the atmosphere, it is advantageous to use a coordinate system adapted for pure Gaussian beams.[45] Although the SAIL-1 oscillator beam is well characterized by a Gaussian, amplification-induced phase distortions and transverse profiles soon destroy the Gaussian character. We have decided to implement the following coordinate transformation to enable our numerical grids to adapt to the local properties of the propagating pulse.

Consider the usual Maxwell-Bloch equations for the electric field envelope and the medium quantities that evolve in time (written in retarded coordinates).

$$\left[\frac{\partial}{\partial z} - \frac{1}{2ik}\left(\frac{\partial^2}{\partial r^2} + \frac{1}{r}\frac{\partial}{\partial r}\right)\right]\mathcal{E} = \mathcal{P}, \qquad \text{(a)}$$

$$\frac{\partial}{\partial t}\mathcal{M}_n = f_n \qquad \text{(b)}$$

If the pulse is propagating in free space, $\mathcal{P}$ is zero. Now make the following coordinate transformation,

$$s = z$$

$$\theta = r/z\ ,$$

or

$$r = s$$

$$r = s\theta\ .$$

The differential equation for $\mathcal{E}$ becomes

$$\left[\frac{\partial}{\partial s} - \frac{\theta}{s}\frac{\partial}{\partial \theta} - \frac{1}{2ik}\frac{1}{s^2}\left(\frac{\partial^2}{\partial \theta^2} + \frac{1}{\theta}\frac{\partial}{\partial \theta}\right)\right]\mathcal{E} = \mathcal{P}. \qquad (21)$$

We now may make a dependent variable transformation to remove the phase factor associated with a divergent beam. It is also convenient to factor an $s^{-1}$ dependence at this point:

$$\mathcal{E} = \frac{1}{s}\, e^{-i\frac{k}{2}s\theta^2}\, \mathcal{E}'$$

$$\mathcal{P} = \frac{1}{s}\, e^{-i\frac{k}{2}s\theta^2}\, \mathcal{P}'$$

The equation for $\mathcal{E}'$ becomes

$$\left[\frac{\partial}{\partial s} - \frac{1}{2ik}\frac{1}{s^2}\left(\frac{\partial^2}{\partial \theta^2} + \frac{1}{\theta}\frac{\partial}{\partial \theta}\right)\right]\mathcal{E}' = \mathcal{P}'\ . \qquad (22)$$

Note that the quantities factored from $\mathcal{E}$ may be written as

$$\frac{1}{s}\, e^{-i\frac{k}{2}s\theta^2} = \frac{1}{z}\, e^{-i\frac{k}{2z}r^2}\ ,$$

which is exactly the paraxial phase front and amplitude decay associated with a beam emitted from a source at z = 0.

The great practical advantage is that the integration of the new parabolic partial differential equation for $\mathcal{E}'$ is very similar to the previous one for $\mathcal{E}$ in cylindrical coordinates. Thus we may use the Crank-Nicolson-Thomas method virtually unchanged. The coordinate grid in r now becomes a grid in the angular variable $\theta$, which expands or contracts to follow the beam propagation. The only parameter to be fixed is the origin of s (or z), which controls the rate of expansion of the grid with distance. We are presently investigating methods of choosing this parameter and will begin numerical investigation of the use of this coordinate system in a free space propagation code.

## Fox-Li Calculations for Iodine Oscillator

Aperture measurements of the radial profile of the oscillator beam in SAIL-1 confirmed that the beam has a Gaussian profile at 6 m from the exit window of the oscillator cavity. The divergence angle ($\lambda/\pi\, w_o$) is determined to be 318 $\mu$rad. The beam is well characterized as Gaussian $TEM_{oo}$ mode

with an electric field waist $w_o$ of 1.316 mm located 1 m outside the plane-plane cavity. We have adopted this characterization of the oscillator beam for all theoretical studies. The question arose as to the unusual location of the waist. Fox-Li calculations were performed for the oscillator cavity including the apertures in front of both plane mirrors. These calculations used our wave propagation code "FOCUS," described previously.[50] As soon as the iterative cavity calculations stabilized, the beam was propagated outward from the cavity. Figure 58 displays the predicted behavior of the waist (here defined as the $1/e^2$ point of the radial intensity variation) with distance. The fact that this simple calculation could display a slight contraction of the beam outside the cavity lends considerable weight to the empirical beam characterization. The far-field divergence angle is predicted quite accurately.

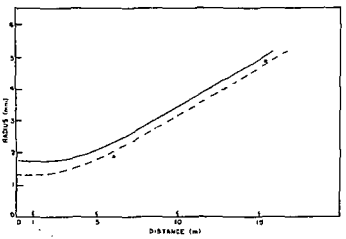


Fig. 58. Variation of SAIL-1 oscillator beam radius with distance.

## Chemical Recovery of Laser-Medium Starting Materials

If the iodine laser is to prove attractive as a candidate for laser fusion applications, it must be shown to be capable of efficient operation in addition to having suitable optical output. This section discusses the role chemical reactions play in determining the overall efficiency of an iodine laser and indicates Sandia's approach toward optimizing chemical efficiency. A kinetic model is presented and used to calculate the consumption of chemical starting material associated with laser operation. This consumption depends sensitively on several chemical kinetic rate constants, some of which are not known accurately and must therefore be determined.

The recent results of experimental efforts to determine important rate constants are summarized. Results of model calculations make it clear that it is economically unattractive to replace chemicals consumed during laser operation by purchasing new starting material. A scheme for regenerating starting material from by-products of laser operation is presented. The energy expanded in the regeneration process is estimated to be a minor component of the total energy required to operate a laser.

*Kinetic Model and Calculated Chemical Consumption* -- The iodine laser operates on the $5^2P_{1/2} - 5^2P_{3/2}$ transition of the iodine atom. Excited atoms are produced by near-ultraviolet photolysis of iodine-bearing compounds, RI. Typically, the R group is $C_nF_{2n+1}$, that is, a perfluoroalkyl radical. These species are chosen because they yield on photolysis a large value of $I^*$, the fractional atomic excited state population, and because the collisional deactivation of the excited atoms $I^*$ by R is slow. The working medium of a typical iodine laser amplifier[51] is a mixture of RI highly diluted in argon. The argon serves to pressure-broaden the lasing transition and to minimize the temperature rise resulting from the absorption of the pumping radiation. Reference 52 summarizes much of the physics and chemistry of the iodine laser.

When pure RI is subjected to intense, unfiltered ultraviolet radiation from a high-current flashlamp, a multitude of reaction products is obtained.[53] Use of a filter which blocks wavelengths less than 220 nm eliminates many undesirable effects of photolysis,[54] and dilution of RI with Ar eliminates the pyrolytic decomposition of RI.[52] Only when the temperature of the working medium

exceeds about 900 K are products other than RI, $R_2$, $I_2$ and buffer gas (if used) found in the working medium after photolysis.[55] The temperature in the amplifier of the Sandia atomic iodine laser, SAIL-1, does not exceed 400 K, and filters blocking short wavelengths are used. Thus, a fairly simple set of chemical reactions is sufficient. The amplifier model treated here includes the following processes:

$$RI + h\upsilon_{UV} \xrightarrow{f^*} R + I^* \qquad (1)$$
$$\xrightarrow{1 - f^*} R + I$$

$$\Delta N(t_{ex}) \longrightarrow (1 + SAT)^{-1}\Delta N(t_{ex}) \qquad (2)$$

$$I^* + R \xrightarrow{k_3 = k_{RI^*}} RI \qquad (3)$$

$$I^* + I_2 \xrightarrow{k_4} I + I_2 \qquad (4)$$

$$I + R \xrightarrow{k_5 = k_{RI}} RI \qquad (27)$$

$$I + I + Ar \xrightarrow{k_6} I_2 + Ar \qquad (28)$$

$$R + R \xrightarrow{k_{RR}} R_2 \qquad (29)$$

Process (23) represents the ultraviolet photolysis of the starting material RI. The photolysis pulse is assumed to be of the form $I(t/\tau)^N e^{-t/\tau}$, where I governs the irradiation intensity, and N and $\tau$ are chosen to give the desired pulse shape. A fraction $f^*$ of the photolytically produced iodine atoms appears in the excited state. Reference 52 tabulates $f^*$ for most of the compounds for which it has been determined experimentally. Process (24) represents the extraction of optical energy from the amplifier by a very short input pulse occurring at the time $t_{ex}$. For the cases discussed here $t_{ex} = 2\Delta t_{pump}$, where the latter quantity is the temporal full-width-at-half-maximum intensity of the photolysis pulse. It is assumed that energy is extracted from both upper hyperfine levels with equal efficiency, governed by the parameter SAT. Processes (25) through (29) embody the kinetics considered here. The rate constants $k_4$ and $k_6$ are well known and are $k_4 = 3.6 \times 10^{-11}$ cm$^3$ sec$^{-1}$,[56] $k_6 = 6.7 \times 10^{-33}$ cm$^6$ sec$^{-1}$.[57] A survey of the literature[58] indicates that $k_3$, $k_5$, and $k_{RR}$ are well determined for at most only a few R groups. For the calculations reported here, the following values were assumed: $k_5 = 5 \times 10^{-11}$ cm$^3$ sec$^{-1}$, $k_3 = 1.5 \times 10^{-12}$ cm$^3$ sec$^{-1}$; $k_{RR}$ is a variable parameter. The value of $k_{RR}$ for a given R group is chosen by reference to the literature or by reasonable extrapolation. Processes (23) through (29) encompass most of those currently thought to be important in an iodine amplifier.[52] Calculations were performed for more extensive sets of kinetic processes by including

$$I^* + Q \xrightarrow{k_8 = k_Q} I + Q \qquad (30)$$

$$I^* + I + Ar \xrightarrow{k_9} I_2 + Ar \qquad (31)$$

$$R + I_2 \xrightarrow{k_{10} = k_{RI_2}} RI + I \qquad (32)$$

and by allowing $k_3$, $k_5$, and $k_{10}$ to change as $k_{RR}$ was varied. In Equation (30) Q is a species in the working medium which quenches excited iodine atoms. Calculations utilizing expanded sets of kinetic processes gave results qualitatively similar to those reported here. The expanded-set calculations did not, however, fit the data on loss of RI associated

with laser operation, reported by Fuss and Hohla,[59] as well as those based on Equations (23) through (29) only.

Figure 59 illustrates typical results obtained by numerical integration of the differential equations appropriate to the model discussed above, considering only Equations (23) through (29). The quantity M, the number of molecules of RI consumed per laser output photon (or twice the number of $R_2$ or $I_2$ molecules thus formed), is plotted as a function of $k_{RR}$ for three values of $\Delta t_{pump}$. There is a significant dependence of M on $\Delta t_{pump}$ for $\Delta t_{pump} \gtrsim 1\ \mu s$ because, in this regime, appreciable R - R association can occur during pumping if a long photolysis pulse is used. Labeled dots on the $\Delta t_{pump} = 1\ \mu s$ curve identify the estimated values of $k_{RR}$ for several compounds of interest. M depends strongly on $k_{RR}$, but can be constrained to $M < 0.1$ for any photolysis pulse width considered if $k_{RR} \lesssim 4 \times 10^{-14}\ cm^3\ sec^{-1}$. It is obvious that precise predictions of M require an accurate knowledge of $k_{RR}$, and evaluation of this parameter for compounds of interest is the main goal of Sandia's experimental work in the area of determining chemical reaction rate constants. The constants $k_3$ and $k_5$ are also important and will be determined simultaneously with $k_{RR}$.

Any RI consumed during laser operation must be replaced; if replacement is through purchase of additional RI, the following argument indicates that the replacement cost is not economically attractive. The current cost of $C_3F_7I$ is about $300 per mole in 10-kg lots; for simplicity this price is also assumed for $t\text{-}C_4F_9I$. Using the values of M displayed in Fig. 59 for $\Delta t_{pump} = 1\ \mu s$, the costs of replacing the RI lost in the generation of 1 kJ iodine laser output are: $t\text{-}C_4F_9I$, $0.13; $i\text{-}C_3F_7I$, $0.40; $n\text{-}C_3F_7I$, $1.06. If an overall electrical efficiency of 1% is assumed for the laser and if the cost of electricity is $0.01 per MJ, then the cost of the electricity required for 1 kJ of laser output is $0.001. It is clear that chemical replacement cost strongly dominates electrical energy cost and would continue to do so even if chemical prices were reduced by a large factor. This indicates that a practical operation of a large-scale iodine laser requires regeneration of products to starting materials by a process which does not require more energy than that used in pumping the laser. The following material discusses Sandia's programs in the determination of chemical reaction rate constants and the development of an attractive regeneration process.


Fig. 59. Effects of radical-radical association rate constant and photolysis pulse width (FWHM) on consumption of starting material in an iodine laser amplifier. Labeled dots identify estimated values of $k_{RR}$ for several compounds of interest.

Determination of Chemical Reaction Rate Constants -- The method employed at Sandia for determining rate constants involves measuring the energy gain in an iodine amplifier as a function of time after activating the amplifier medium using a flashlamp pump.[60] An advantage of this technique is that data are obtained in systems very similar to actual lasers. Because gain depends on the concentrations of both excited and ground state iodine atoms, it is influenced by any reaction influencing either of these concentrations. All the reactions considered in the kinetic model presented earlier, except reaction (23), influence directly either

the concentration of ground or excited state iodine atoms. Reaction (23), $R + R \longrightarrow R_2$, influences both these concentrations, but only indirectly, by removing one of the reactants in reactions (25) and (27). Rate constants are obtained from gain-versus-time data by computer fitting the data with kinetic models using rate constants as variable parameters.

Early work at Sandia[60, 61] was aimed at establishing the reliability of the gain-versus-time technique and consequently was performed in relatively simple systems for which many of the reaction rate constant were known. This work demonstrated the validity of the technique but did not determine its sensitivity to $k_{RR'}$, the most important parameter for predicting consumption of starting material. Numerical calculations of gain-versus-time curves, based on the model presented earlier, indicate that the data should be quite sensitive to $k_{RR'}$. Figure 60 presents calculated curves for two values of $k_{RR}$ with other model parameters held fixed. The qualitative difference in curve shapes indicates that the gain-versus-time method can be used to determine $k_{RR}$ with good precision. This has been confirmed in two ways. First, the curves of Fig. 60 were fitted with the standard gain-versus-time computer analysis techniques, and sensitivity to $k_{RR'}$, $k_3$, and $k_5$ was established. Second, experimental work was extended to the n-$C_3F_7I$ - Argon system. Figure 61 shows experimental data and two computer fits. The fit of lower quality ignores all radical-radical reactions, and the fit of higher quality includes reactions (25), (27), and (29). Table V presents a summary of the overall analysis of data presented in Fig. 61 along with other data taken for different conditions in the n-$C_3F_7I$ - Argon system. Estimated uncertainties reflect the sensitivity of the computer analysis routines to the various rate constants. Comparisons with literature values are indicated where applicable.

A comparison of the values of the radical-radical reaction rate constants given in Table V with the estimates used to calculate the curves in Fig. 59 indicates that the original estimates were somewhat high. This illustrates the difficulty of estimating unknown chemical kinetic parameters. The experimental and computer techniques for obtaining and analyzing gain-versus-time data are now well established; they must be applied to a series of perfluoroalkyl iodide systems to generate reliable data for the computation of chemical consumption in iodine lasers.

TABLE V

Results of Kinetic Analysis of Gain vs. Time Data Obtained with a $C_3F_7I$ Iodine Laser Amplifier

$f^* = 1.0 \left(^{+0.0}_{-0.05}\right)$

$k_Q(R1) = 3 \pm 2 \times 10^{-15}$ cm$^3$/molecule-sec

$k_{R1^*} = 2 \pm 1 \times 10^{-13}$ cm$^3$/molecule-sec

$k_{21} = 1 \pm .5 \times 10^{-12}$ cm$^3$/molecule-sec

$k_{RR} = 1.5 \pm .5 \times 10^{-13}$ cm$^3$/molecule-sec

$k_{R1_2} = 2 \pm 1 \times 10^{-12}$ cm$^3$/molecule-sec

Literature Values

$k_{Q(R1)} = 8 \times 10^{-16}$ cm$^3$/molecule-sec Zalesskii and Krupenikova, 1971[62]

$k_{R1^*} = 4 \times 10^{-13}$ cm$^3$/molecule-sec, Kuznetsova and Maslov, 1974[63]

$k_{R1} = 9 \times 10^{-12}$ cm$^3$/molecule-sec, Kuznetsova and Maslov, 1974[63]

$f^* = > 0.99$ Donohue and Wiesenfeld, 1975[64]

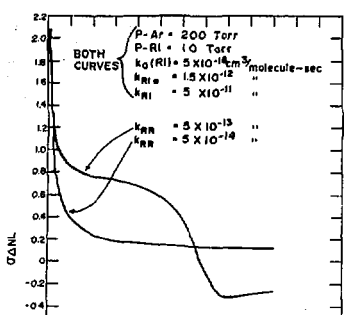


Fig. 60. Computer simulated iodine laser amplifier gain vs. time for two radical-radical association rates.

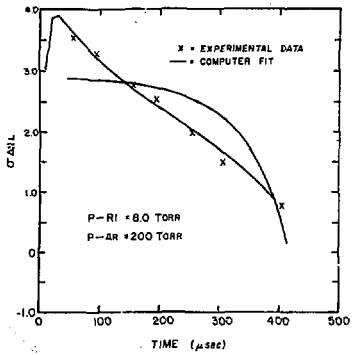


Fig. 61. Gain vs. time in an iodine laser amplifier: $C_3F_7I$.

Chemical Regeneration Scheme -- This material treats two variants of a scheme fc regenerating RI from $R_2$ and $I_2$ and estimat the efficiency of the regeneration process. Schemes for regenerating RI from species other than $R_2$ and $I_2$ are not discussed because, as was indicated in the discussion o the kinetic model, such species are not formed under typical amplifier operating conditions. The dissociation energies of C-C, I-I, and C-I bonds are 3.60 eV, 1.6 e and 2.4 eV, respectively. Thus the minimum energy expenditure for the process

$$R_2 + I_2 \longrightarrow 2\ RI \qquad (33$$

is about 0.2 eV per molecule of RI produced Unfortunately, no scheme for carrying out Equation (33) with an energy expenditure approaching this minimum value has ever been devised. The difficulty in devising efficient schemes for carrying out Equation (33) arises from the fact that $R_2$ is a perfluoroalkane and these species are exceptionally stable, exhibiting virtually no chemical reactions. It presently appears tha., in order for Equation (33) to proceed, it is necessary to break the C-C bond uniting the two R groups. The reaction

$$R + I_2 \longrightarrow RI + I \qquad (34$$

will then proceed spontaneously.[65] If the required C-C bond cleavage can be performe selectively, chemical regeneration can be made relatively efficient. If a nonselective technique such as pyrolysis is used to break C-C bonds,[66] the overall efficiency of the regeneration process will be appreciably lower.

One conceptually simple scheme for carrying out Equation (33) is the following two-step process: Multiple photon dissociation o $R_2$, followed by reaction of R with $I_2$ as described by Equation (34). Specifically, a mixture of $R_2$ in an excess of $I_2$ is irradiate

with an intense infrared laser pulse. During the pulse an individual $R_2$ absorbs enough photons that it can decompose unimolecularly. The overall pressure of the mixture is adjusted to such a value that, for the $R_2$ excitation level under consideration, decomposition through C-C bond breakage occurs on the average before the occurrence of collisions which might deactivate the excited $R_2$. The R fragments then react with $I_2$ to form RI. This reaction occurs after the laser pulse is over, thus the RI formed will not be excited or decomposed by irradiation.

The calculations required to estimate the excitation energy required for a given $R_2$ unimolecular dissociation rate can be carried out easily under the assumption that excitation energy is randomly distributed in the $R_2$ molecule. RRKM theory yields the approximate relation[67]

$$k_{\substack{uni \\ C-C}}(sec^{-1}) = \upsilon_{vib}\left(\frac{\varepsilon_{C-C}}{\varepsilon_{C-C} + D_{C-C}}\right)^n , \quad (35)$$

where $k_{\substack{uni \\ C-C}}$ is the dissociation rate through the desired C-C bond cleavage, $\upsilon_{vib}$ is an average molecular vibrational frequency, $\varepsilon$ is the total internal energy in excess of the C-C bond energy $D_{C-C}$, and n may be taken to be the total number of vibrations in the molecule. (See Reference 64 for a more exact but only slightly different definition of n. The difference is inconsequential here.) The quantity $\varepsilon_{C-C}$ is related to other energies by

$$\varepsilon_{C-C} = E_{IR} + E_{thermal} - D_{C-C} , \quad (36)$$

where $E_{IR}$ is the amount of energy absorbed by a molecule from the infrared laser beam and $E_{thermal}$ is the average thermal excitation. The expression for $k_{\substack{uni \\ C-F}}$ is analogous to Equation (35) except that the C-F bond dissociation energy, $D_{C-F} = 5.0$ eV, must be substituted for $D_{C-C}$, and the overall expression must be multiplied by the number of C-F bonds in $R_2$.

Figure 62 displays calculated values of $k_{uni}$ for the irradiation of $C_2F_6$ at an initial temperature of 300 K. The value of $\upsilon_{vib}$ was assumed to be $3 \times 10^{13}$ $sec^{-1}$. If the regeneration process is carried out at a total pressure of the order of 1 torr, $k_{\substack{uni \\ C-C}}$ must be of the order $10^6$ $sec^{-1}$ for $C_2F_6$ to dissociate to 2 $CF_3$ before any deactivating collisions occur. This requires that $E_{IR} \approx 5.7$ eV, and at this level of excitation $k_{\substack{uni \\ C-C}}/k_{\substack{uni \\ C-F}} > 10^7$. In general, the amount of energy which must be absorbed by $R_2$ molecules to regenerate the laser mixture is, per photon of laser output,

$$E_R = ME'_{IR}/2/s \quad (37)$$

where M is presented in Fig. 59 and $E'_{IR}$ is the absorbed energy yielding the desired $k_{\substack{uni \\ C-C}}$. For an amplifier using $CF_3I$ and having $\Delta t_{pump} = 1$ μs, the requirement $k_{\substack{uni \\ C-C}} = 10^6$ yields $E_R = 2.7$ eV. The corresponding energies for operation with n-$C_3F_7I$, i-$C_3F_7I$, and t-$C_4F_9I$ are 2.1 eV, 0.77 eV, and 0.33 eV, respectively. For comparison, the energy of an iodine laser photon is 0.94 eV. It must be mentioned that the regeneration scheme described here may not be appropriate for molecules such as $C_6F_{14}$ or $C_8F_{18}$. The reason is that the required energies $E'_{IR}$ are so high that C-C bonds other than the one joining the two R groups may break at a rate comparable to the decay rate in the desired channel. The C-C bond joining two i-$C_3F_7$ or two t-$C_4F_9$ groups is expected to be the weakest bond in an $R_2$ molecule, but a quantitative determination of the difference between its strength and that of the other C-C bonds is not available. The difference may not be large enough to ensure that the desired C-C cleavage occurs with nearly unit probability unless $\epsilon$ in Equation (35) is small. A regeneration process with small $\epsilon$ is described below.

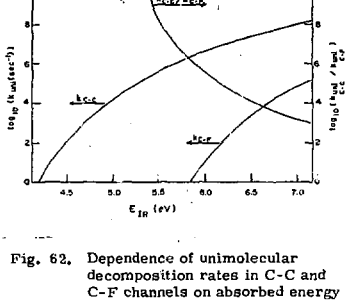


Fig. 62. Dependence of unimolecular decomposition rates in C-C and C-F channels on absorbed energy for the case of $C_2F_6$ irradiated at an initial temperature of 300° K.

The pulsed laser scheme described above is analogous to dissociation schemes pursued for $SF_6$[68] and other molecules[69, 70] for several years. It relies on the absorption of sufficient infrared quanta during a single laser pulse that decomposition occurs before collisional deactivation. The requirement of rapid dissociation leads to large ε. Recently the decomposition of ethane samples placed in the output beam of a CW $CO_2$ laser has been reported.[71] Ethane does not absorb $CO_2$ radiation at 10.6 μm, and decomposition occurred only when $SF_6$ and $C_2H_6$ were mixed. No decomposition of $SF_6$ was observed. The experiment is not yet well enough understood that the detailed kinetics can be interpreted, but absorption of radiation by $SF_6$ followed by efficient V-V energy transfer to $C_2H_6$ must be involved. The fact that the experiment is carried out in a CW rather than in a pulsed mode of operation removes the requirement of rapid unimolecular decay and allows for the possibility of small ε. Reference 71 reports that the absorbed energy per molecule of $C_2H_6$ decomposed was 3.8 eV under the best attainable experimental conditions and predicts that lower values would be obtained with higher power $CO_2$ laser excitation. $D_{C-C} = 3.6$ eV; thus, the above remarks and reference to Equation (36) indicate that the CW decomposition scheme can indeed be used to dissociate molecules under conditions for which ε is small and selectivity is maintained.

There appears to be no reason why the technique discussed above should work only for $C_2H_6$. $C_2F_6$ and other $R_2$ molecules have energy levels lying close to the appropriate levels in $SF_6$, and V-V energy transfer from $SF_6$ to $H_2$ should be an efficient process. Chemical regeneration using the energy transfer scheme could be carried out as follows. A mixture of $SF_6$ and $R_2$ diluted in Ar is flowed through the output beam of a CW $CO_2$ laser, resulting in dissociation of $R_2$ to 2R. Immediately downstream of the excitation region $I_2$ is mixed into the stream to allow the regeneration of RI. The relation (37) may still be used to calculate $E_R$, but now $E'_{IR} \approx D_{C-C}$ for all species $R_2$. This means that the CW regeneration process would be appreciably more efficient than the pulsed one.

It is now possible to estimate the efficiency of the chemical regeneration process and to compare it to the estimated efficiency of the pumping process. Consider a figure of merit η, customarily called the efficiency, defined for closed loop amplifier performance as

$$\eta = \frac{\text{extracted laser energy}}{\text{total input energy}} \quad . \tag{38}$$

If several operational steps are involved, and $\eta_i$ for step i is defined in a manner analogous to Equation (38), then

$$\eta^{-1} = \sum_i \eta_i^{-1} \quad . \tag{39}$$

Only the pumping (electrical) figure of merit $\eta_P$ and the chemical regeneration figure of

merit $\eta_R$ will be considered here. The value of $\eta_R$ is related to $E_R$ defined in Equation (37) by

$$\eta_R = \frac{0.94\ \eta_L \phi}{E_R(eV)} \quad , \tag{40}$$

where 0.94 eV is the energy of an iodine laser photon, $\eta_L$ is the overal figure of merit of the infrared laser used in the regeneration process, and $\phi$ is the fraction of the infrared photons actually utilized. For purposes of evaluating $\eta_R$, it is assumed that the infrared laser used is a $CO_2$ laser (typical $R_2$ species absorb in the region of the $CO_2$ laser output).[72] The value of $\eta_L$ is assumed to be 0.2. This value can be attained in either pulsed[73, 74] or CW[75] operation. The best current estimate of $\phi$ for pulsed experiments is 0.5; the data in Reference 47 indicate that $\phi \approx 1$ for carefully conducted CW experiments. The numbers for $\eta_L$ and $\phi$ given here together with values cited earlier for $E_R$ and the information contained in Fig. 48 are used to construct Table VI.

TABLE VI

Tabulation of Estimated Figures of Merit $\eta_R$ for Pulsed and CW Chemical Regeneration Processes

(Assumed value of $\Delta t_{pump}$ is 1 $\mu$s)

| | Pulsed | | CW | |
|---|---|---|---|---|
| RI | $E_R$(eV) | $\eta_R$ | $E_R$(eV) | $\eta_R$ |
| $CF_3I$ | 2.7 | 0.03 | 1.7 | 0.11 |
| $i\text{-}C_3F_7I$ | 0.77 | 0.12 | 0.22 | 0.86 |
| $t\text{-}C_4F_9I$ | 0.33 | 0.29 | 0.07 | 2.6 |

The data in Table VI apply only for $\Delta t_{pump}$ = 1 $\mu$s. Values of $\eta_R$ for other photolysis pulse widths may be determined by using the appropriate data in Fig. 59. Values of $\eta_R$ are given for both pulsed and CW regeneration processes for comparison purposes, but the reservations expressed earlier concerning the use of the pulsed technique with large molecules should be remembered. The CW process is more efficient than the pulsed one by a factor that increases with increasing size of the RI molecule. The reason for this can be seen by inspecting Equation (35). For a given value of $k_{uni}$, $\epsilon$ increases with n. Only when a low value of $k_{uni}$ is acceptable can the dissociation process proceed with small $\epsilon$, more or less independent of n. There is, of course, a lower limit on the value of $k_{uni}$ which is acceptable in a given experiment, and actual values of $\eta_R$ for large molecules regenerated in a CW process consequently may be smaller than those reported in Table VI.

Based on the foregoing material, it seems reasonable to predict that a chemical regeneration process with $\eta_R \approx 0.1$ to 0.2 can be found. It is instructive to compare this estimate to the expected pumping efficiency $\eta_P$. In the case of photolysis using conventional flashlamps, $\eta_P$ is the ratio of energy extracted from the amplifier to energy stored in the flashlamp capacitor bank. It has been estimated[76] that with conventional flashlamp pumping the maximum attainable electrical efficiency is $\eta_P \approx 0.01$. Experimentally determined efficiencies[77-79] are a factor of two or more lower than this estimate. When estimated values of $\eta_R$ and $\eta_P$ are compared and considered in terms of Equation (39), it is clear that the overall figure of merit for an iodine laser should not be strongly influenced by the requirement of chemical regeneration, if conventional flashlamp pumping is used. A much more efficient pump source would have to be found before $\eta_R$ could become the limiting term in the overall operational figure of merit, if the above regeneration scheme is in fact successful.

Work currently in progress at Sandia will investigate experimentally the regeneration scheme discussed here. A pulsed, line-tunable $CO_2$ laser has been obtained for use as the irradiation source. Infrared spectroscopic and mass spectrometric systems are

being assembled for use as diagnostic tools. Initial irradiation experiments with $C_2F_6$ will commence shortly. Although only laser-based chemical regeneration has been discussed here, there is some indication in the literature that perfluroalkanes may be dissociated efficiently in low-frequency discharges.[80] This possibility will also be explored.

## Flashlamp Studies

Some previous studies on doped flashlamps were repeated because of some questions that were raised by ILC, and we developed a phenomenological model of doped flashlamps.[81] Figure 63 shows the light as detected with a 2800 ± 100 Å interference filter and a photomultiplier combination. The results represent three different experiments for which the vertical scale sensitivity is the same. It is to be noted that in the case of pure xenon (Fig. 63a) the light starts at the onset of breakdown. The second bump is due to the ringing of the discharge current. The addition of 60-mg $Zn_3P_2$ results (Fig. 63b) in several interesting observations: (1) The light output is delayed by approximately 5 μs, (2) the peak output is slightly higher than for pure xenon, and (3) the second peak is approximately twice as intense as it is for pure xenon. The first of these observations gives the key to a physical model for this doped discharge. When the gas breaks down, the arc channel begins to expand radially but little light escapes due to the opaque dopant film on the inside of the quartz wall. When the arc reaches the proximity of the wall, the dopant is blown off (much like a blow-off shutter) and now light can escape. The time scales and energies involved are consistent with Drabkina's[82] analysis. The relatively large increase in the second peak is due to dopant mixing with the arc. The above suggested that perhaps a more volatile dopant would give more dramatic results; thus, tellurium was added. The result is shown in Fig. 63c. Again, there is a 5-μs delay, but now the first peak was considerably bigger than in the other two cases, exactly as was anticipated. When the tube diameter was decreased to 8 mm ID the delay was 2.5 μs.

Considerable effort was also spent on analyzing promising ways to produce shorter pulse width photolysis sources, which are necessary to reduce the cost of chemical recovery of laser-medium starting materials.[83] These results indicate that it is necessary to shorten the pump pulse to ~ 1 μs (or less). Another advantage of short pump pulses is the avoidance of gas dynamic disturbances in the laser medium. Consequently, we have begun studies on short pulse width flashlamps. Some of these results are presented in Figs. 64 and 65. The results of these figures show that the optimum xenon pressure is a function of tube bore and discharge energy. In Fig. 64, results are presented for a charging voltage of 35 kV. The two curves represent integrated energies for 2 μs and 10 μs into the light pulse. We are pursuing a detailed program to evaluate the characteristics of short pulse lamps under repetitive operation and the efficiency and lifetime with which one can expect reasonable operation. We have found that the discharge circuit paramaterization used in Ref. 84 is acceptable for 1-μs discharge.

## SAIL-1/Streak Camera Response

In the previous Laser-Fusion Research Progress Report, reference was made to an experiment in progress for recording iodine laser pulses over a greater dynamic range. Now substantially completed, this study utilized Kodak Royal X Pan 4166 film, an extremely fast film which exhibits a dynamic range of several thousand. The streak camera system was known to be nonlinear at the iodine wavelength; i.e., the exposure level on film was increased to an extent greater than a corresponding increase in input intensity at the entrance slit. It was to be expected that the dynamic range of the camera-film system would be limited by this nonlinear instrumental response.

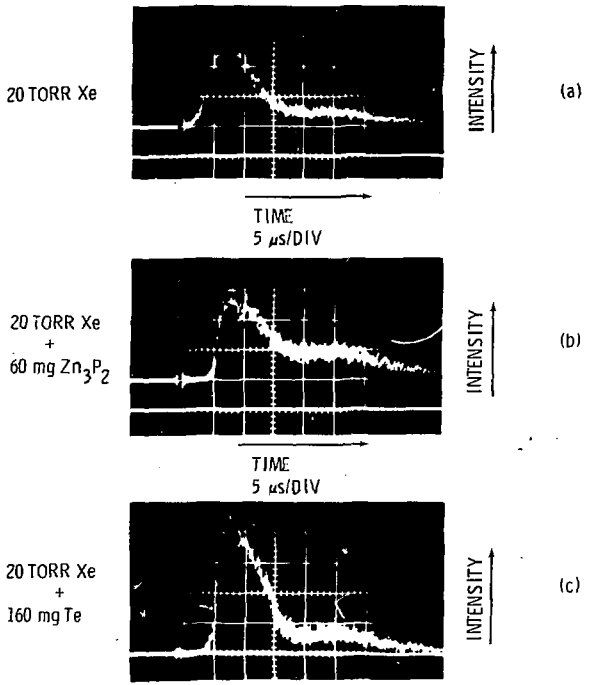


Fig. 63. The flashlamp light as detected with an interference filter (2800 ± 100 Å)/photomultiplier combination. The three cases (a, b, and c) were identical except insofar as the filling.

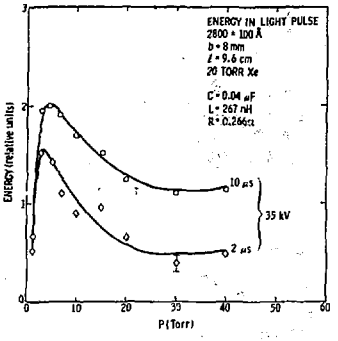


Fig. 64. The energy contained in 2 $\mu$s and 10 $\mu$s units of the flashlamp light contained in a band defined by an interference filter (2800 ± 100 Å). The tube bore was 8 mm.

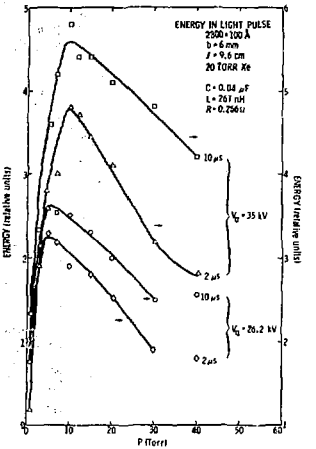


Fig. 65. The energy contained in 2 $\mu$s and 10 $\mu$s units of the flashlamp light contained in a band defined by an interference filter (2800 ± 100 Å). The tube bore was 6 mm.

As before, calibration data were taken using the SAIL-1 oscillator as the camera input source and operating the camera at a streak rate of $10^9$ cm/s. A split attenuator was included at the entrace slit, permitting two simulataneous exposures of a single input pulse at intensity levels differing by a factor of two. The input energy density level at the entrance slit was varied from approximately 1 $\mu J/cm^2$ to cover 30 $\mu J/cm^2$. Useful exposure levels on film were maintained by operating the image converter tube relay lens at progressively smaller apertures. Values for the relative apertures had been determined previously, and in all cases the follow-on image intensifier was operated at maximum gain.

Density samples obtained from the resulting photographs were used to construct a camera-film system response curve in terms of density versus relative $Log_{10}$ exposure. The film was also independently calibrated over an exposure interval of $10^{-3}$ s to simulated P11 phosphor light using a xenon flash sensitometer and appropriate band pass filters. Figure 66 shows a camera-film system response curve obtained for the camera operating at maximum sensitivity, and an independent film calibration curve. A Photometric Data Systems Model 1010 microdensitometer system was used for all data reduction.

The relative response of the camera system results from a comparison of the film response data as shown in Fig. 67. Here the nonlinearity previously mentioned is demonstrated and the maximum possible dynamic

range, approximately 50, is shown to lie between film exposure threshold and the level of exposure at which defocusing in the image converter streak tube occurs. The onset of defocusing was noted at an energy density of approximately 10 $\mu J/cm^2$ at the entrance slit for a nominal 200-ps pulse. A useful dynamic range of 30 seems realistic. This compares with a range of approximately 8 obtained using Polaroid Type 57 film.

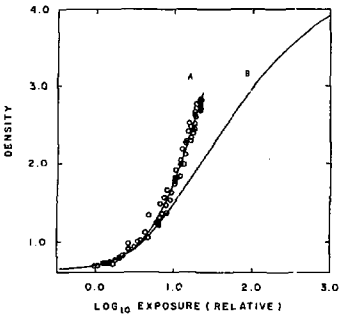


Fig. 66. Density vs relative log exposure for the streak camera system including film (curve A) and for film *independently exposed to simulated* P11 phosphor light (curve B). Royal X Pan 4166 film.

Photocathode Responsivity -- The image converter streak tube S-1 photocathode responsivity at $\lambda = 1.315\ \mu m$ has been revised, resulting in a substantially lower value. The photocathode current density ranges reported previously, while approximate, are valid for producing the photographic data reported; i.e., the range $10^{-11}$ to $10^{-10}$ $A/cm^2$ for low input intensity integrated over $1.6 \times 10^{-2}$ s and $3 \times 10^{-4}$ to $10^{-2}$ $A/cm^2$ for nominal

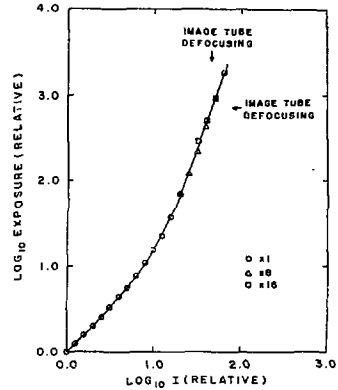


Fig. 67. Log exposure for Royal X Pan 4166 film vs log intensity at streak camera entrance slit, $\lambda = 1.315\ \mu m$. Image converter tube relay lens operated at maximum aperture (O); set for exposure decrease of 8x(Δ) and 16x (□).

200-ps iodine laser pulses to give useful exposure levels on Polaroid Type 57 film. An inconsistency was noted when these same current densities were calculated forward to give intensity density and ultimately energy density values at the photocathode and, in logical sequence, at the camera entrance slit.

The photocathode responsivity measurements were made using a tungsten ribbon filament lamp in combination with a small grating monochromator to illuminate the photocathode surface. Broad-band cut-off filters were introduced to eliminate unwanted orders passing through the monochromator. The bandpass was 13.2 nm FWHM using 2-mm slits and 3.3-nm FWHM using 0.5-mm slits.

The monochromator throughput was measured with a Hewlett-Packard Model 8330A Radiant Flux Meter and Model 8334A Radiant Flux Detector which had been calibrated against an Eppley lamp standard of total irradiance. In order to measure photocathode current, the image tube was operated as a simple diode. The extraction screen was used as the anode and operated at +500 V, and the photocathode was connected through a picoammeter to ground. Other external tube connections, the normal anode and deflection electrodes, were made common to ground.

In repeating the calibration, it was determined that the Corning 2-64 filter originally used to eliminate second order, $\lambda$ = 657.5 nm, in fact transmitted approximately 12 percent at this wavelength. Because the photocathode sensitivity is comparatively high at 657.5 nm, $2.2 \times 10^3$ A/W, an unrealistically high value of $1.31 \times 10^{-5}$ A/W was determined at 1.315 $\mu$m. Currently, two Corning 7-56 filters are used in cascade to give a total thickness of 5.08 mm for all measurements beyond $\lambda$ = 1 $\mu$m. (For a single 7-56 filter 2.11 mm thick, the measured transmission was $10^{-7}$ at $\lambda$ = 657.5 nm and $8.2 \times 10^{-1}$ at $\lambda$ = 1.315 $\mu$m.) With these cut-off filters, the responsivity at 1.315 $\mu$m was determined to be $1.69 \times 10^{-6}$ A/W. The total error in repeating this measurement was approximately 15 percent.

The further inclusion of a $\lambda$ = 1.315-$\mu$m, 5-nm FWHM narrow band pass filter demonstrated the strong influence of scattered light within the monochromator for measurements in a region of steep fall-off in photocathode spectral responsivity. As a result, a double monochromator will be used for future measurements. A final value of $1.04 \times 10^{-7}$ A/W was established by this technique at a current density of $2 \times 10^{-11}$ A/cm$^2$. The total error in repeating this measurement is approximately 30 percent. Spectral responsivity versus wavelength is given in Fig. 68. Using a CW laser operating on the 1.318-$\mu$m transition in Nd:YAG, values were obtained at a current density of approximately $5 \times 10^{-9}$ A/cm$^2$, indicating responsivity between $1.7 \times 10^{-7}$ and $3 \times 10^{-7}$ A/W. This range of sensitivity is ascribed at least in part to variation in the CW output of the YAG laser The generally higher responsivity at higher input intensity is also possible.

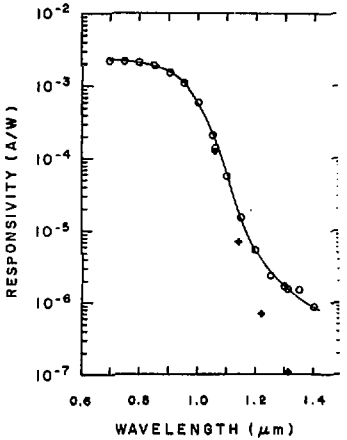


Fig. 68. Photocathode responsivity vs wavelength for Instrument Technology Ltd image converter streak tube, serial no. STM-S1-43. Monochromator operated with 0.5 mm slits (3.3 nm FWHM) and second order cut-off filters (O), with 2 mm slits (13.2 nm FWHM), second order cut-off filters and narrow band pass filters (+).

## Analysis of Lateral Shearing Interferometer

The wedged, lateral shearing interferometer is very useful for measuring laser-beam wavefront radius of curvature and for making semiquantitative estimates of beam phase-front distortions. Although shearing

interferometers have been used and analyzed for many years, there is no derivation in the literature of the formulas for the evaluation of the wavefront radius of curvature.

Bates[85] first discussed the principle of the lateral shearing interferometer. Important extensions were made by Drew[86] and by Brown.[87] The original application was to measure aberrations produced by optical elements. These early, relatively complex, devices were designed to maintain a zero optical path difference for the sheared beams. A significant advance in shearing interferometry was made by Murty[88] who introduced the simple wedged (or plane parallel) glass plate with a nonzero optical path difference. This instrument must be used with nearly monochromatic sources, and it is the one used for laser beam studies. To date there have been few reports of laser beam analysis using the Murty-type interferometer. Anthes et al[89] reported an experiment using a high-power glass laser in which the beam divergence was determined by measuring the fringe rotation of the interferogram. Lurie[90] reported an analysis but did not give the formulas necessary for interpretation of rotated fringe patterns. His results are also restricted to near-normal incidence on the shear plate.

We decided to make a theoretical and experimental effort to obtain an understanding of the shear plate adequate for our laser beam applications; the results are being published,[91] so they are only summarized here. The principle of the interferometer involves dividing the initial laser beam into two components of approximately the same intensity and displacing them laterally with respect to one another. In that region where the two beams overlap, interference results. As described, it is seen that the interferogram compares the original phase front relative to itself, displaced by the shear distance.

Figure 69 shows a side and top view of the interferometer with exemplary ray paths. The wedger angle $\delta$ has been greatly exaggerated in this schematic drawing. A left-handed coordinate system (x, y, z) is erected with the origin at the point of intersection of the incident principal ray and the front surface. The z-axis lies on the reflected ray from the front surface; the x-axis lies in the plane of incidence; the y-axis is upward (out of the plane of the figure in the top view). We characterize the incident beam by a paraxial form. Upon reflection from the front surface, we may write that part of the beam as

$$E_1 = \mathcal{E} e^{-ikz - i\Phi(x,y,z)}$$

in the chosen coordinate system. Another part of the beam is reflected from the rear surface of the wedged plate. If we call this beam $E_2$, it is obvious that the intensity of the reflected beam is given by the sum,

$$\left| E_1 + E_2 \right|^2 ,$$

allowing the interference of the beam with itself. The equation for the fringes (light or dark bands) may be derived,

$$2N\pi = k\theta y - kD + \Phi(x, y, L) - \Phi(x - s, y + \theta L, L) .$$

In this equation, L is the distance from the shear plate to the image, N is the order of the fringe, D is the optical path difference of the two beams, s is the shear distance, and $\theta$ is the beam tilt angle. In terms of the plate thickness, angle of incidence, and index of refraction, one finds the lateral shear distance, s, and the tilt angle, $\theta$:

$$s = t \frac{\sin 2\alpha}{\left(n^2 - \sin^2\alpha\right)^{1/2}}$$

$$\theta = 2\delta\left(n2 - \sin^2\alpha\right)^{1/2} .$$

The optical path difference is not important for our results.

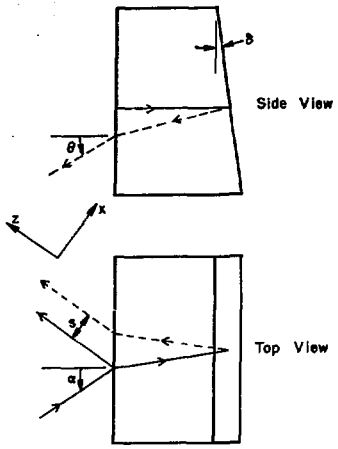


Fig. 69. A schematic representation of a lateral shearing interferometer of the Murty type.

In the event that the beam is free of distortion, the phase front will be given by

$$\Phi(x, y, z) = \frac{k}{2R(z)}(x^2 + y^2),$$

where R(z) is the local radius of curvature. The fringe pattern is found to be straight and simply rotated from the x-axis by an angle $\phi$:

$$\tan \phi = -\frac{sd}{\lambda R(L)},$$

$$d = \frac{\lambda}{\theta(1 - L/R(L))}.$$

These quantities are illustrated in Fig. 70 for a converging beam of negative R(L). If the beam does not possess a simple parabolic phase front, the interference pattern does not consist of straight fringes. It is possible to unfold such an interferogram by numerical procedures. More relevant here is the ability to make a qualitative determination of phase front distortion by observing the deviation of the fringes from the ideal linear pattern. Suppose the interference pattern shows a region where the fringes undergo an excursion that is a fraction, $\eta$, of the normal separation, K (see Fig. 70). This implies $\Phi(x, y, L) - \Phi(x - s, y, L)$ possesses a fraction $\eta$ of a full wave distortion from a pure parabolic wave front along the direction of shear over the distance s. Thus, a given interference pattern immediately shows the deviation from ideal phase behavior across the direction of shear.

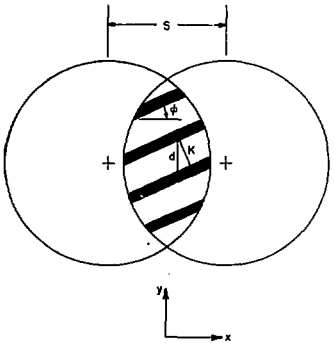


Fig. 70. A schematic representation of the interference pattern resulting from a lateral shearing interferometer.

We performed experimental verification of the results by producing beams of known radii of curvature.[91] The formulas for fringe rotation predicted the experimental results very accurately. We also confirmed the predicted variation of fringe rotation and spacing with the angle of incidence.[91] The utility of this interferometric technique lies in the simplicity with which one can measure the phase front uniformity of a parabolic phase front. Figure 71 shows the shear interferogram resulting from the reflection of a beam from a spherical mirror (10 m radius of curvature) with a 2-mm-diameter hole in the center. The phase distortion due to the presence of the hole is apparent.

Fig. 71. A shear interferogram resulting from the reflection of a laser beam from a spherical mirror (10 m radius of curvature) with a 2 mm hole in the center.

## POWER CONDITIONING FOR GROUP VIA ($^1$S) ATOMS

### Overview

The class of gas-laser systems based on the excitation of the $p^4\ ^1S$ state of Group VIA atoms (e.g., O, S, Se, Te) with energy extraction on the $p^4\ ^1S \rightarrow p^4\ ^1D$ or $p^4\ ^1S \rightarrow p^4\ ^3P$ transition is an extremely promising one for laser-fusion applications. Long energy-storage times are possible since the $^1$S state exhibits a long radiative lifetime and is resistant to deactivation by a wide variety of other species. Also, these transitions occur at useful wavelengths (459 to 790 nm) and exhibit stimulated emission cross sections that are low enough to inhibit parasitic amplified spontaneous emission but not so low that the medium cannot be saturated at reasonable energy fluxes.

The primary difficulty with this laser system is that no efficient means of generating large densities of $^1$S atoms has yet been demonstrated. For this reason, as noted in the last semiannual report,[92] we had implemented a research program to evaluate three different concepts for producing Group VIA ($^1$S) atoms. As described in that report, the three concepts involved in-situ electron-beam-excited rare-gas metastable energy transfer; in-situ electron-beam-excited photolytic energy transfer; and extra-cavity photolytic energy transfer. Our evaluation of the first two concepts is contained in that previous report. In the remainder of the present report, we will describe our progress in examining the third concept.

### Experimental Program

Extra-cell photolytic energy transfer utilizes spontaneous or lasing emission from a source (the photolytic driver), which is

transported to a separate cell containing the Group VIA bearing molecule that is to be photodissociated. The success of this approach relies on finding an efficient source of a radiation at a wavelength that coincides with a $^1$S-state producing absorption band of an appropriate molecule.

We had proposed[93] earlier that one such photolytic source could be the rare-gas halogen excimer NeF*. Although NeF* had not been observed before our work, it was predicted[94] to emit near 1070 Å, a useful wavelength for photolytically producing O($^1$S) from $CO_2$.

In order to search for NeF* emission, we configured the LILI electron-beam device[95] as shown in Fig. 72. The electron beam, confined by an externally applied, 3-kilogauss, axial magnetic field passed through the 25-μm-thick anode foil and entered a low-pressure drift region. After drifting 61 cm, the electron beam entered the high-pressure test cell region through a 32-μm-thick stainless-steel foil. The magnetic field then turned the beam by 45 degrees into the laser excitation region. The length of this region was 210 cm; the diameter was 7.5 cm. For these experiments, the electron beam had a peak current of about 20 kA, an area of 45 cm$^2$, a pulsewidth of about 400 ns, and a peak electron energy of 850 keV. The energy deposited in the cell was determined calorimetrically for each gas as described in the last report.[96] In order to avoid window-induced wavelength-dependent attenuation of the expected ~ 1100 Å radiation, a gate valve was placed between the test cell and the spectrometer. The spectrometer was filled with Ne to a pressure matching the total pressure in the cell, and the valve was open only during the time of the shot.

Figure 73 contains a microdensitometer trace of Kodak SWR film exposed to the emission from e-beam-excited mixtures of Ne and $F_2$. The peak of the strong emission feature, which we attribute to NeF*, is at 1080 Å. Two much weaker features are seen at 1195 Å and 1220 Å. The 1080 Å emission is not present when the e-beam is used to excite neon alone or helium/fluorine mixtures.

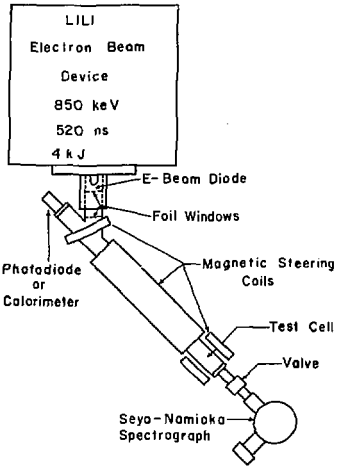


Fig. 72. Schematic diagram of the LILI experimental apparatus.

In addition to these spectral studies, we examined the temporal behavior of the NeF* emission with an absolutely calibrated windowless photodiode containing a tantalum cathode. The time dependence of the 1080 Å feature followed the e-beam current pulse. Figures 74 and 75 show the behavior of the time-integrated NeF* fluorescence signal with changes in neon and fluorine pressure. The peak fluorescence signal corresponds to a fluorescence efficiency of 5.8 percent. (Efficiency is defined as radiated energy divided by deposited e-beam energy.)

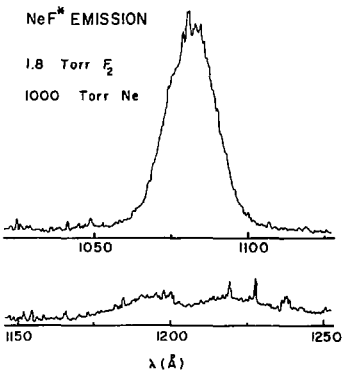


Fig. 73. Microdensitometer trace of the emission spectrum in the spectral region from 1050 to 1250 Å for electron-beam excited $Ne/F_2$ mixtures. The vertical scale is linear in optical density. The film was Kodak SWR, exposed in an 0.5 m Seya-Namioka spectrograph in first order with a 200-$\mu$m slit.

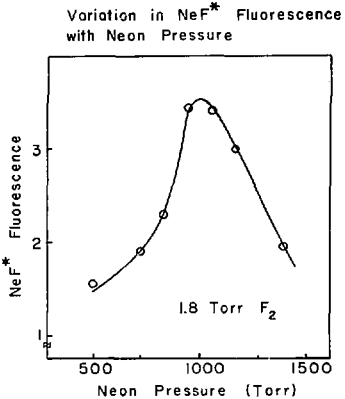


Fig. 74. Variation in the time-integrated NeF* fluorescence signal with neon pressure at a constant 1.8 torr $F_2$ pressure. The vertical scale is in relative units but is the same for both Figures 74 and 75.

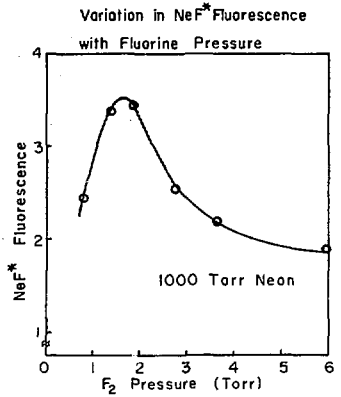


Fig. 75. Variation in the time-integrated NeF* fluorescence signal with $F_2$ pressure at a constant 1000 torr neon pressure. The vertical scale is in relative units but is the same for both Figs. 74 and 75.

This new light source is an interesting candidate for producing $O(^1S)$ from $CO_2$ as shown in Fig. 76. The NeF* emission lies in a spectral region that has been shown[97] to have high quantum yield for $O(^1S)$ production.

While studying e-beam excited $Ne/F_2$ mixtures, we discovered another broad emission feature between 1500 and 1600 Å. This emission band, which we attribute to a $^3\pi \rightarrow {}^3\pi$ transition in $F_2$, is observed in both e-beam-excited $Ne/F_2$ and $He/F_2$ mixtures but not in $Ar/F_2$ mixtures. The lower trace in Fig. 77 shows the spontaneous emission from this molecular fluorine band. As shown by the upper trace in this figure, lasing can occur at the 1575-Å peak of the emission spectrum in $He/F_2$ mixtures. We obtained this laser spectrum with an ~ 80 percent reflecting aluminum mirror at one end of the cell and a nonaligned $MgF_2$ window at the other end. Under these conditions, $F_2^*$ lased for helium pressures $\geq$ 1500 torr and $F_2$ pressures between 1 and 4 torr. Neon/fluorine mixtures did not lase in the pressure range investigated.

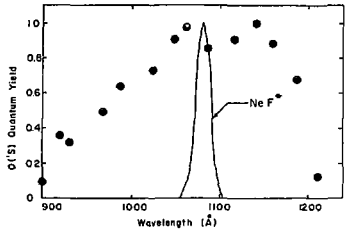


Fig. 76. The $NeF^*$ fluorescence spectrum superimposed on the $O(^1S)$ quantum yield vs wavelength from $CO_2$ (filled circles).

This new emission is a very promising one for photolytically producing $S(^1S)$ from COS, as shown by Fig. 78. The $F_2^*$ radiation occurs in an experimentally convenient spectral region in terms of window transmission and mirror availability. Further, both the spontaneous emission and lasing overlap the region of highest quantum yield[98] for $S(^1S)$ production. And, as will be discussed in more detail below, $F_2^*$ can be produced efficiently by e-beam excitation.

With an absolutely calibrated ITT 4115 photodiode, we observed the temporal behavior of the $F_2^*$ emission. Under conditions for which $F_2^*$ lased, the photodiode signal exhibited a sharp onset, delayed from the start of the e-beam current pulse, and followed the current pulse thereafter. The $F_2^*$ spontaneous emission closely followed the time dependence of the current pulse.

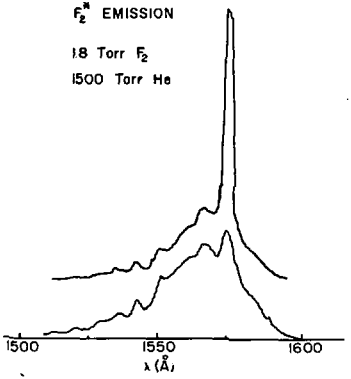


Fig. 77. Microdensitometer trace of the emission spectrum in the spectral region from 1500 to 1600 Å for electron-beam excited He/$F_2$ mixtures showing the spontaneous emission (lower trace) and lasing emission (upper trace). The vertical scale is linear in optical density. The base line for the lasing spectrum is vertically displaced, and the film is saturated at the peak of this spectrum. The spectra were recorded with a 0.5 metre Seya-Namioka spectrograph in first order with a 100 μm slit on Kodak SWR film.

Figure 79 shows the time-integrated fluorescence efficiency of the spontaneous emission from He/$F_2$ mixtures as a function of helium pressure. The triangles were obtained with the full incident e-beam of 40 J/cm$^2$. At 1000 torr, this energy loading corresponds to a deposited energy of 48 mJ/cm$^3$. The data represented by circles were obtained by attenuating the e-beam with stainless-steel screens installed in the drift region.

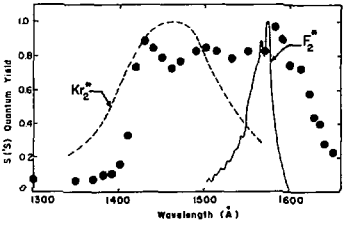


Fig. 78. The $F_2^*$ spontaneous emission spectrum superimposed on the S($^1$S) quantum yield vs wavelength from COS (filled circles). The $Kr_2^*$ emission spectrum is also shown for comparison.

At an incident e-beam energy of 2.7 J/cm$^2$ and 1000 torr helium, the deposited energy was 3.2 mJ/cm$^3$. The lower energy loading leads to somewhat increased fluorescence efficiency. Both sets of data indicate that still higher efficiencies might be obtained at higher helium pressures. The LILI test cell is structurally limited at present to a maximum pressure of ~ 1800 torr.

In order to examine the $F_2^*$ radiation, both parallel and perpendicular to the e-beam axis, we mounted a side-light-viewing photodiode midway down the test cell in addition to the end-light-viewing photodiode shown in Fig. 72. The experimentally observed side-light to end-light signal ratios are shown in Fig. 80 for both high (triangles) and low (circles) incident e-beam energies. For these measurements, the end and sides of the cell opposite the photodiodes were blackened with Nextel paint to eliminate optical feedback. The decrease in signal ratio with increasing helium pressure at an incident e-beam energy of 40 J/cm$^2$ is indicative of amplified spontaneous emission along the axis of the cell. This effect is not evident for an incident e-beam energy of 2.7 J/cm$^2$. Both sets of data yield equal

ratios at low helium pressures. This result provides strong evidence that the e-beam does not produce a significant concentration of transient species that might absorb $F_2^*$ radiation during the e-beam pulse, even at e-beam energy depositions near 50 J/ℓ. In view of the large absorptions normally observed[99] during an e-beam pulse in the visible and near UV, the lack of significant absorption in the present case near 1575 Å is a very gratifying result.

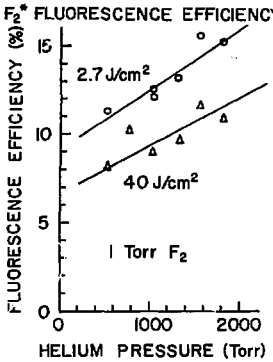


Fig. 79. The $F_2^*$ fluorescence efficiency vs helium pressure at a constant 1 torr $F_2$ pressure. The triangles are for an incident e-beam energy of 40 J/cm$^2$, and the circles are for an incident energy of 2.7 J/cm$^2$.

The LILI electron-beam device, as presently configured, does not appear to be capable of producing a highly efficient $F_2^*$ laser. With an optical cavity consisting of a highly reflecting dielectric mirror (R > 96% at 1575Å)

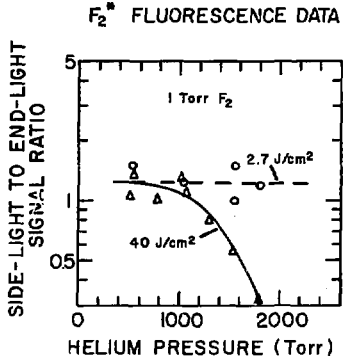


Fig. 80. The side-light photodiode to end-light photodiode signal ratio vs helium pressure at a constant 1 torr $F_2$ pressure. The triangles are for an incident e-beam energy of 40 J/cm$^2$, and the circles are for an incident energy of 2.7 J/cm$^2$.

at one end of the cell and an aligned $MgF_2$ flat output coupler at the other end, we obtained a maximum laser efficiency of ~0.5 percent. (Efficiency is defined as extracted laser energy divided by deposited e-beam energy.) The $F_2^*$ laser energy was measured using an evacuable calorimeter assembly that consisted of a 125-μm-thick titanium foil coated with carbon black and spot welded to a chromel-constantan thermocouple. The laser efficiency noted above was obtained at the highest excitation intensity level available with the LILI device, i.e., 40 J/cm$^2$, 500 ns, 1800 torr helium, and an active medium length of 2.1 metres. Further, the laser efficiency was increasing markedly with small increases in excitation intensity. For

example, the laser efficiency increased a factor of 5 by increasing the helium pressure from 1550 torr to 1800 torr, an increase of only 16 percent in pressure and in deposited e-beam energy. This observation led us to expect that still higher excitation intensities would produce even larger laser efficiencies. Our expectations have been realized in the series of experiments to be described next.

In February of 1977 we began design and construction of a 1.8-metre-long laser cell with a "λ" geometry, to be excited by a Febetron 705 electron-beam pulser (1.8 MeV, 400 joules, 50 ns). It was expected that the high intensity of this electron beam, coupled with the high-pressure capabilities of the laser cell ($> 10^4$ torr) would allow us to achieve an excitation intensity (energy deposited/$cm^3$-s multiplied by the length of cell) of 25 MW/$cm^2$, a factor of eight higher than the excitation intensities available on the LILI device.

Initial experiments were performed with a 70-cm-long straight laser cell which had ports to observe radiation both parallel (end light) and perpendicular (side light) to the e-beam axis. Analysis of the side-light emissions (observed with an absolutely calibrated VUV photodiode) from this laser cell indicated optimum fluorescence efficiencies of ~ 15 percent, in agreement with earlier results obtained with the LILI device. Under most conditions, the light emerging from the end-light port of the laser cell was completely dominated by stimulated emission. The time history of these laser pulses closely followed the time history of the ~ 50-ns-wide e-beam current pulse. By comparing the intensities of the side-light and end-light signals, we estimated a small signal gain in this test cell of ~ 3 percent/cm.

After the initial experiments with the short laser cell, the 1.8 metre "λ" cell was assembled on the front of the e-beam machine (see Fig. 81), and the magnetic-field coils were adjusted to guide the electron beam around the corner of the "λ" section and down the 1.4-metre active length of the cell. The Helmholtz coils at the end of the cell deflected into the chamber wall whatever fraction of the e-beam had not been absorbed, preventing the beam from damaging the optics or end windows. We then performed extensive calorimetry with a segmented carbon calorimeter (30 segments) to assure that the electron beam was propagating down the center of the test cell and that energy was being deposited in the gas at a rate predicted by Sandia's one-dimensional, Monte-Carlo electron-beam-deposition code.[100] Total e-beam energy reaching the calorimeter at several different He pressures and a number of different calorimeter positions in the laser cell is plotted in Fig. 82.

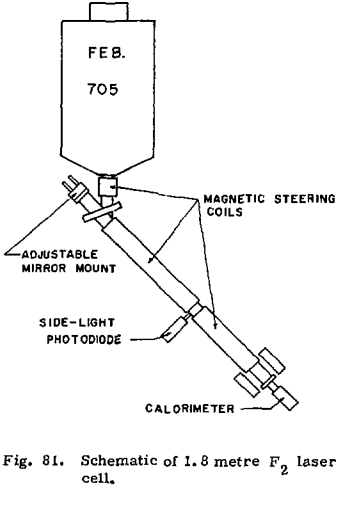


Fig. 81. Schematic of 1.8 metre $F_2$ laser cell.

The 1575-Å-laser energy was determined by measuring the temperature rise of a black-painted, 125-μm-thick, titanium-disc calorimeter, which was vacuum coupled to the

end of the laser cell. This calorimeter was calibrated by measuring its response to a standard quartz-iodide lamp which had been calibrated by the Epply Research Laboratories. The VUV photodiode used to view side-light fluorescence was calibrated by comparing its response to a 1575 Å monochromatic light source to that of a standard calibrated photodiode, which had been calibrated by the National Bureau of Standards. The transmission of each $MgF_2$ window or flat used in these experiments was measured using the same 1575 Å light source. (The monochromatic light source consisted of a stable, $H_2$-continuum discharge lamp and a VUV monochromator.) Considerable care was taken in all of the measurements leading to values for fluorescence efficiency and laser efficiency. Therefore, we feel that we can place conservative error bars on our absolute values of fluorescence and laser efficiency of ±29 percent and ±31 percent, respectively. Relative uncertainty of various values of fluorescence and laser efficiency are considered to be ±10 percent or less.

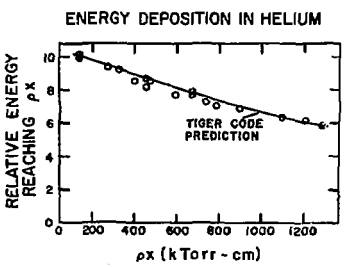


Fig. 82. Deposition of electron beam from Febetron 705 in helium; total energy reaching the carbon calorimeter at position $\rho x$ is plotted vs $\rho x$. The prediction from Sandia's 1-dimensional Monte-Carlo code "Tiger" is also shown.

In order to minimize the optical losses in the 1.8-metre laser cavity formed by the "λ" cell, mirror mounts were constructed which held the mirrors inside the laser cell, in direct contact with the $He/F_2$ laser mixture. Because the laser cell flexed noticeably when it was filled to $10^4$ torr, it was also necessary to design these mounts so that they could be adjusted from outside the pressure/vacuum seal of the laser cell. Thus, final mirror alignment was performed after the cell was filled with the laser gas mixture.

Table VII shows the results of firing the e-beam into the laser mixtures (7750 torr He, 10 torr $F_2$) with several different optical cavities on the system. In each case, the optical components had a 4.5-cm-diameter clear aperture. The optimum laser efficiency for this gas mixture was obtained with a dielectric coated high reflector on one end of the cavity and a $MgF_2$ flat output coupler on the other end. Apparently, optical feedback on the central axis of the laser is very important in this system. It should be noted that all-dielectric reflective optics were an absolute necessity with this laser. Due to the laser power densities of ~ 5 MW/cm$^2$, aluminum-coated optics were typically destroyed in a single shot of the device.

In order to get an estimate of how strongly the gas medium was being saturated by the laser photons, the total flux of the 1575 Å side-light signal was repeatedly observed with the laser mirrors first aligned and then misaligned. The ~3-cm-diameter laser beam (determined by burn patterns) was smaller than the 4.5-cm clear aperture of the optics and was essentially equal to the 2.8-cm-diameter e-beam. Therefore, the saturation observed in the side light should provide a reasonable estimate of the actual medium saturation on the laser axis. It is clear from the data in Table VII that the gas medium is significantly saturated by the laser photons. This conclusion is also supported by single-pass gain measurements made on the 1.8-metre-long cell, which determined that the large-signal

gain was ~ 1 percent/cm in contrast to the small signal gains of ~ 3 percent/cm measured on the 70-cm-long straight test cell. After determining the best optical cavity for a set of gas mixtures which were felt to be near optimum, we made a careful survey of laser efficiency, fluorescence efficiency, and sidelight saturation for a variety of He and $F_2$ pressures. The results of this survey are shown in Figs. 83 and 84. Perhaps the most important conclusion that may be drawn from these figures is that the optimum efficiency of the $F_2^*$ laser in this laser cell is 3.5 percent. However, from the data in Figs. 83 and 84 we feel confident that the efficiency of the $F_2^*$ laser can be increased a factor of 2 or more. The fluorescence efficiency measurements in Fig. 83 indicate that the optimum operating point for this laser system should be at He pressures lower than 5000 torr. However, at He pressures lower than 5000 torr, not enough e-beam energy is deposited in the laser cell to allow us to optically saturate the laser medium. This explains the sharp drop off of both laser efficiency and side-light saturation at low He pressures. The highest sidelight saturation achieved in these experiments was 32 percent. For a laser transition ending on the ground state with equal statistical weights for the two laser levels, 50 percent saturation would be the maximum expected under normal conditions. However, the lower level of the $F_2^*$ laser transition is probably an excited state which should be quickly quenched to the ground state in the high-pressure laser mixture of interest. Thus, if the laser pulse could be made longer than the collisional relaxation time of the lower state, greater saturations than 50 percent could be achieved and hence larger amounts of energy could be extracted.

To test these hypotheses, we plan to double the active length of the present 1.8-metre-long laser cell. This will allow us to work at much higher saturation levels at low He pressure. Also, by using a more highly reflective optical cavity, we whould be able

TABLE VII

Comparison of Optical Cavities on $F_2$ Laser

| Optical Cavity | VUV Laser Energy ($J/cm^2$) | Peak Laser Power ($W/cm^2$) | Laser Pulsewidth (ns) | Sidelight Saturation (%) | Laser Efficiency (%) |
|---|---|---|---|---|---|
| Flat High Reflector No Mirror | 0.12 | $4.5 \times 10^6$ | 33 | 15 | 1.3 |
| Flat High Reflector with 1/2-inch hole | 0.17 | $6.4 \times 10^6$ | 26 | 24 | 1.8 |
| Flat High Reflector $MgF_2$ Flat | 0.25 | $7.6 \times 10^6$ | 33 | 30 | 2.6 |

Note: Laser $\lambda$ = 1575 Å
Gas Mix = 6450 torr He, 10 torr $F_2$
Active Length of Laser Medium = 1.4 metre
E-Beam Energy Deposited Along Optic Axis = 9.3 $J/cm^2$

to lengthen the time laser photons spend in the optical cavity to greater than 100 ns to test its effects on the level of saturation.

In summary, the demonstrated efficiency of the $F_2^*$ laser is 3.5 percent, far higher than any other laser in the vacuum ultraviolet. We feel confident that the efficiency of the $F_2^*$ laser can at least be doubled to 7 percent and 10 to 15 percent efficiency may be possible. We feel that it is a very attractive candidate as a photolytic pump for a Group VI laser fusion laser.

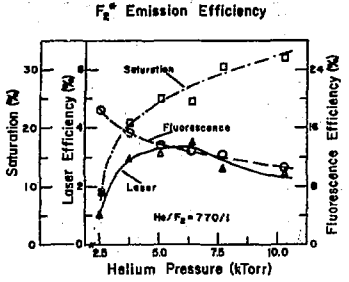


Fig. 83. $F_2^*$ fluorescence efficiency, laser efficiency, and sidelight saturation vs He pressure.

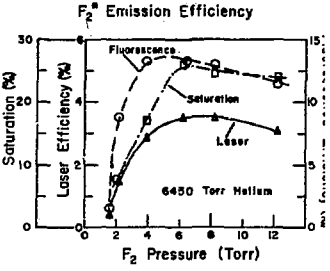


Fig. 84. $F_2^*$ fluorescence efficiency, laser efficiency, and sidelight saturation vs $F_2$ pressure.

## REFERENCES


1. J. A. Halbleib, Jr. and W. H. Vandevender, SAND74-0030, Sandia Laboratories, Albuquerque, NM, March 1975.

2. G. C. Tisone, Generation of Short Pulses for Extraction of Energy from an Electron-Beam Initiated $H_2$-$F_2$ Amplifier, Internal Memorandum, Sandia Laboratories, Albuquerque, NM, RS 5210/118.

3. G. P. Arnold and R. G. Wenzel, IEEE J. Quantum Electron., QE-8, 29 (1972).

4. R. G. Wenzel and G. P. Arnold, Appl. Opt., 15, 1322 (1976).

5. N. R. Greiner, IEEE J. Quantum Electron, QE-11, 884 (1975).

6. R. W. Getzinger, K. D. Ware, J. P. Carpenter, and G. L. Schott, IEEE J. Quantum Electron., QE-13, 4, (7 (1977). ).

7. R. A. Gerber and E. L. Patterson, J. Appl. Phys., 47, No. 8, 3524 (1976).

8. J. J. T. Hough, Appl. Opt., 16, 2297 (1977).

9. J. A. Mangano, R. L. Limpaecher, J. D. Daugherty, and F. Russell, Appl. Phys. Lett., 27, 293 (1975).

10. R. L. Kerber, G. Emanual, and J. S. Whittier, Appl. Opt., 11, 1112 (1972).

11. Laser-Fusion Research Progress Report, July-December 1976, SAND77-0157, Sandia Laboratories, Albuquerque, NM.

12. F. K. Truby, Appl. Phys. Lett., 29, 247 (1976).

13. J. H. Sullivan, R. C. Ferber, and J. W. Starner, J. Chem. Phys., 62, 1714 (1975).

14. J. H. Sullivan, J. Phys. Chem., 79, 1045 (1975).

15. J. B. Levy and B. K. W. Copeland, J. Phys. Chem., 72, 3168 (1968).

16. V. L. Tal'roze, G. K. Vasil'ev, and O. M. Baltovskii, Kinet Katal., 11, 277 (1970).

17. S. N. Foner and R. L. Hudson, Adv. Chem., V36, 34 (1962).

18. R. C. Mackenzie and M. Ritchie, Proc. R. Soc., A185, 207 (1946).

19. P. A. Giguère, Can. J. Res., 25B, 135 (1947).

20. F. Kaufman, Ann. Geophysics, 20, 106 (1964).

21. A. G. Streng, Combust. Flame, 6, 89 (1962).

22. F. K. Truby, SAND75-0513, Sandia Laboratories, Albuquerque, NM, October 1975.

23. M. A. Duguay, G. A. Fisk, J. M. Hoffman, J. B. Moreno, R. E. Palmer, M. E. Riley, and R. P. Sandoval, SAND76-0094, Sandia Laboratories, Albuquerque, NM, March 1976.

24. R. P. Sandoval and J. B. Moreno, Experimental and Theoretical Study of the Xenon Laser and Associated High-Gain Phenomena, Sandia Laboratories, Albuquerque, NM, to be published.

25. Laser-Fusion Research Progress Report, July-December 1976, SAND77-0157, Sandia Laboratories, Albuquerque, NM (1977), p. 16.

26. Ibid, p. 15.

27. Ibid, p. 23.

28. M. E. Riley, Temporal Pulse Broadening Due to Amplifier-Produced Frequency Narrow m's in the Small-Gain Limit, SAND76-0051, Sandia Laboratories, Albuquerque, NM (1976).

29. E. D. Jones, Laser Bandwidth Requirements for Distortionless Amplification, SAND76-0233, Sandia Laboratories, Albuquerque, NM (1976).

30. A. Siegman and D. Kuizenga, Appl. Phys. Lett., 14, 181 (1969).

31. M. A. Gusinow, J. Appl. Phys., 44, 4567 (1973).

32. Progress Report, op. cit., p. 17

33. Prospects of the High Power Iodine Laser, K. Hohla, G. Brederlow, E. Fill, R. Volk, K. J. Witte, IPP IV/93, Max-Planck-Institut fur Plasma Physik, Garching, 1976, p.18.

34. T. A. King (private communication).

35. M. A. Gusinow, Efficiency of Flashlamp Excited Lasers, SLA-73-0905, Sandia Laboratories, Albuquerque, NM (1973).

36. J. L. Emmett, A. I. Schawlow, and E. H. Weinberg, J. Appl. Phys., 35, 260 (1964).

37. V. S. Zuev, V. A. Katulin, V. Yu. Nosach, and O. Yu. Nosach, Soviet Phys. JETP 35, 870 (1972).

38. H. J. Baker and T. A. King, J. Phys. D: Appl. Phys., 9, 2433 (1976).

39. T. D. Padrick and R. E. Palmer, J. Chem. Phys., 62, 3350 (1975).

40. W. Fuss and K. Hohla, Max-Planck-Institut fur Plasma Physik, Garching, Report IPP IV/67 (1974).

41. M. E. Riley and R. E. Palmer, Evaluation of the Potential to Upgrade the SAIL-1 Laser to Higher Output Energies, SAND77-0775, Sandia Laboratories, Albuquerque, NM, May 1977.

42. E. A. Yukov, Sov. J. Quant. Electron, 3, 117 (1973).

43. V. A. Alekseev, T. L. Andreeva, V. N. Volkov, and E. A. Yukov, Soviet Phys., JETP 36, 238 (1973).

44. Numerical Analysis, John Todd, editor, McGraw-Hill (1962), New York, NY.

45. P. B. Ulrich, PROP-1: An Efficient Implicit Algorithm for Calculating Nonlinear Scalar Wave Propagation in the Fresnel Approximation, NRL Report 7706, Naval Research Lab, Washington, DC (1974).

46. A. Icsevgi and W. E. Lamb, Jr., Phys. Rev., 185, 517 (1969).

47. E. O. Schulz-DuBois, Bell Sys. Tech. J., 43, 625 (1964).

48. R. Bellman, G. Birnbaum, and W. G. Wagner, J. Appl. Phys., 34, 780 (1963).

49. G. Brederlow, K. J. Witte, E. Fill, K. Hohla, and R. Volk, IEEE J. Quant. Electron, QE-12, 152 (1976).

50. Progress Report, op. cit., p. 28.

51. R. E. Palmer, T. D. Padrick, and E. D. Jones, SPIE Proceedings, 76, 32 (1976).

52. C. C. Davis, R. J. Pirkle, R. A. McFarlane, and G. J. Wolga, IEEE J. Quantum Electron, QE-12, 334 (1976).

53. G. A. Skorobogatov and V. M. Smirnov, J. Gen. Chem, USSR, 41, 1419 (1971) (Eng. Transl.).

54. T. D. Padrick and R. E. Palmer, J. Appl. Phys., 47, 5109 (1976).

55. V. Y. Zalesskii and A. M. Kokushkin, Sov. J. Quantum Electron., 6, 813 (1976). (Eng. Transl.).

56. D. H. Burde and R. A. McFarlane, J. Chem. Phys., 64, 1850 (1976).

57. J. A. Blake and George Burns, J. Chem. Phys., 54, 1480 (1971).

58. G. A. Fisk, Internal Memorandum, Sandia Laboratories, Albuquerque, NM, RS 5210/119 December 1976 (unpublished).

59. W. Fuss and K. Hohla, Optics Comm., 18, 427 (1976).

60. R. E. Palmer and T. D. Padrick, J. Chem. Phys., 64, 2051 (1976).

61. T. D. Padrick and R. E. Palmer, Electronic Transition Lasers, J. Steinfeld, editor, p. 116. MIT Press, Cambridge, MA (1976).

62. V. Y. Zalesskii and T. I. Krupenikova, Optics and Spectroscopy, 30, 439 (1971).

63. S.V. Kuznetsova and A. I. Maslov, Sov. J. Quant. Electron, 3, 468 (1974).

64. T. Donohue and J. R. Wiesenfeld, J. Chem. Phys., 63, 3130 (1975).

65. J. C. Amphlett and E. Whittle, Trans. Faraday Soc., 63, 2695 (1967).

66. R. K. Pearson, editor, UCID-17237, Lawrence Livermore Laboratory, Livermore, CA, September 1976.

67. P. J. Robinson and K. A. Holbrook, Unimolecular Reactions, Wiley-Interscience, New York, NY (1972). See particularly Eqs. (4.31), (5.40), and (5.42).

68. For a recent experiment and references to earlier work, see P. Kolodner, C. Winterfeld, and E. Yablonovitch, Optics Comm., 20, 119 (1977).

69. J. D. Campbell, G. Hancock, J. B. Halpern, and K. H. Welge, Optics Comm., 17, 38 (1976).

70. R. V. Ambarizumian, N. V. Checkalin, V. S. Letokhov, and E. A. Ryabov, Chem. Phys. Lett., 36, 301 (1975).

71. J. Tardieu de Maleissye, F. Lempereur, C. Marsal, and H. I. Ben-Aim, Chem. Phys. Lett., 42, 46 (1976).

72. R. A. Carney, E. A. Piotrowski, A. G. Meister, J. H. Braun, and F. F. Cleveland, J. Molec. Spectry., 7, 209 (1961).

73. O. P. Judd, Appl. Phys. Lett., 22, 95 (1973).

74. S. J. Kast and C. Cason, J. Appl. Phys., 44, 1631 (1973).

75. P. K. Cheo, Lasers, Vol. 3, Ch. 2, A. K. Levine and A. J. DeMaria, eds., Marcel Dekker, New York, NY (1971).

76. M. A. Gusinow and G. A. Fisk, Internal Memorandum, Sandia Laboratories, Albuquerque, NM, RS 5215/004, May 1976 (unpublished).

77. W. Fuss, K. Hohla, R. Volk, and K. Witte, VII Int. Quantum Electronics Conference, San Francisco, CA, June 1974.

78. N. G. Basov, L. E. Golubev, V. S. Zuev, V. A. Katulin, V. N. Netemin, V. Yu Nosach, O. Yu Nosach, and A. L. Petrov, Sov. J. Quantum Electronics, 3, 524 (1974).

79. K. Hohla, G. Brederlow, E. Fill, R. Volk, and K. J. Witte, Max-Planck IPP Report IPP IV/93, September 1976.

80. R. J. Lagow, L. L. Gerchman, R. A. Jacob, and J. A. Morrison, J. Am. Chem. Soc., 97, 518 (1975).

81. M. A. Gusinow, Appl. Optics, 14, 2645 (1975).

82. S. I. Drabkina, JETP 21, 473 (1951).

83. G. A. Fisk, The Effects of Chemical Kinetics and Starting Material Regeneration on the Efficiency of an Iodine Laser Amplifier, SAND77-0880, Sandia Laboratories, Albuquerque, NM (1977).

84. J. P. Markiewicz and J. L. Emmett, IEEE J. Quant. Elec., QE-2, 707 (1966).

85. W. J. Bates, Proc. Phys. Soc., 59, 940 (1947).

86. R. L. Drew, Proc. Phys. Soc., B64, 1005, London (1951).

87. D. Brown, Proc. Phys. Soc., B67, 232, London (1954).

88. M. V. R. K. Murty, Appl. Opt., 3, 531 (1964).

89. J. P. Anthes, J. W. Lavasek, and M. A. Palmer, A Picosecond and Nanosecond Nd Glass High Power Laser Amplifier System, SAND76-0432, Sandia Laboratories, Albuquerque, NM, November 1976.

90. M. Lurie, Opt. Engin., 15, 68 (1976).

91. M. E. Riley and M. A. Gusinow, "The Evaluation of Laser Beam Divergence Utilizing a Lateral Shearing Interferometer," Appl. Optics, to be published October 1977.

92. Laser-Fusion Research Progress Report, July-December 1976, SAND77-0157, Sandia Laboratories, Albuquerque, NM, May 1977, p. 60.

93. A. K. Hays, A 3% Efficient O($^1$S) Laser at 5577 Å Photolytically Pumped by NeF*--A Proposal, SAND76-5856, Sandia Laboratories, Albuquerque, NM (1976).

94. L. A. Brau and J. J. Ewing, J. Chem. Phys., 63, 4640 (1975).

95. Laser-Fusion Research Progress Report, January-June 1976, SAND76-0357, Sandia Laboratories, Albuquerque, NM, August 1976, p. 87.

96. Laser-Fusion Research Progress Report, July-December 1976, SAND77-0157, Sandia Laboratories, Albuquerque, NM, May 1977, p. 64.

97. G. M. Lawrence, J. Chem. Phys., 57, 5616 (1972).

98. G. Black, R. L. Sharpless, T. G. Slanger, and D. C. Lorents, J. Chem. Phys., 62, 4274 (1975).

99. Laser-Fusion Research Progress Report, January-June 1976, SAND76-0357, Sandia Laboratories, Albuquerque, NM, August 1976, p. 42.

100. J. A. Halbleib, Sr. and W. H. Van Devender, TIGER: A One-Dimensional, Multilayer Electron/Photon Monte Carlo Transport Code, SLA-73-1026, Sandia Laboratories, Albuquerque, NM, March 1974.

## PUBLICATIONS

ELECTRON IONIZATION CROSS SECTIONS IN THE BORN APPROXIMATION, E. J. McGuire (5211), Phys. Rev. A 16, 62 (1977).

SCALED ELECTRON IONIZATION CROSS-SECTIONS IN THE BORN APPROXIMATION, E. J. McGuire (5211), Phys. Rev. A 16, 73 (1977).

ANGULAR DEPENDENCE OF POLARIZATION RELATED LASER-PLASMA ABSORPTION PROCESSES, M. K. Matzen (5211) and J. S. Pearlman (5214), Phys. Rev. Lett., 39, 140 (1977).

FOCUSING IN A LARGE F-NUMBER OPTICAL SYSTEM, M. A. Gusinow (5215), M. E. Riley (5211), and M. A. Palmer (5214), Opt. and Quant. Electronics, 9, 465 (1977).

EVALUATION OF THE POTENTIAL TO UPGRADE THE SANDIA ATOMIC IODINE LASER SAIL-1 TO HIGHER OUTPUT ENERGIES, M. E. Riley (5211) and R. E. Palmer (5215), SAND77-0775, Sandia Laboratories, Albuquerque, NM, May 1977.

SATURABLE ABSORPTION AND ROTATIONAL RELAXATION IN $CO_2$, G. N. Hays (5212), and G. A. Fisk (5215), J. Chem. Phys., 65, 4554 (1976).

OPTICAL ENERGY EXTRACTION FROM ELECTRON-BEAM-INITIATED $H_2F_2$ MIXTURES G. C. Tisone (5212) and J. M. Hoffman (5212), J. Appl. Phys., 47, 3530 (1976).

VOLUME-AVERAGED RATE EQUATIONS FOR PLANAR AND DISK-CAVITY LASERS, J. B. Moreno (5212), J. Appl. Phys., to be published September 1977.

DIRECT OBSERVATION OF THE DYNAMICS OF PICOSECOND PULSE OPTICAL BREAKDOWN, J. P. Anthes (5214) and M. Bass (U of CA), Appl. Phys. Lett., 31, 412 (1977).

STREAK CAMERA INVESTIGATION OF A MODE-LOCKED ARGON-ION LASER SYSTEM, E. D. Jones (5214) and M. A. Palmer (5214), Opt. Quantum Electronics, Short Comm., 9, 451 (1977).

CLOSURE OF PINHOLES UNDER INTENSE LASER RADIATION, J. S. Pearlman (5214) and J. P. Anthes (5214), Appl. Opt., 16, 2328 (1977).

EMISSION OF RF RADIATION FROM LASER-PRODUCED PLASMAS, J. S. Pearlman (5214), w/G. H. Dahlbacka (LLL), J. Appl. Phys., to be published.

CHARGE SEPARATION AND TARGET VOLTAGES IN LASER PRODUCED PLASMAS, J. S. Pearlman (5214), w/G. H. Dahlbacka (LLL), Appl. Phys. Lett., 31, 415 (1977).

POLARIZATION DEPENDENT ABSORPTION OF LASER RADIATION BY PLANAR TARGETS, J. S. Pearlman (5214), Phys. Rev. Lett., 28, 1397 (1977).

THE EFFECTS OF CHEMICAL KINETICS AND STARTING MATERIAL REGENERATION ON THE EFFICIENCY OF AN IODINE LASER AMPLIFIER, G. A. Fisk (5212), SAND77-0880, Sandia Laboratories, Albuquerque, NM, May 1977.

LASER BEAM DIVERGENCE UTILIZING A LATERAL SHEARING INTERFEROMETER, M. A. Gusinow (5215) and M. E. Riley (5211), Appl. Opt., to be published October 1977.

EVALUATION OF FLASHLAMP REFLECTORS FOR THE ATOMIC IODINE PHOTO-DISSOCIATION LASER. R. E. Palmer (5215), T. D. Padrick (5215), and R. B. Pettit (5842) J. Appl. Phys., 48, 3125 (1977).

VUV EMISSIONS FROM MIXTURES OF $F_2$ AND THE NOBLE GASES--A MOLECULAR $F_2$ LASER AT 1575 Å, J. K. Rice (5215), A. K. Hays (5215), and J. R. Woodworth (5215), Appl. Phys. Lett., 31, 31 (1977).

$H_2$-$F_2$ CHAIN REACTION RATE INVESTIGATION, J. C. Cummings (5216), w/J. Eugene Broadwell, W. L. Shackleford, A. B. Witte, J. E. Tvost, and George Emanuel, J. of Quantitative Spectroscopy and Radiative Transfer, 17, 97 (1977).

## PRESENTATIONS

BORN APPROXIMATION ELECTRON IONIZATION CROSS-SECTIONS, E. J. McGuire (5211), presented at the Topical Conference on Atomic Processes in High Temperature Plasmas, Knoxville, TN, February 16-19, 1977.

LASER-RELATED SPATIAL DISTRIBUTION OF PLASMA EXPANSIONS, M. K. Matzen (5211) and J. S. Pearlman (5214), presented at the 1977 IEEE International Conference on Plasma Science, Troy, NY, May 23-25, 1977.

A POWER-PULSE LENGTH PARAMETER STUDY OF TIME DEPENDENT EFFECTS IN LASER PRODUCED PLASMAS, M. K. Matzen (5211), Conference on Transport Processes in Laser Plasmas, Bar Harbon, ME, August 3-6, 1977.

PERFORMANCE CHARACTERISTICS OF THE SANDIA ATOMIC IODINE LASER (SAIL-1), T. D. Padrick (5215), R. E. Palmer (5215), M. A. Palmer (5214), and M. E. Riley (5211), presented at the 1977 IEEE/OSA Conference on Laser Engineering & Applications, Washington, DC, June 1-3, 1977.

SEMICLASSICAL EXCHANGE APPROXIMATION FOR INELASTIC ELECTRON SHATTERING, M. E. Riley (5211), Nancy Ann Mullaney, and D. G. Truhlar, presented at the 11th Great Lakes Regional Meeting, ACS, Stevens Point, WI, June 6-8, 1977.

HIGH POWER ATOMIC IODINE LASER CHARACTERISTICS, T. D. Padrick (5215), R. E. Palmer (5215), M. A. Palmer (5214), and M. E. Riley (5211), presented at the 11th Great Lakes Regional Meeting, ACS, Stevens Point, WI, June 6-8, 1977.

THEORETICAL STUDY OF PARASITIC OSCILLATIONS IN HIGH-GAIN LASER OSCILLATORS AND AMPLIFIERS, J. B. Moreno (5212), Conference on Laser Engineering and Applications, Institute of Electrical and Electronis Engineers and the Optical Society of America, Washington, DC, June 1-3, 1977.

SIMULTANEOUS ACTIVE AND PASSIVE Q-SWITCHING OF AN Nd:YAG SINGLE MODE OSCILLATOR, A. Owyoung (5214) and E. D. Jones (5214), IEEE Quantum Electronics Conference on Laser Engineering and Applications, Washington, DC, June 1-3, 1977.

SAIL-1 PERFORMANCE CHARACTERISTICS, T. D. Padrick (5215), 4th Colloquium on Electronic Transition Lasers (High Power Lasers and Applications), Munich, Germany, June 19-25, 1977.

POWER CONDITIONING FOR THE PRODUCTION OF GROUP VIA $^1S$ ATOMS, J. K. Rice (5215), J. R. Woodworth (5215), and A. K. Hays (5215), presented at the 7th Winter Colloquium on Quantum Electronics, Park City, UT, February 16-19, 1977.

CHARGE TRANSFER MEASUREMENTS FOR $He^{2+}$ IN H AND $H_2$, G. J. Lockwood (5232), J. M. Hoffman (5212), and G. H. Miller (5216), presented at the Topical Conference on Atomic Processes in High Temperature Plasmas, Knoxville, TN, February 16-18, 1977.